

Editor-in-Chief B.E.Paton

Editorial board:

Yu. S. Borisov	V. F. Grabin
A. Ya. Ishchenko	V. F. Khorunov
B. V. Khitrovskaya	I. V. Krivtsun
S. I. Kuchuk-Yatsenko	
Yu. N. Lankin	V. K. Lebedev
V. N. Lipodaev	L. M. Lobanov
V. I. Makhnenko	A. A. Mazur
O. K. Nazarenko	I. K. Pokhodnya
I. A. Ryabtsev	Yu. A. Sterenbogen
N. M. Voropai	K. A. Yushchenko
A. T. Zelnichenko	

International editorial council:

N. P. Alyoshin	(Russia)
U. Diltey	(Germany)
Guan Qiao	(China)
D. von Hofe	(Germany)
V. I. Lysak	(Russia)
N. I. Nikiforov	(Russia)
B. E. Paton	(Ukraine)
Ya. Pilarczyk	(Poland)
P. Seyffarth	(Germany)
G. A. Turichin	(Russia)
Zhang Yanmin	(China)
A. S. Zubchenko	(Russia)

Promotion group:

V. N. Lipodaev, V. I. Lokteva
A. T. Zelnichenko (exec. director)

Translators:

I. N. Kutianova, V. F. Orets,
T. K. Vasilenko, N. V. Yalanskaya

Editor

N. A. Dmitrieva

Electron galley:

I. S. Batasheva, T. Yu. Snegiryova

Address:

E.O. Paton Electric Welding Institute,
International Association «Welding»,
11, Bozhenko str., 03680, Kyiv, Ukraine
Tel.: (38044) 287 67 57
Fax: (38044) 528 04 86
E-mail: journal@paton.kiev.ua
http://www.nas.gov.ua/pwj

State Registration Certificate
KV 4790 of 09.01.2001

Subscriptions:

\$324, 12 issues per year,
postage and packaging included.
Back issues available.

All rights reserved.

This publication and each of the articles
contained herein are protected by copyright.
Permission to reproduce material contained in
this journal must be obtained in writing from
the Publisher.

Copies of individual articles may be obtained
from the Publisher.

CONTENTS

SCIENTIFIC AND TECHNICAL

- Belous V. Yu. and Akhonorin S. V.* Influence of controlling magnetic field parameters on weld formation in narrow-gap argon-arc welding of titanium alloys 2
- Tsybulkin G. A.* Compensation of external disturbance action on consumable electrode arc welding mode 5
- Giridharan P. K. and Murugan N.* Study on the effect of pulsed GTAW process parameters on bead geometry of the AISI 304L stainless steel welds 9
- Lebedev V. A.* Dependence between the rates of pulsed wire feed and wire melting in welding with short-circuiting 17
- Gedrovich A. I., Tkachenko A. N., Tkachenko S. A., Zelnichenko A. T., Alekseenko I. I. and Bondarenko V. L.* Peculiarities of structure and properties formation in 10Kh13G18D steel fusion zone 20
- Labur T. M., Ishchenko A. Ya., Taranova T. G., Kostin V. A., Grigorenko G. M. and Chajka A. A.* Influence of thermophysical conditions of welding on fracture resistance of the HAZ metal in the joints of aluminium alloy V96tss 25

INDUSTRIAL

- Makhnenko V. I., Makhnenko O. V. and Zinchenko O. Ya.* Investigation of performance of welded joints in steam generators PGV-1000M by leak tests 31
- Neklyudov I. M., Borts B. V., Vanzha A. F., Lopata A. T., Rybalchenko N. D., Sytin V. I. and Shevchenko S. V.* Improvement of quality of permanent joints — way to prolongation of service life of heat-generating assemblies 37
- Blashchuk V. E.** TIG welding of titanium and its alloys (Review) 41

- Borisov Yu. S., Panko M. T. and Rupchev V. L.* Methods for manufacture of powders with quasi-crystalline component for thermal spraying of coatings (Review) 47

BRIEF INFORMATION

- Zhernosekov A. M. and Kisilitsyn V. M.* Efficiency enhancement of gas generators of hydrogen-oxygen mixture 51
- Developed at PWI 16, 30, 50, 52



INFLUENCE OF CONTROLLING MAGNETIC FIELD PARAMETERS ON WELD FORMATION IN NARROW-GAP ARGON-ARC WELDING OF TITANIUM ALLOYS

V.Yu. BELOUS and S.V. AKHONIN

E.O. Paton Electric Welding Institute, NASU, Kiev, Ukraine

The efficiency of application of narrow-gap nonconsumable-electrode argon-arc welding of titanium alloys of ≥ 20 mm thickness is noted. It is shown that in order to provide a reliable fusion in the joints when using a transverse variable magnetic field, the value of magnetic induction in the arc zone should be equal to 8–9 mT. Minimum penetration of the side walls is achieved at the field frequency of 10 Hz.

Keywords: argon-arc welding, narrow gap preparation, titanium alloy, tungsten electrode, penetration, side wall, magnetic induction, field frequency

Narrow-gap non-consumable electrode welding is efficient method for connection of titanium alloys of 20 and ≥ 20 mm thicknesses. The main issue, which occurs in this case, is ensuring of reliable fusion of the narrow gap vertical walls with the bead being built-up and between the beads themselves. Different technological methods exist for solution of this task: application of the welding conditions with increased heat input; sequential arrangement of the beads [1]; mechanical oscillations of the electrode from the edge to the edge [2]; application of the transverse magnetic field [3]. However, as far as the process of welding with increased heat input is characterized by low productivity, welded joints, produced under such conditions, have HAZ of big width. As far as titanium and titanium-base alloys relate to non-magnetic materials, the

most efficient method for ensuring reliability and uniformity of melting of the gap side walls is control of the welding arc deviation by means of application of the external controlling transverse variable magnetic field (hereinafter the magnetic field).

In [3] narrow-gap welding of titanium using tungsten electrode with the controlling magnetic field is described. In mentioned method of welding the magnetic field is created by an electric magnet, which has a magnetic conductor of special shape, lowered into the prepared groove (Figure 1), whereby force lines of the transverse magnetic field are directed parallel to the weld axis.

At present data on influence of the controlling magnetic field parameters on formation of weld in narrow-gap welding are absent in the literature. In welding with the controlling magnetic field its the most important parameters, which effect deviation of the welding arc, are magnetic induction B_x in the arc zone (magnetic induction component along axis x) and frequency W of the variable magnetic field.

The goal of this work is investigation of regularities of the weld shape change depending upon parameters of the magnetic field, which will allow choosing the optimal ones, under which a quality bead will be formed.

For this purpose a number of the deposition experiments were carried out that simulated performance of the filling passes with subsequent measurement of size of the produced welds (Figure 2). The experiments were carried out in two stages: at the first stage influence of magnetic induction on weld shape cross-section at constant frequency of magnetic field was investigated, and at the second stage — influence of frequency of the variable magnetic field on weld shape cross-section at constant value of magnetic induction was studied.

Preliminary experiments showed that welds, produced without deviation of the welding arc, had bigger depth of penetration of the gap bottom and small width of the weld in its lower part (Figure 3, a). In this case occurrence of lacks of penetration in corners of the groove is possible. It is also determined that significant penetration of the gap side walls causes

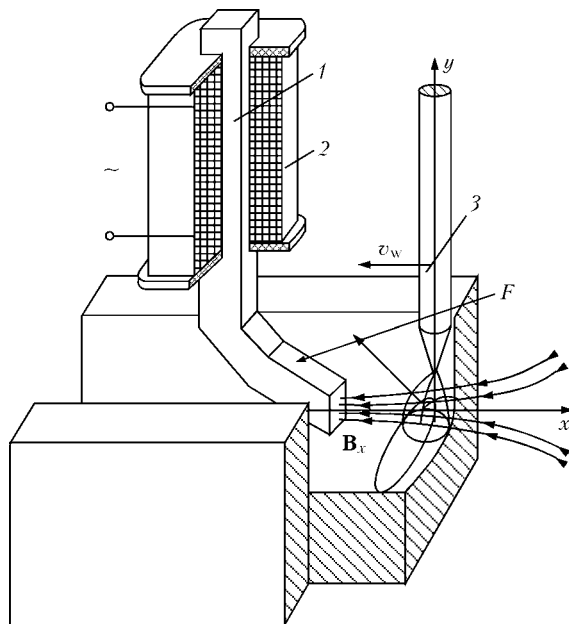


Figure 1. Scheme of narrow-gap tungsten electrode welding: 1 — electromagnet core; 2 — coil; 3 — electrode; F — force which deviates arc column; v_w — welding speed

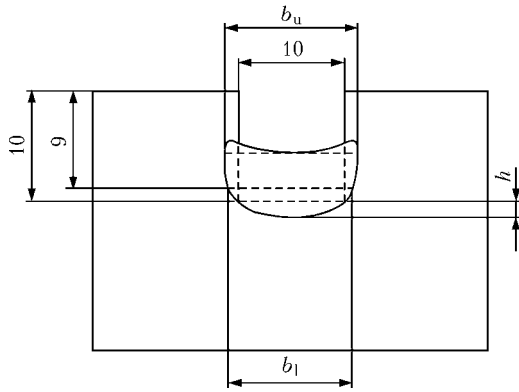


Figure 2. Scheme of narrow-gap bead deposition: h — depth of base metal penetration; b_u , b_l — width of bead in upper and lower parts, respectively

excessive width of the weld and HAZ, whereby such defects as lacks of fusion may occur (Figure 3, *b*).

In this connection as an optimal shape of deposited bead in narrow-gap welding is accepted the one, at which depth of penetration of the previous bead surface is minimal, and width of the weld in its upper part b_u equals the width in its lower part b_l , i.e. depth of penetration of the side walls over their height is the same. In this case HAZ has small length, and lacks of penetration do not occur in the weld.

Welding was performed under constant conditions. The bead of 5 mm height was built up at 400 A current, which corresponds to lower limit of the welding current range and allows producing a welded joint, having HAZ of small length. Arc voltage was $U_a = 12$ V, welding speed $v_w = 8$ m/h.

Controlling magnetic field was created by an electric magnet with the OI-119 device developed in PWI, which generated alternative current pulses, the shape of which being close to the rectangular ones (Figure 4). In the course of the experiments frequency of the variable magnetic field was set within 2.5–

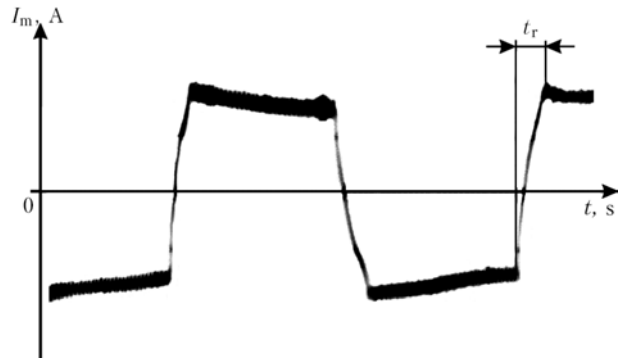


Figure 4. Oscillograms of pulses of magnetization current passing through electromagnet coil: I_m — magnetization current; t_r — time of current pulse rise

80.0 Hz, and value of magnetic induction of the variable magnetic field in the arc zone varied from 2 to 12 mT. The specimens were made of commercial titanium of the VT1-0 grade, and the filler wire — from titanium alloy OT4-1. Selection of the latter is stipulated by the fact that it contains aluminium as an alloying element, which allows accurate determining of the weld width and length of the fusion zone by the method of X-ray microspectral analysis [3]. Measurement of the bead width b and penetration depth h of the base metal was performed on transverse microsections cut out from the welds.

Results of the experiments showed that as magnetic induction in the arc zone increases, degree of penetration of the narrow groove side walls in the lower part increases too, i.e. b_l increases (Figure 5). At $B_x = 8$ mT width of the weld in its upper and lower parts is the same (Figure 5), while at $B_x < 8$ mT width of the weld in its upper part is bigger than in the lower one. Microsections of the deposits produced at $B_x < 8$ mT, have lacks of fusion in the corners of the prepared grooves. At $B_x = 11–12$ mT cross-section of the built-up bead acquires the shape, shown in Fi-

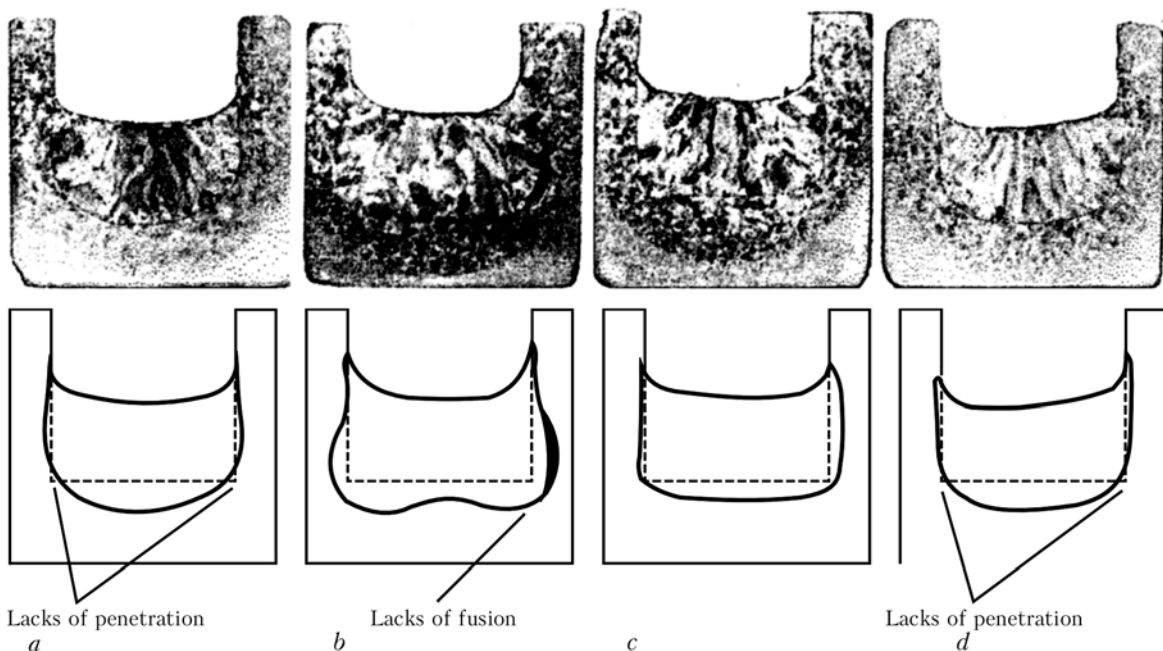


Figure 3. Macrosections of beads produced by narrow-gap welding (above), and schemes of penetration shape (below): *a* — bead produced without controlling magnetic field; *b* — $b_u < b_l$; *c* — $b_u = b_l$; *d* — $b_u > b_l$

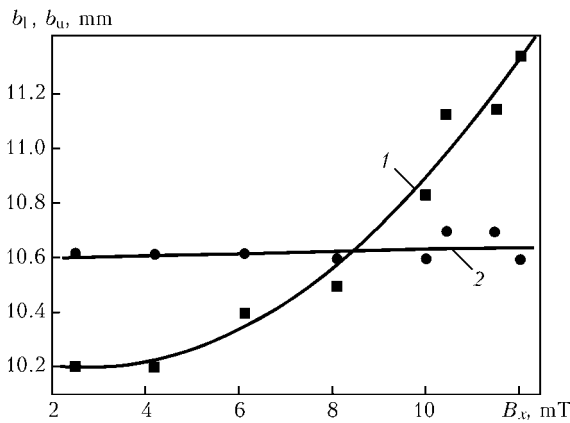


Figure 5. Dependence of width of weld produced by narrow-gap welding upon magnetic induction of variable magnetic field: 1, 2 — weld width in lower and upper parts, respectively

Figure 3, *b*. As magnetic induction increases, depth of penetration of the groove bottom reduces (Figure 6).

So, proceeding from the results obtained one may draw conclusion that at $B_x = 8-9$ mT optimal formation of the bead is achieved, i.e. width of the weld in its upper and lower parts is the same.

Frequency of the variable magnetic field also exerts its influence on the bead shape. Results of the experiments showed that the biggest depth of penetration of the groove side walls is achieved at the magnetic field frequency 2.5 Hz (Figure 7), in particular, when the arc stays near the side wall for a long time. In this case depth of penetration of the groove side walls in the weld upper part is smaller than in the lower part. Cross section of the built-up beads, produced at the magnetic field frequency $W = 2.5-4.0$ Hz, has in the upper part of the weld smaller width than in the lower one (see Figure 3, *b*). The smallest depth of penetration of the groove side walls is achieved at $W = 80$ Hz. Shape of cross-section of the built-up

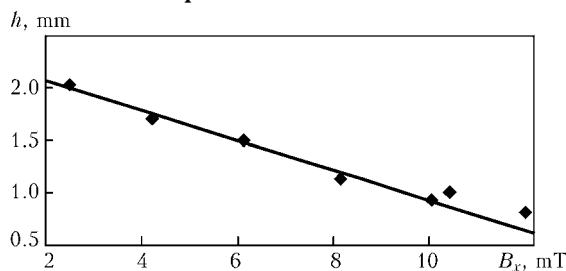


Figure 6. Dependence of penetration depth h of narrow groove bottom upon magnetic induction B_x of variable magnetic field

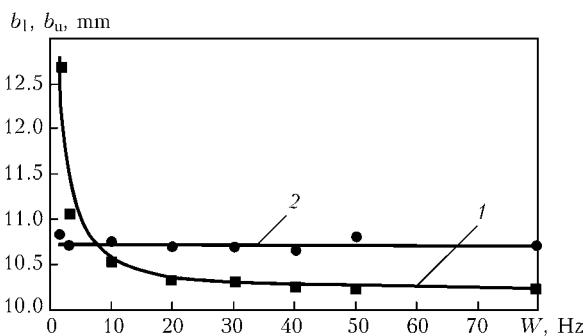


Figure 7. Dependence of width of weld produced by narrow-gap welding upon frequency W of variable magnetic field: 1, 2 — the same as in Figure 5

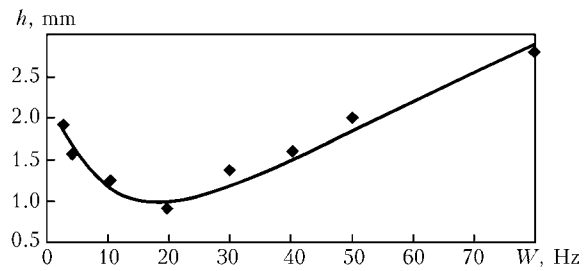


Figure 8. Change of penetration depth of narrow groove bottom upon frequency of variable magnetic field

bead at $W = 50-80$ Hz is similar to shape of the bead, produced without action of the magnetic field. Microsections of the deposits at $W = 20-80$ Hz have lacks of fusion in corners of the prepared grooves.

Dependence of depth of the groove bottom penetration upon frequency of the variable magnetic field is minimal at $W = 10-20$ Hz (Figure 8). Inflection of the curve is connected with the fact that the biggest depth of the groove bottom penetration at $W = 2.5-10.0$ Hz occurs near side walls, and at $W = 20-80$ Hz — in center of the weld. Depth of penetration of the groove bottom at the magnetic field frequency $W = 10-20$ Hz is minimal and constitutes only 1 mm, whereby values of this parameter in the weld center and near side walls are the same. In addition, cross-section of the beads, produced at $W = 4-10$ Hz, has the same width in their upper and lower parts. So, at $W = 10$ Hz a bead is formed, in which depth of the groove bottom penetration is minimal, and width in its upper and lower parts is the same.

More deep penetration of the groove side walls by means of the magnetic induction increase is connected with the fact that angle of the welding arc turn in this case increases [4], due to which greater part of the anode spot transfers to the side wall, where heat input and depth of penetration respectively increase.

Reduction of penetration depth of the groove side walls by means of the magnetic field frequency increase is connected with increase of the number of the arc transitions per unit time from one extreme position into the other. As far as time of the magnetization current pulse rise t_r (see Figure 4) constitutes 6 ms, and in case of the magnetic field frequency change

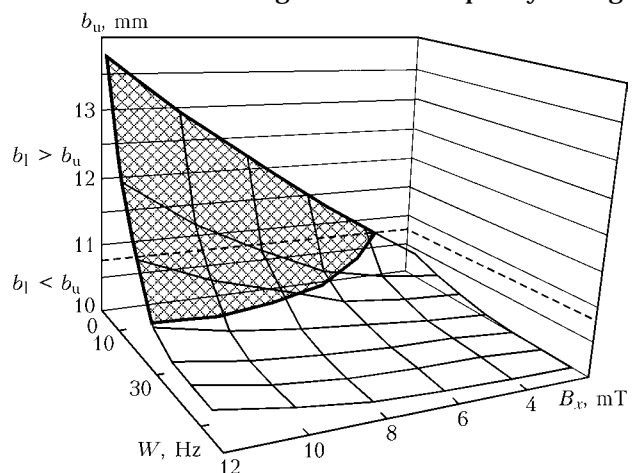


Figure 9. Influence of induction B_x and frequency of variable magnetic field W on bead width in lower part b_1 ; in dashed area $b_1 > b_u$



this value remains constant (when the OI-119 control device is used), within this time the arc is in intermediate position and the narrow gap bottom melts. Due to increase of the magnetic field frequency, the magnetic induction being unchangeable, penetration depth of the side walls reduces (Figure 9). For this to occur at the same depth when the magnetic field frequency increases, it is necessary to turn welding arc at a bigger angle, and in order to achieve this it is necessary to increase the magnetic induction. If $W = 20$ Hz, uniform penetration of the side walls is achieved at $B_x = 12-13$ mT.

CONCLUSIONS

1. For forming built-up bead of optimal shape in narrow-gap welding and for excluding lacks of fusion

when building up a bead of 5-6 mm height into 8-10 mm gap, the magnetic induction value of the controlling variable magnetic field in the arc zone should be 8-9 mT.

2. Minimal penetration of the previous layer surface and uniform over the height penetration of the narrow groove side walls occurs at the variable magnetic field frequency 10 Hz.

1. Hori, K., Haneda, M. (1999) Narrow gap arc welding. *J. JWS*, **3**, 55-56.
2. Grinin, V.S., Shtrikman, M.M. (1982) High-efficient automatic narrow-gap welding. *Svarochn. Proizvodstvo*, **7**, 21-23.
3. Paton, B.E., Zamkov, V.N., Prilutsky, V.P. (1996) Narrow-groove welding proves its worth on thick titanium. *Welding J.*, **5**, 37-41.
4. Gagen, Yu.G., Taran, V. (1970) *Magnetically-impelled arc welding*. Moscow: Mashinostroenie.

COMPENSATION OF EXTERNAL DISTURBANCE ACTION ON CONSUMABLE ELECTRODE ARC WELDING MODE

G.A. TSYBULKIN

E.O. Paton Electric Welding Institute, NASU, Kiev, Ukraine

The paper deals with one of approaches to reducing the influence of external disturbances on the arc welding mode parameters, based on application of the absorption principle. The procedure of structural synthesis of compensating feedback is described. Results of mathematical simulation are presented.

Keywords: arc welding, mode stabilization, absorption principle, compensation of disturbances, structural synthesis, internal models

The issue of the mode stabilization of the automatic consumable electrode arc welding has been discussed since long [1-5]. This problem, as it is known, is connected with significant influence on the arc welding process of various kinds of uncontrollable disturbances, causing reduction of the welded joint quality. The main difficulty in building of the stabilization systems consists in the fact that a welding circuit with a consumable electrode itself as an object of automatic control represents a system with natural feedback, which ensures self-regulation of the arc length [6]. That's why additional introduction into the welding circuit of additional feedbacks for stabilizing the welding mode does not always ensure achievement of the desirable effect.

Nevertheless, another possibility for removing influence of the disturbances exists, based on application of so called absorption principle [7], the basis of which is synthesis of internal model of the external disturbance with introduction of the compensation feedback. Despite increased interest within recent years to the systems of this class [7-11], mentioned principle is not yet used to the degree it deserves in the welding process control systems.

The task of structure synthesis of the compensation device (CD), which ensures in some cases reduction

of the external action influence on the arc welding mode parameters, is considered in this work.

Let us consider structural scheme of the welding circuit (Figure 1), drawn on the basis of equations [12]:

$$\begin{aligned} (LD + S)i &= u_s - u_s; \quad u_s - u_a = Ri; \quad u_a = u_0 + E\dot{l} \\ l = H - h; \quad h &= \frac{1}{D}(v_e - v_m); \quad v_m = Mi, \end{aligned} \tag{1}$$

where L is the inductivity of the welding current source; R is the total resistance of the leads, the electrode extension h and sliding contact in the torch tip; u_s is the voltage at output terminals of the welding

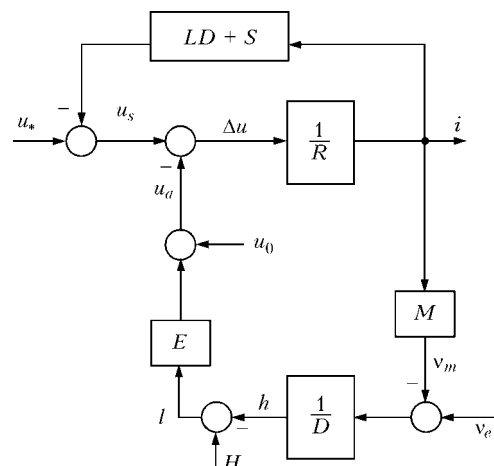


Figure 1. Structural scheme of welding circuit (here and in Figures 2 and 3 see designations in the text)



current source; u_* is the open-circuit voltage; u_a is the arc voltage; u_0 is the total of the near-electrode voltage falls; i is the welding current; l is the length of arc gap; $E \equiv \partial u_a / \partial l$ is the intensity of electric field in the arc column; $S \equiv \partial u_s / \partial i$ is the steepness of volt-ampere characteristic of the welding current source at nominal current value i_{nom} ; H is the distance between the end of the current-leading tip and free surface of the welding pool; v_e is the speed of movement (feed rate) of the consumable electrode relative the torch nozzle; v_m is the rate of the electrode melting; $M \equiv \partial v_m / \partial i$ is the steepness of the electrode melting characteristic at nominal values of the welding current i_{nom} and the electrode extension h_{nom} ; $D = d/dt$ is the differentiation operator; t is the time.

One can see from Figure 1 that external disturbances, which act on voltage u_* , speed v_e , and distance H , can cause change of nominal values of welding current i_{nom} and arc voltage $u_{a,nom}$. Let us consider for definiteness the case, when disturbance of the nominal arc welding mode is caused by short-term change of H . In this case first of all change (disturbance) of arc voltage $u_a(t)$ will occur. Let's present $u_a(t)$ in the form of a sum:

$$u_a(t) = u_{a,nom} + \xi(t), \quad (2)$$

where $\xi(t)$ is the resulting disturbance.

It is clear that for compensation of the disturbance $\xi(t)$ it is necessary to measure it. But as far as direct measurement of $u_a(t)$ is practically impossible, we will try to estimate $\xi(t)$ in indirect way, having introduced into structure of the system the double-input internal model of external disturbance. Idea of indirect estimation consists in the following. If two coordinates in the circuit, consisting of detecting units, are selected in such way that the element on which acts disturbance $\xi(t)$ is located between them, difference of the selected coordinates will be the function of this disturbance. At a certain selection of the internal model operators a certain variable $\delta(t)$ will be proportional or equal to the disturbance $\xi(t)$. It should be noted that the idea of indirect measurement of the disturbances was, evidently, proposed for the first time by A.G. Ivakhnenko [13] and was further developed in works [14–17].

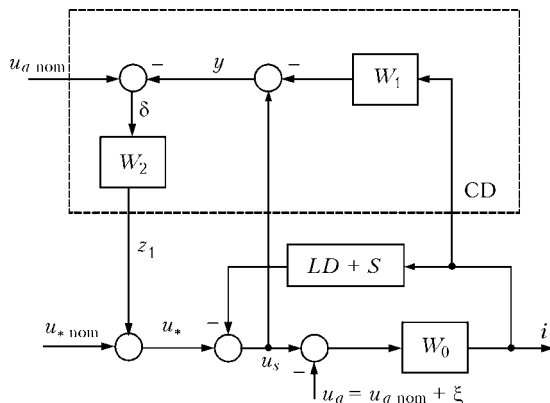


Figure 2. Structural scheme of CD with compensation action on open-circuit voltage

CD structure, which includes the double-input internal model of external disturbance and the compensation feedback, is presented in Figure 2, where for convenience of consideration only a section of the welding circuit, the elements of which are used in further calculations, is shown. On the basis of internal model (sometimes it is called a differentiation fork [15, 17]) one may write

$$y = (1 - W_1 W_0) u_s - W_1 W_0 u_a, \quad (3)$$

where through W_0 the operator is designated

$$W_0 = 1/R \quad (4)$$

and through W_1 --- the unknown for a time being operator.

If the measurement links are arranged in such way that

$$W_1 W_0 \equiv 1, \quad (5)$$

from expression (3) follows the identity

$$y \equiv u_a, \quad (6)$$

which means that at any time t signal $y(t)$ numerically equals arc voltage $u_a(t)$. It is important, because in this case we will get, according to the structural scheme presented in Figure 2 and taking into account (2) and (6), the equality $\delta = u_{a,nom} - y = u_{a,nom} - u_{a,nom} - \xi = -\xi$. Hence it follows that signal $\delta(t)$, created by the measurement links, does not depend either on the welding current i , or on arc voltage $u_a(t)$, but depends only upon the disturbance $\xi(t)$.

And now let us use principle of absorption [7], according to which invariance of voltage u_a relative the disturbance $\xi(t)$ may be ensured by its oppression by the compensation action $z_1(t)$. As far as in this scheme (Figure 2) compensation action is directed over the control circuit with voltage u_* , mentioned invariance means that $z_1 \equiv W_2 \delta \equiv \xi$. So, for compensation of $\xi(t)$ it is necessary to ensure fulfillment of the identity $W_2 \equiv 1$.

In practice it is advisable to construct the control law $u_* = u_*(\delta)$, which performs current compensation of the disturbance, proceeding from conditions of astatism, i.e. in integral form

$$u_* = u_{*,nom} + z_1; \quad z_1 = K_1 \int_0^t \delta(t) dt,$$

where $u_{*,nom}$ is the nominal value of open-circuit voltage; K_1 is the positive coefficient, whereby the operator W_2 will have the form

$$W_2 = \frac{K_1}{D}. \quad (7)$$

So, for compensation (absorption) of the disturbance ξ it is necessary to ensure according to (4), (5) and (7) fulfillment of two conditions:

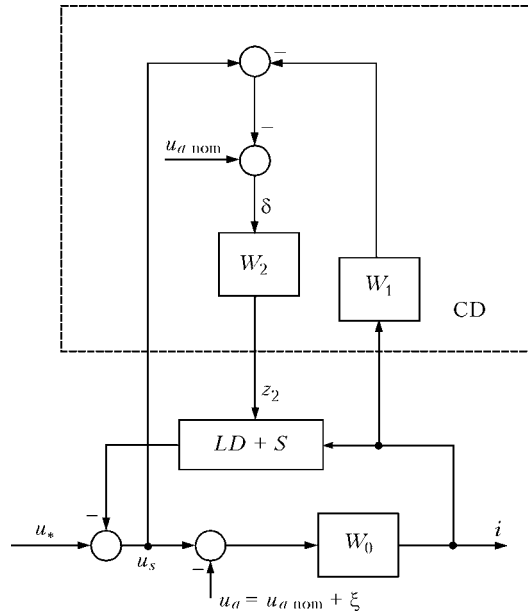


Figure 3. Structural scheme of CD with compensation action on steepness of volt-ampere characteristic of welding current source

$$W_1 \equiv \frac{1}{W_0} = R; \quad W_2 = \frac{K_1}{D}. \quad (8)$$

Selection of the operators W_1 and W_2 is the final stage of synthesis of the absorption model, which includes a double-input model of external action and the compensation feedback. As a result we get CD

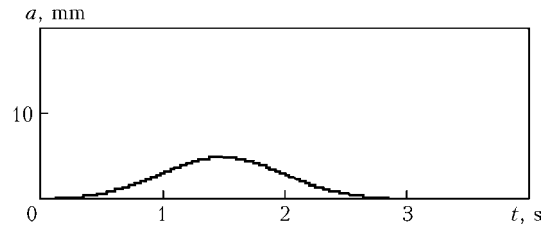


Figure 4. Diagram of function $a(t)$

with a rather valuable property — it creates a significantly oppressing external disturbance signal $z_1(t)$, which is fed to a section of the circuit, covered by the double-input model. This ensures stabilization of arc voltage at the level of the assigned nominal value $u_{a\text{nom}}$.

In those cases when it is more important to ensure independence of the welding current i upon disturbance $\xi(t)$, the compensation feedback has to be connected to parametric input of the unit with a transmission function $(LD + S)$, as it is shown in Figure 3. In this case we will build the law of control, which performs current compensation of the disturbance, in the following form:

$$S = S_{\text{nom}} + z_2; \quad z_2 = K_2 \int_0^t \delta(t) dt,$$

where S_{nom} is the nominal value of the volt-ampere characteristic steepness of the welding current source; and $K_2 = \text{const} > 0$.

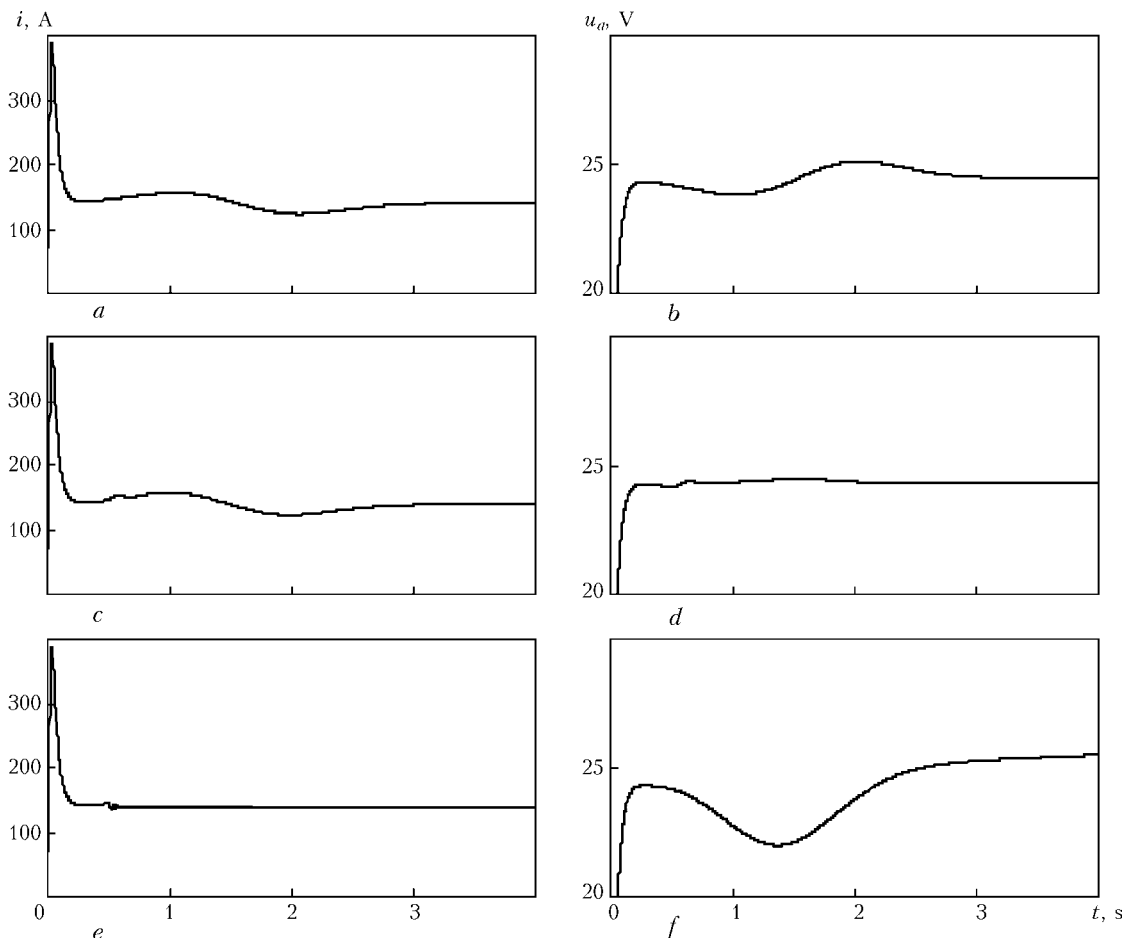


Figure 5. Diagrams of functions $i(t)$ (a, c, e) and $u_a(t)$ (b, d, f) built according to simulation results (for a–f see the text)



For checking efficiency of the CD introduction into the welding circuit, computer simulation of the dynamics of the processes, proceeding in the circuit in arc welding, was performed.

The following parameters of the circuit and welding modes were taken: $L = 4 \cdot 10^{-4}$ H; $R = 0.02$ Ohm; $S = -0.02$ V/A; $u_* = 30$ V; $u_0 = 12$ V; $u_{a\text{nom}} = 24$ V; $v_e = 50$ mm/s; $H_{\text{nom}} = 17$ mm. Calculated values of the CD coefficients K_1 and K_2 constituted $K_1 = 50$ s $^{-1}$ and $K_2 = 0.01$ (A·s) $^{-1}$.

As a disturbance change of the distance $H(t)$, caused by «tacking» on the axial line of the joints being welded, was considered. The law of the $H(t)$ change was assigned by the dependence $H(t) = [17 - a(t)]$ mm, where $a(t) = 5e^{-n(t-1.5)^2}$ mm, $n = 2c^{-2}$. Diagram of function $a(t)$ is shown in Figure 4.

Results of the simulation are presented in Figure 5 in the form of curves $i(t)$ and $u_a(t)$ in the circuit without (Figure 5, a, b) and with (Figure 5, c-f) compensation feedback. When comparing the curves one can see that in the circuit without CD the distance disturbance causes change of the welding current $i(t)$ and arc voltage $u_a(t)$ (Figure 5, a, b). In the circuit with CD the situation is somewhat different. In the case when the compensation signal $z_1(t)$ acts on the open-circuit voltage u_* (see Figure 2), arc voltage $u_a(t)$ gets independent of the disturbance and equal to $u_{a\text{nom}}$ (Figure 5, d), whereby deviation of the welding current $i(t)$ from its nominal value i_{nom} remains practically uncompensated (Figure 5, c). In the case when the compensation signal $z_2(t)$ acts on steepness S of volt-ampere characteristic of the welding current source (see Figure 3), invariant relative the disturbance gets welding current $i(t)$, whereby change of arc voltage $u_a(t)$ even somewhat increases in comparison with similar parameters in the scheme without CD.

So, results of numeric simulation showed that introduction into the control system of the consumable electrode arc welding process of compensation feed-

backs allowed implementing the idea of absorption of harmful actions. However, in this case it becomes possible to stabilize only one of the main mode parameters (either welding current or arc voltage). Nevertheless, high efficiency of introduction of the compensation feedback allows expecting that application of the disturbance compensation principle in development of the welding equipment opens one more way to quality improvement of welded joints.

1. Paton, B.E. (1958) Some problems in automatic control of welding processes. *Avtomatich. Svarka*, **4**, 3-9.
2. Gladkov, E.A. (1976) *Automation of welding processes*. Moscow: N.E. Bauman MVTU.
3. (1986) *Automation of welding processes*. Ed. by V.K. Lebedev, V.P. Chernysh. Kiev: Vyshcha Shkola.
4. Lebedev, A.V. (1978) Efficiency of stabilization of mean value of current in semiautomatic welding. *Avtomatich. Svarka*, **10**, 37-41.
5. Paton, B.E., Shejko, P.P., Zhernosekov, A.M. et al. (2003) Stabilization of the process of consumable electrode pulse-arc welding. *The Paton Welding J.*, **8**, 2-5.
6. Paton, B.E. (1952) Self-regulation of arc in consumable electrode welding. *Avtomatich. Svarka*, **1**, 38-45.
7. Clarke, D.W., Montadi, C., Tuffs, P.S. (1987) Generalized predictive control. Part 1: The basic algorithm. *Automatica*, **27**(2), 137-148.
8. Tomizuka, M., Tsao, T., Chew, K. (1989) Analysis and synthesis of discrete-time repetitive controllers. *ASME J. Dynamic Systems, Measurement and Control*, **111**(3), 357-359.
9. Goodwin, G., Tsyppkin, Ya.Z. (1992) Robust control systems with inner model. *Doklady AN Ukrainy*, **333**(4), 640-644.
10. Tsyppkin, Ya.Z. (1996) Synthesis of structure of stabilizing and invariant regulators. *Ibid.*, **347**(5), 607-609.
11. Tsybulkin, G.A. (1998) About compensation of influence of welding condition instability on evaluation of electrode deviation from fusion line of parts being welded. *Avtomatich. Svarka*, **4**, 50-52.
12. Tsybulkin, G.A. (2002) To the question of GMAW stability. *The Paton Welding J.*, **5**, 14-16.
13. Ivakhnenko, A.G. (1961) Connection between invariance theory and theory of differential regulators. *Avtomatika*, **1**, 3-25.
14. Mensky, B.M. (1961) On problem of realisation of invariance principle. *Izvestiya AN SSSR. Energetika i Avtomatika*, **5**, 80-86.
15. Kukhtenko, A.I. (1963) *Invariance problem in automation*. Kiev: Gostekhzdat.
16. Zajtsev, G.F., Steklov, V.K. (1984) *Automatic systems with differential feedbacks*. Kiev: Tekhnika.
17. Tsyppkin, Ya.Z. (1996) Stochastic discrete systems with inner models. *Problemy Upravl. i Informatiki*, **1/2**, 21-26.



STUDY ON THE EFFECT OF PULSED GTAW PROCESS PARAMETERS ON BEAD GEOMETRY OF THE AISI 304L STAINLESS STEEL WELDS

P.K. GIRIDHARAN¹ and N. MURUGAN²

¹Amrita Institute of Technology, India

²Coimbatore Institute of Technology, India

A study on the effect of pulsed gas tungsten arc welding (GTAW) parameters on weld bead geometry was carried out for welding of the 304L stainless steel sheets of 3 mm thickness. Autogenous welding with square butt joint was employed. The advantages of pulsed GTAW process, such as controlled heat input, increased depth to width ratio and less distortion etc., can be achieved only when the welding parameters were thoroughly studied, controlled and optimized through mathematical models. Hence, mathematical models were developed correlating the important controllable pulsed GTAW process parameters like pulse current, pulse duration and welding speed with weld bead parameters, such as penetration, bead width, aspect ratio and bead area of the weld. A design of experiments based on central composite rotatable design was employed. The developed models were found to be adequate based on regression and ANOVA analysis. The models were validated by plotting scatter diagram and by conducting confirmation test. Weld bead parameters predicted by the models were found to confirm with observed value with high accuracy. Using these models, the main and interaction effects of pulsed GTAW parameters on weld bead parameters can be studied. Optimization of the process parameters was also carried out to obtain optimum bead parameters using quasi-newtonian numerical optimization technique. Results of the optimization were also presented in this paper.

Keywords: pulsed GTAW process, welding of stainless steel sheets, mathematical models, design of experiments, ANOVA analysis, optimization

Pulsed GTAW process is suitable for joining thin and medium thickness materials like stainless steel sheets etc. and for the applications where metallurgical control of the weld metal is critical. With the increased use of mechanized welding, the selection of welding parameters and welding procedure must be more specific to ensure that the weld bead parameters of good quality is obtained at minimum cost and with high repeatability.

In pulsed GTAW process, welding current is pulsed between high and low level of short or long time interval, so that it brings weld zone to melting point during pulse current period and allows molten weld pool to be cooled and solidified during the background current period. The weld bead shape will be series of overlapping weld spots and the amount of overlap depends upon the pulse frequency and welding speed [1]. Pulsed current GTAW process parameters are depicted in Figure 1. The stainless steel weld produced by the pulsed GTAW process should have good mechanical properties and corrosion resistance in addition to have appropriate weld bead geometry [2]. One of the major problems in welding of thin austenitic stainless steel sheets is variation in penetration of the weld from weld-to-weld and heat-to-heat of the base metal. Presently addition of filler materials was employed to control the variation in penetration, and it was recommended to use stainless steel sheets having sulphur content less than 0.008 % for automated welding in order to control the variation in weld penetration [1].

Selection of optimum pulsed GTAW process parameters combination to obtain optimum bead parameters using sequential experimentation for welding of thin stainless steel sheets was reported [3–7]. A report on design of experiments using five factor three-level full factorial design for bead-on-plate weld (304 type stainless steel) was available. But report on correlation between welding process parameters and bead parameters using mathematical models for welding of thin stainless steel sheets was not available [5]. Hence, an attempt was made to predict and optimize the weld bead parameters using mathematical models.

Statistically designed experiment based on central composite rotatable design with full factorial technique was employed for the development of mathematical models [8–10]. Response surface methodology was used for the study of main and interaction effects of welding process parameters on weld bead parameters. Optimization of welding process parameters was carried out to optimize the bead parameters of the weld. In the optimization, bead area was considered as the objective function (for minimum heat input)

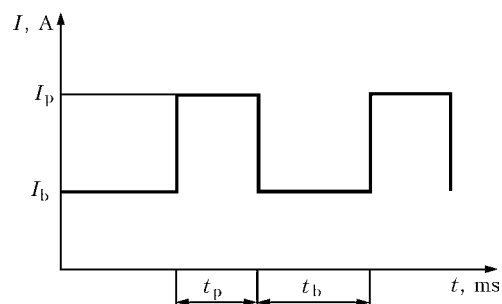


Figure 1. Pulsed GTAW process parameters at $F = 1(t_p + t_b)$ Hz: I_b --- base current, A; I_p --- pulse current, A; t_b --- base current duration, ms; t_p --- pulse current duration, ms

**Table 1.** Pulsed GTAW process variables

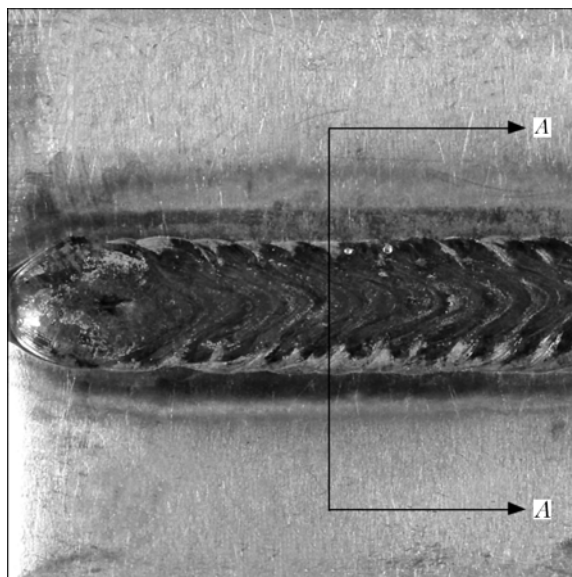
Process variable levels	I_p , A	t_p , ms	v_w , cm/min
-1.628	180	450	11
-1	188	490	12.6
0	200	550	15
1	212	610	17.4
1.628	220	650	19

and other weld bead parameters like width, penetration and aspect ratio and its limits as constraints.

Experimental procedure. AISI 304L type austenitic stainless steel sheets of size $100 \times 50 \times 3$ mm were welded autogenously with square butt joint without edge preparation. The chemical composition of steel used was as follows, wt. %: 0.017C, 10.1Ni, 18.71Cr, 0.22Si, 1.64Mn, 0.027P, 0.047S, 0.015N, 69.224Fe. The experiments were conducted using ESSETI-UNIMACRO 501C pulse TIG/MIG welding machine (Italy). Industrial pure and commercial grade argon was used as shielding gas and for back purging, respectively.

The fixed pulsed GTAW process parameters and their values were as follows: 1 Hz pulse frequency; 2 mm arc length; 14 V mean arc voltage; tungsten electrode diameter of 2.4 mm; electrode vertex angle of 60° ; argon flow rate of 10 l/min for shielding and of 5/1 l/min for back purging. Automatic voltage control available in the welding equipment was used. The voltage and current readings indicated by the equipment were used for heat input calculation. Fixture variation effects were not considered due to the same setup was being used throughout the experiment.

Independently controllable process parameters (pulse current I_p , pulse current duration t_p , and welding speed v_w) were identified to carry out the experimental work and to develop the mathematical models.

**Figure 2.** Typical pulsed GTAW welded specimen showing the location of cross sectioning

The ratio between base current and pulse current is maintained as 0.2 through out the experiments.

Trial runs were conducted to find the limits of each controllable process parameters, so as to obtain full penetration weld, free from any visible defects. Because of computational ease and enhanced interpretability of the models, parameters were converted to coded form for developing mathematical models, drawing graphs and for further analysis of the results. The upper limit of a factor was coded as +1.682 and lower limit as -1.682. The coded value for intermediate values was calculated from the following relation [10]:

$$X_i = (3.364\{(X - X_{\min}) / (X_{\max} - X_{\min})\} - 1.682), \quad (1)$$

where X_i is the required coded value of X ; X is any value of the variable from X_{\min} to X_{\max} ; X_{\min} and X_{\max} are the lower and upper limits of the variable X , respectively. The decided level of process variables with their levels, units and notations for pulsed GTAW are given in Table 1.

A central composite rotatable three factor five-level full factorial experimental design consisting of 20 runs was used [9, 10]. Experiments were conducted at random to avoid systematic error creeping into the experimental procedure.

During the trial run, it was observed from the welded plates that penetration was at minimum between the two pulses, i.e. at the location of maximum bead overlap. Hence, by ensuring full penetration at maximum bead overlap location, full-penetration weld can be achieved for entire length of the weld. So welded plate was cross-sectioned at the location A-A (maximum bead overlap) for the measurement of weld bead parameters (Figure 2).

The welded specimens of 10 mm wide were cut and mounted using Bakelite, polished and electrolytically etched with 10 % oxalic acid solution for revealing the macrostructure. A photomicrograph of a typical weld specimen cross-sectioned at A-A showing the bead profile is presented in Figure 3. The weld bead profiles were traced and the bead dimensions, such as bead width W , depth of penetration P and weld bead area BA , were measured by using an optical profile projector and a digital planimeter. Aspect ratio AR (bead width/penetration depth) was calculated from the measured value of bead width and depth of penetration.

Heat input is also very important factor, which affects the bead geometry, mechanical and metallur-

**Figure 3.** Photomicrograph of a typical weld specimen cross-sectioned at A-A showing bead profile ($\times 10$)



gical properties and corrosion resistance of weld. Hence, heat input was also included in the study. The heat input per unit length is proportional to voltage and current, as well as inversely proportional to welding speed. Unlike continuous current GTAW process, where heat input is calculated from continuous current, in pulsed GTAW heat input is calculated from the mean current using the following equation:

$$I_{\text{mean}} = \frac{I_p t_p I_b t_b}{t_p + t_b} \text{ (A)}. \tag{2}$$

Heat input in pulsed GTAW is calculated using the equation

$$HI = (I_{\text{mean}} U / v_w) \eta \text{ (kJ/mm)}, \tag{3}$$

where U is the mean voltage; η is the welding process efficiency.

For pulsed GTAW process, arc efficiency is taken as 60 %. During the experiment, voltage was found to vary from 13.4 to 14.6 V. Hence, a mean voltage of 14 V is taken for heat input calculation. The observed value of bead width, bead area, penetration depth, calculated values of aspect ratio and heat input for pulsed GTA-welded specimens with the design matrix, are given in Table 2.

Development of mathematical model. Procedure based on regression was used for the development of mathematical models and to predict the weld bead geometry [11].

The response surface function representing any of the weld bead geometry can be expressed as $Y = f(I_p, t_p, v_w)$ and the relationship selected being a second-order response surface as follows [10]:

$$Y = b_0 + b_1 I_p + b_2 t_p + b_3 v_w + b_{11} I_p^2 + b_{22} t_p^2 + b_{33} v_w^2 + b_{12} I_p t_p + b_{13} I_p v_w + b_{23} t_p v_w, \tag{4}$$

where b_0 – b_3 are the constant term and coefficients of linear terms, respectively; b_{11} , b_{22} , b_{33} are the coefficients of second order square terms; b_{12} , b_{13} and b_{23} are the coefficients of second order interaction terms.

Coefficients of the above polynomial equation were calculated by regression equations [10]:

$$b_0 = 0.166338 ((\sum X_0 Y) - 0.05679 (\sum \sum X_{ij} Y)); \tag{5}$$

$$b_i = 0.073224 (\sum X_i Y); \tag{6}$$

$$b_{ii} = 0.0625 ((\sum X_{ii} Y) + 0.006889 (\sum \sum X_{ij} Y) - 0.056791 (\sum X_0 Y)); \tag{7}$$

$$b_{ij} = 0.125000 (\sum X_{ij} Y), \tag{8}$$

where X_i , X_{ii} and X_{ij} are the values of first order, second order square and interaction terms of the process parameters considered for the study; Y is the observed response.

Initially mathematical models were developed using the following coefficients obtained from above equations:

Table 2. Design matrix and observed values of bead parameters and heat input

Specimen code	Pulsed GTAW parameters			Depth of penetration P , mm	Bead width W , mm	Bead area BA , mm ²	Aspect ratio AR	Heat input HI , kJ/mm
	I_p , Å	t_p , ms	v_w , cm/min					
S1	-1	-1	-1	2.36	8.79	12.04	3.725	0.75
S2	1	-1	-1	3.54	9.77	20.93	2.760	0.83
S3	-1	1	-1	3.40	9.24	18.88	2.718	0.87
S4	1	1	-1	3.85	9.80	23.29	2.545	0.97
S5	-1	-1	1	1.66	7.75	7.85	4.668	0.54
S6	1	-1	1	2.98	8.54	13.50	2.866	0.60
S7	-1	1	1	2.37	8.18	10.94	3.451	0.63
S8	1	1	1	3.43	9.33	18.15	2.720	0.70
S9	-1.682	0	0	1.90	7.89	8.62	4.153	0.66
S10	1.682	0	0	3.59	9.52	19.40	2.652	0.78
S11	0	-1.682	0	1.85	7.58	8.68	4.097	0.63
S12	0	1.682	0	3.73	8.79	22.50	2.357	0.81
S13	0	0	-1.682	3.84	10.26	24.66	2.672	0.98
S14	0	0	1.682	1.95	8.385	8.95	4.300	0.57
S15	0	0	0	3.45	9.10	18.44	2.638	0.72
S16	0	0	0	3.78	8.62	20.01	2.280	0.72
S17	0	0	0	3.48	9.14	20.63	2.626	0.72
S18	0	0	0	3.48	9.08	20.91	2.609	0.72
S19	0	0	0	3.84	8.73	21.58	2.273	0.72
S20	0	0	0	3.83	8.75	19.76	2.285	0.72



Table 3. Comparison of square multiple *R* values and standard error of estimate for full and reduced models

Bead parameter	Adjusted square multiple <i>R</i>		Standard error of estimate	
	Full model	Reduced model	Full model	Reduced model
<i>P</i>	0.887	0.888	0.262	0.261
<i>W</i>	0.886	0.904	0.237	0.218
<i>BA</i>	0.899	0.919	1.766	1.583
<i>AR</i>	0.877	0.888	0.264	0.252

$$P = 3.637 + 0.502I_p + 0.415t_p - 0.431v_w - 0.278I_p^2 - 0.262t_p^2 - 0.225v_w^2 - 0.124I_p t_p + 0.094I_p v_w - 0.024t_p v_w; \quad (9)$$

$$W = 8.897 + 0.456I_p + 0.273t_p - 0.509v_w - 0.028I_p^2 - 0.212t_p^2 + 0.19v_w^2 - 0.007I_p t_p + 0.05I_p v_w + 0.092t_p v_w; \quad (10)$$

$$AR = 2.46 - 0.454I_p - 0.404t_p + 0.344v_w - 0.284I_p^2 + 0.222t_p^2 + 0.314v_w^2 + 0.233I_p t_p - 0.174I_p v_w - 0.183t_p v_w; \quad (11)$$

$$BA = 20.205 + 3.243I_p + 2.942t_p - 3.743v_w - 2.087I_p^2 - 1.528t_p^2 - 1.099v_w^2 - 0.365I_p t_p - 0.055I_p v_w - 0.183t_p v_w; \quad (12)$$

$$HI = 0.72 + 0.037I_p + 0.055t_p - 0.12v_w - 0.001I_p^2 - 0.001t_p^2 - 0.019v_w^2 + 0.004I_p t_p - 0.006I_p v_w - 0.009t_p v_w. \quad (13)$$

Significance of the coefficients was tested using *t*-test [12] and also by backward elimination method available in SYSTAT software package [13]. Final models were developed by using significant coefficients only after eliminating the insignificant coefficient with the associated response without sacrificing much of the accuracy.

The developed models were checked for adequacy by regression analysis. The values of adjusted square multiple *R* and standard error of estimate for both the full and reduced models are given in Table 3. It was found that the reduced models were better than the full models as reduced models have higher values of adjusted square multiple *R* and lesser values of standard error of estimate than those of respective full models. The adequacy of developed models was also

tested by analysis of variance technique ANOVA [14]. The results of analysis of variance are presented in Table 4. It is evident from the Table that all models are adequate.

Final mathematical models with process parameters in coded form as determined by regression analysis:

$$P = 3.637 + 0.502I_p + 0.419t_p - 0.433v_w - 0.276I_p^2 - 0.265t_p^2 - 0.226v_w^2; \quad (14)$$

$$W = 8.874 + 0.456I_p + 0.273t_p - 0.509v_w - 0.209I_p^2 + 0.193v_w^2; \quad (15)$$

$$AR = 2.46 - 0.454I_p - 0.404t_p + 0.344v_w - 0.284I_p^2 + 0.222t_p^2 + 0.314v_w^2 + 0.233I_p t_p - 0.174I_p v_w; \quad (16)$$

$$BA = 20.205 + 3.243I_p + 2.942t_p - 3.743v_w - 2.087I_p^2 - 1.528t_p^2 - 1.099v_w^2; \quad (17)$$

$$HI = 0.72 + 0.037I_p + 0.055t_p - 0.12v_w - 0.001I_p^2 - 0.001t_p^2 - 0.019v_w^2 + 0.004I_p t_p - 0.006I_p v_w - 0.009t_p v_w. \quad (18)$$

Model validation. Conformity tests were conducted with the same experimental setup to validate the accuracy of the models. The results of the conformity test are presented in Table 5. From the conformity test it was found that developed models were able to predict the bead parameters with a reasonable accuracy. The validity of the model was tested again by drawing scatter diagrams, which show the degree of closeness between observed and predicted values of weld bead dimensions. A typical scatter diagram for bead area is shown in Figure 4.

Bead area optimization. As welding process is a multi-objective problem (full penetration, minimum weld bead area, minimum bead width for good quality bead and maximum welding speed for higher productivity etc.), the optimum solution is a compromise [15, 16]. The developed models were used for optimization of pulsed GTAW parameters to obtain optimum weld bead geometry. Bead area is an important weld bead parameter, which in turn controlled by other bead parameters, such as penetration depth, bead width and aspect ratio. A good control over weld bead area leads to minimum heat input, better control on

Table 4. Results of ANOVA analysis

Bead parameter	1st order term		2nd order term		Lack of fit		Error term		<i>F</i> -ratio	<i>R</i> -ratio
	Sum of squares	Degree of freedom								
<i>P</i>	8.332	3	2.561	6	0.505	5	0.1829	5	2.76	33.08
<i>W</i>	7.103	3	7.396	6	0.303	5	0.2597	5	1.16	18.80
<i>BA</i>	453.2	3	98.270	6	26.860	5	5.9178	5	4.54	59.77
<i>AR</i>	6.648	3	3.445	6	0.517	5	0.1790	5	2.89	31.32



Table 5. Results of conformity of experimental and predicted values

Test No.	Process parameter			Penetration P , mm			Bead width W , mm		
	I_p , A	t_p , ms	v_w , cm/min	Predicted values	Observed values	Error, %	Predicted values	Observed values	Error, %
1	200	550	17	3.11	2.98	-4.27	8.58	8.77	2.19
2	212	603	17.14	3.45	3.31	-4.15	9.11	9.23	1.37
3	211.4	537.65	16.51	3.40	3.28	-3.53	9.00	9.17	1.91
Mean error							Mean error		
-3.98							1.82		

Table 5 (cont.)

Test No.	Aspect ratio AR			Bead area BA , mm ²		
	Predicted values	Observed values	Error, %	Predicted values	Observed values	Error, %
1	2.971	2.943	-0.96	16.28	17.051	4.73
2	2.721	2.788	2.45	18.51	19.017	2.74
3	2.572	2.795	-2.03	16.63	16.014	-3.70
Mean error					Mean error	
-0.18					1.25	

Note. Error, % = (observed value - predicted value) / predicted value.

other bead geometry and also optimum use of welding power source.

The limits of constraints were selected based on trial runs. From the trial runs, weld bead width less than 9 mm, penetration greater than 3.4 mm, aspect ratio in the range of 2.5 to 3.0 and bead area in the range of 15 to 20 mm² were ensured for a good weld bead geometry with full penetration. So limits of constraints for bead width and bead area were considered less than 9 mm and between 15 to 20 mm², respectively, whereas for aspect ratio and penetration respectively greater than 2.5 and 3.4 mm were considered as their respective constraint values.

In the optimization, bead area was taken as objective function, and penetration, bead width, aspect ratio and bead area with its limits as constraint equations. By minimizing the bead area, heat input would be minimum leading to optimum use of process parameter and power. Optimization method considered is a nonlinear constrained minimization problem solved using quasi-newtonian numerical optimization technique [16], which is well suited for second order equation and also simple, efficient and fast [17, 18]. For optimization, objective function and constraint equations were used.

Optimization tool available in MATLAB Version 7 (Release-14, 2004) software package was used for optimization. Software tool «Solver» available in Microsoft Excel 2000 was also used for solving the optimization and found to confirm the results obtained from MATLAB Software package. The results of optimization were as follows: $I_p = 211.4$ A, $t_p = 537.65$ ms and $v_w = 16.51$ cm/min. Optimized bead parameters are $P = 3.4$ mm, $W = 9$ mm, $AR = 2.572$, and $BA = 17.89$ mm².

Pulsed GTAW parameters were set near to the predicted optimum process parameter values and conformity test was conducted. The results obtained were found to confirm the predicted and observed optimum bead parameters with high accuracy.

Results and discussion. Mathematical models were developed correlating important pulsed GTAW parameters with the weld bead geometry for welding of the 304L austenitic stainless steel thin sheets.

The possible causes for the main and interaction effects of different pulsed GTAW parameters on the weld bead parameters were analyzed and are presented graphically in Figures 5-9. The graphs constructed with the help of the developed models provide satisfactory explanations about the effect of the welding

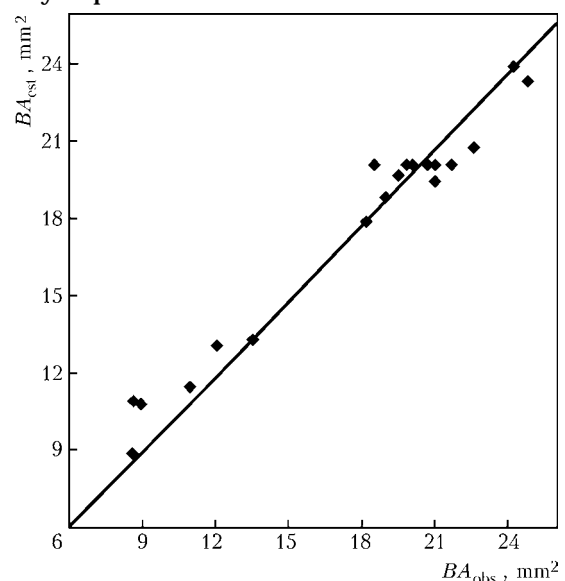


Figure 4. Scatter diagram for bead area model

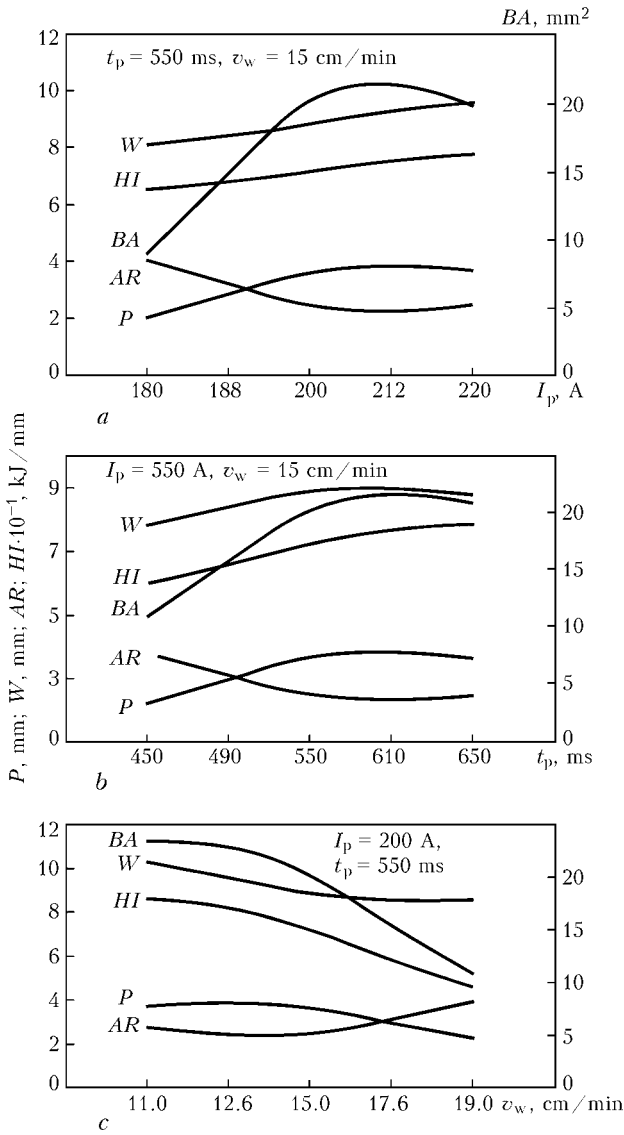


Figure 5. Direct effect of pulse current I_p (a), pulse current duration t_p (b) and welding speed v_w (c) on bead parameters

process parameters on various bead parameters. Contour and response surface plots were drawn for interaction effects using SYSTAT software package [13] to visualize their nature.

The effects of heat input on bead parameters were also included in the study using the heat input model, shown in equation (18). From the mathematical equations (14), (15) and (17), it is clear that there is no

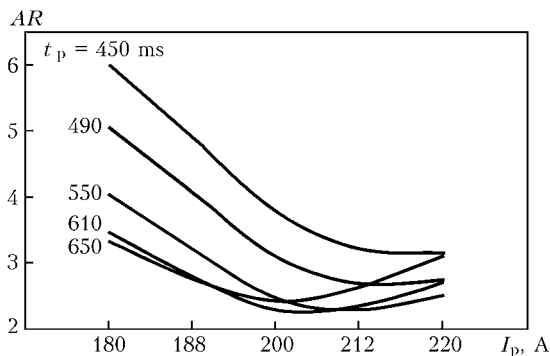


Figure 6. Interaction effect of pulse current I_p and pulse current duration t_p on aspect ratio AR at $v_w = 15$ cm/min

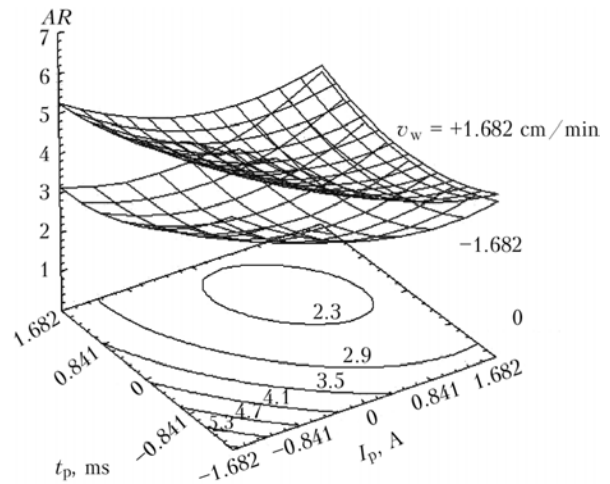


Figure 7. Response surface and contour plot for interaction effect of pulse current I_p and pulse current duration t_p on aspect ratio AR

interaction effect of the process parameter on P , W and BA . Whereas from equation (16), it is evident that AR has interaction effects.

Direct effects. Direct effects of pulse current I_p on weld bead parameters and heat input HI . It is evident from Figure 5, a, that as I_p is increased from 180 to 220 A, HI and W increase steadily from 0.65 to 0.78 kJ/mm and from 8.107 to 9.641 mm, respectively. P and BA increase significantly from 2.01 to 3.86 mm and from 8.84 to 21.36 mm², respectively, as I_p is increased from 180 to 212 A and further increase in I_p beyond 212 A, P and BA decrease less significantly to 3.7 mm and 19.75 mm², respectively. Whereas AR initially decreases significantly from 4.02 to 2.29 as I_p increases to 212 A and then increases less significantly to 2.5 as I_p is increased to 220 A. AR decreases due to significant increase in P compared to W as I_p is increased, and AR increases due to significant increase in W compared to P as I_p increases further. The rate of increase of BA is high as I_p increases from 180 to 212 A and this may be due to the significant increase in both P and W . So, it is clear that increase in I_p had positive effect on W and HI , mixed effect on AR , BA and P .

Direct effects of pulse current duration t_p on weld bead parameters and heat input HI . It is evident from Figure 5, b, that as t_p increases from 450 to 650 ms HI increases steadily from 0.59 to 0.78 kJ/mm. W , P and BA increase significantly from 7.82 to

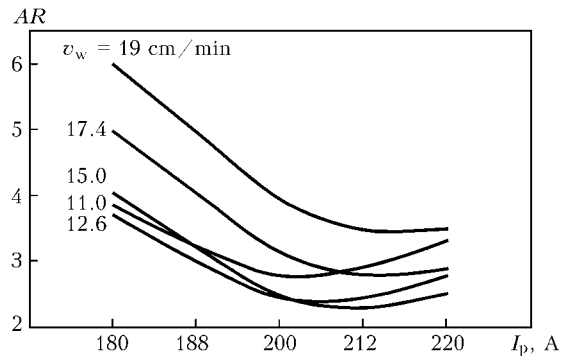


Figure 8. Interaction effect of pulse current I_p and welding speed v_w on aspect ratio AR at $t_p = 550$ ms



8.938 mm, 2.18 to 3.79 mm and 10.93 to 21.62 mm², respectively, as t_p increases from 450 to 610 ms, and then all the bead parameters decrease less significantly as t_p increases beyond 610 ms. W initially increases significantly as t_p increases to 550 ms and further increase in t_p beyond 550 ms, and there is no significant change in W due to constant arc zone width. AR initially decreases significantly from 3.76 to 2.27 as t_p increases to 610 ms and then increases less significantly to 2.41 showing similar trend as in Figure 4. BA also has similar trend as I_p on BA as shown in Figure 5, a, but with lesser magnitude indicating the less influence of t_p on BA compared to I_p . Hence, increase in t_p has positive effect on W and HI , and mixed effects on AR , BA and P .

Direct effects of welding speed v_w on weld bead parameters and heat input HI . It is apparent from Figure 5, c, that as v_w is increased from 11 to 15 cm/min, HI , AR and BA decreases less significantly, P increases slightly, and further increase in v_w beyond 15 cm/min leads to significant decrease in P , BA and HI . W initially decreases significantly from 10.276 to 8.87 mm, as v_w is increased from 11 to 15 cm/min and further increase in v_w beyond 15 cm/min, and there is no significant change in W . AR initially decreases less significantly from 2.77 to 2.46 as v_w is increased to 15 cm/min, and AR increases significantly to 3.927 on further increase in v_w beyond 15 cm/min. It is obvious that as v_w increases, HI to base metal decreases, hence less melting of base metal leading to decrease in all the bead parameters. Initial decrease in AR may be due to significant decrease in W compared to P as v_w increased from 11 to 15 cm/min. But slight increase in AR as v_w is increased beyond 15 cm/min may be due to decrease in HI leading to significant decrease in P compared to W . Hence, increase in v_w has negative effect on P , BA and W , and positive effect on AR .

Interaction effects. Interaction effect of pulse current I_p and pulse current duration t_p on aspect ratio AR . Figure 6 shows the interaction effect of I_p and t_p on AR . It is apparent that as I_p is increased from 180 to 200 A, AR decreases significantly for all value of t_p and further increase in I_p to 220 A, no significant change in AR is observed when t_p increases from 450 to 490 ms and AR increases less significantly for t_p above 550 ms. The initial decreasing trend of AR may be due to the predominant effect of I_p on AR and later increasing trend of AR may be due to the predominant effect of t_p on AR . It is also observed that AR is maximum when I_p and t_p are at their minimum levels, whereas AR is minimum when I_p and t_p are at 200 A and 610 ms, respectively, and v_w is 15 cm/min. Hence, effect of increasing t_p has predominant effect on AR as I_p is increased beyond 200 A. These effects are also reflected in response surface and contour plots (Figure 7). Response surface shows that AR increases as v_w changes from minimum to maximum level for all values of I_p and t_p . AR is maximum

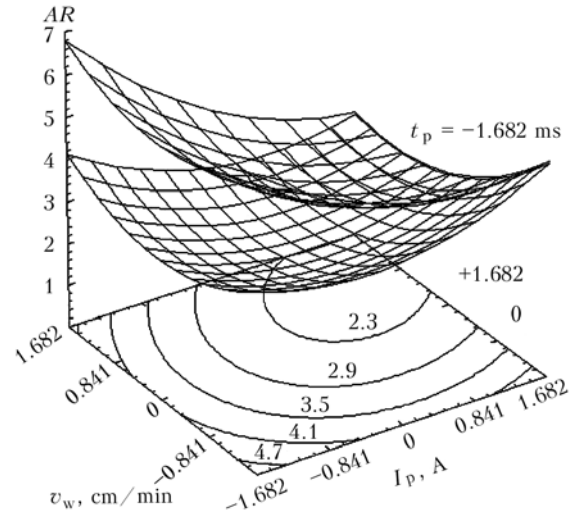


Figure 9. Response surface and contour plot for interaction effect of pulse current I_p and welding speed v_w on aspect ratio AR

when I_p and t_p are at their minimum levels and v_w is at maximum level.

Interaction effect of pulse current I_p and welding speed v_w on aspect ratio. It is evident from Figure 8, which shows the interaction effect of I_p and v_w on AR . It is observed that AR is maximum when I_p and v_w are at their minimum and maximum levels, respectively, whereas AR is minimum when I_p and v_w are at 212 A and 15 cm/min, respectively. It is apparent that as I_p is increased from 180 to 200 A, AR initially decreases significantly for all values of v_w and further increase in I_p beyond 200 A, AR increases less significantly as v_w is decreased from 15 to 11 cm/min, whereas AR becomes more or less steady when v_w is decreased from 19 to 17.4 cm/min. Hence, it is clear that increase of I_p from 180 to 200 A has predominant effect on AR , whereas decrease of v_w has predominant effect on AR as I_p is increased from 200 to 220 A. These effects are also visualized in Figure 9, which shows the response surface and contour plots for the interaction effect of I_p and v_w on AR . From the Figure it is evident that AR decreases as t_p is changed from minimum to maximum level for all values of I_p and v_w . AR is maximum when I_p , t_p and v_w are at 180 A, 450 ms and 19 cm/min, respectively.

CONCLUSIONS

1. Response surface methodology can be employed to visualize the effect of pulsed GTAW process parameters on weld bead parameters for welding of the 304L stainless steel thin sheets.

2. A five-level full factorial technique can be employed for developing mathematical models to predict the weld geometry within the workable region of process parameters.

3. Penetration model developed was found to predict the penetration with 96 % accuracy, whereas models of bead width, bead area and aspect ratio were found to predict their respective bead parameters with 98 % accuracy based on conformity test.



4. It is found that pulse current have positive effect on bead width, whereas mixed effects on penetration and bead area. Pulse current duration has mixed effects on penetration, bead width and bead area, whereas welding speed has negative effect on penetration, bead width and bead area.

5. Optimum pulsed GTAW parameters for welding of the 304L stainless steel sheets 3 mm thick are pulse current of 211.4 A, pulse current duration of 537.65 ms and welding speed of 16.51 cm/min at a frequency of 1 Hz.

6. Optimized bead parameters predicted by the models are as follows: $P = 3.4$ mm, $W = 9$ mm, $AR = 2.572$, and $BA = 17.89$ mm².

7. MATLAB Software package can be effectively used for optimization of pulsed GTAW parameters for welding of stainless steel thin sheets.

Acknowledgement. The authors thank All India Council of Technical Education and UGC for providing financial assistance for the project. We also thank Mr. K.R. Ananthanarayanan, A.G.M., (P.A.D.), Stainless Steel Plant, S.A.I.L., Salem, India, for providing stainless steel sheets for conducting the experiments successfully.

- Cornu, J. (1988) *Advanced welding system, TIG and related processes*. Vol. 3. Springer.
- Murugan, N., Parmar, R.S., Sud, S.K. (1993) Effect of submerged arc process parameters on dilution and bead geometry in single wire surfacing. *J. Material Proc. Technol.*, **37**, 767–780.
- Lothongkum, G., Chaumbai, P., Bhandhubanyong, P. (1999) TIG pulse welding of 304L austenitic stainless steel in flat, vertical and over head position. *Ibid.*, **89/90**, 410–414.
- Troyer, W., Tomsic, M., Barhorst, R. (1977) Investigation of pulsed wave shapes for gas tungsten arc welding. *Welding J.*, **56(1)**, 26–32.
- Omar, A.A., Ludin, C.D. (1979) Pulsed plasma — pulsed GTA arc: A study of process variables. *Ibid.*, **58(4)**, 97–105.
- Lothongkum, G., Viyanit, E., Bhandhubanyong, P. (2001) TIG pulse welding parameters of the AISI 316L stainless steel plate at the 6–12 h positions. *J. Material Proc. Technol.*, **91/92**, 312–316.
- Leitner, R.E., Mcelhinney, G.H., Pruitt, E.L. (1973) An investigation of pulsed GTA welding variables. *Welding J.*, **52(9)**, 405–410.
- Hames, P., Smith, B.L. (1993) Factorial techniques for weld quality prediction. *Metal Construction*, **15**, 128–130.
- Adler, Y.P., Markov, E.V., Granovsky, Y.V. (1975) *Design of experiments to find optimal conditions*. Moscow: Mir.
- Cochran, W.G., Cox, G.M. (1957) *Experimental designs*. John Wiley & Sons.
- Murugan, N., Parmar, R.S. (1994) Effects of MIG process parameters on the geometry of bead in automatic surfacing of stainless steel. *J. Material Proc. Technol.*, **41**, 381–398.
- Gunaraj, V., Murugan, N. (2000) Prediction and optimization of weld bead volume for submerged arc process. Part 1. *Welding J.*, **79(10)**, 286–294.
- (2004) SYSTAT, Version 11. Systat Inc.
- Montgomery, D.C., Peck, E.A. (1992) *Introduction to linear regression analysis*. New York: John Wiley & Sons.
- Jashir, S.A. (1989) *Introduction to optimum design*. New York: McGraw-Hill.
- Arora, J.S. (1989) *Introduction of optimum design*. New York: McGraw-Hill.
- Gill, P.E., Murray, W. (1981) *Practical optimization*. New York: Academic Press.
- Gunaraj, V., Murugan, N. (2000) Prediction and optimization of weld bead volume for submerged arc process. Part 2. *Welding J.*, **79(11)**, 331–294.

TECHNOLOGY, MATERIALS AND METHODS OF CONSTRUCTION OF INTRICATE MONUMENTAL SCULPTURES



Sculpture «Motherland», the museum of the Great Patriotic War of 1941–1945, Kiev

Technology has been developed for manufacture of monumental sculptures from stainless steel. In 1981 on the Dnieper river bank in Kiev an all-welded sculpture «Motherland» of 115 m total height was constructed. The more than 15-year experience of service showed the high reliability and serviceability of the structure.

Technology and taken technological solutions allow creation of monumental structures of any sizes, including the art masterpieces of intricate three-dimensional shape.

Purpose and application. Civil engineering.

Status and level of development. Technology and structures were tested in practice.

Proposals for co-operation. Any forms of cooperation, contracts on use of technology and assistance in construction of monumental sculptures.

Main developers and performers: Prof. Yushchenko K.A., Lead. Eng. Fomin V.V.

Contacts: Yushchenko K.A.
E-mail: Tel./fax: 289 22 02



DEPENDENCE BETWEEN THE RATES OF PULSED WIRE FEED AND WIRE MELTING IN WELDING WITH SHORT-CIRCUITING

V.A. LEBEDEV

E.O. Paton Electric Welding Institute, NASU, Kiev, Ukraine

Mathematical model is considered, describing the dependence of the arc process current and the rate of melting of electrode wire on the varying nature of its motion in the process of consumable electrode arc welding, in particular, in short-circuiting of the arc gap.

Keywords: arc welding, mechanized process, electrodes, pulses, melting rate, welding current, mathematical model

Ever greater attention has been paid recently to mechanized-arc welding with a pulsed impact on the process due to current pulses coming from special sources (pulsed-arc process) or application of pulsed electrode wire feed. These actions offer certain advantages compared to stationary (undisturbed) processes.

A number of materials have been published in technical literature which consider the problems related to technological features of application of pulsed wire feed [1] and technical means of implementation of such a motion [2]. However, insufficient attention is paid to investigations related to studying the influence of a changing feed rate on the arc process parameters, in particular, such an important characteristic as the electrode wire melting rate. Knowledge of these regularities is required both for determination of the parameters of wire motion into the arcing zone and of elements of control of the process of electrode metal transfer into the weld pool, and for evaluation of the influence of disturbances in the feed system (deviations in the feed rate compared to assigned values) on weld formation and characteristics of the welding process as a whole.

The purpose of this study is derivation of an analytical dependence between the electrode wire feed rate and its melting rate at a varying nature of wire motion, in particular, for the case of specially used pulsed feed.

In study [3] an equation was derived which correlates the welding current and electrode wire feed rate for the process of gas-shielded consumable-electrode arc welding with short-circuiting of the arc gap:

$$\frac{L}{R_{eq} + 0.5b} \frac{d^2 I_w}{dt^2} + \frac{dI_w}{dt} + \frac{AHE_w I_w}{R_{eq} + 0.5s} = \frac{v_f E_c}{R_{eq} + 0.5s}, \quad (1)$$

where L is the welding circuit inductance; R_{eq} is the equivalent resistance of the welding circuit; E_c is the electric field intensity in the arc column; b is the coefficient characterizing the slope of the static arc characteristic to the current axis; $A = 1/\pi R_{eq}^2 M$; $H =$

$= U_{0.-c} (0.285 - 0.0052 U_{0.-c})$; $U_{0.-c}$ is the open-circuit voltage; $M = C_m \gamma_m T_m - C_{amb} \gamma_{amb} T_{amb} + r_m \gamma_m$; C_m , C_{amb} is the metal heat capacity at melting and ambient temperatures, respectively; γ_m , γ_{amb} is the metal density at melting and ambient temperatures, respectively; r_m is the latent heat of melting; T_m , T_{amb} is the electrode metal melting and ambient temperature, respectively.

This equation is quite complicated to solve and use in selection of parameters of controlled pulsed feed. For simplification, let us convert it into a form, convenient for solving by the methods of operator calculus, assuming that the electrode wire feed rate v_f is the input action, and the arc process current I_w is the output action:

$$\frac{I_w(p)}{v_f(\partial)} = \frac{E_c / (R_{eq} + 0.5s)}{T_1 p^2 + p + k}, \quad (2)$$

where p is the differential calculus operator; $T_1 = L / (R_{eq} + 0.5s)$; $k = AHE_c / (R_{eq} + 0.5s)$.

Equation (2) in the operator form is the transfer function of the system of welding current source --- mechanized welding process with short-circuiting of the arc gap. Influence of electrode wire feed rate on welding current can be studied by assigning different wire motion laws.

Let us consider a sinusoidal change of the feed rate as one of the most widely spread laws, purposefully realized by means of pulsed feed mechanisms. This law (Figure 1, a) can be written in the form of

$$v_f = V_f | \sin \omega t |, \quad (3)$$

where V_f is the amplitude value of the feed rate; ω is the pulse repetition rate.

Proceeding from equation (3) and data of study [4] it is possible to find the operator form image of the input value which is the electrode wire feed rate. In this case, however, the solution (searching for an original) of the equation in the operator form when searching for the output value (welding current I_w) will be rather complicated and cumbersome.

Let us simplify the problem, and consider in detail the form of feed pulses, obtained when using the real mechanism of pulsed feed and impulse passage along

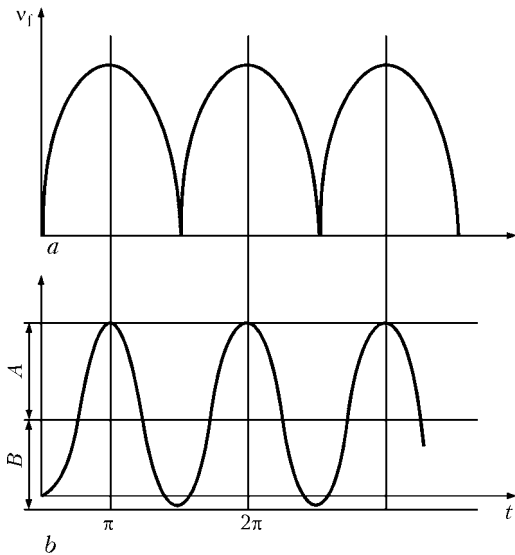


Figure 1. Calculated (a) and close to the real one (b) forms of feed pulses

the guiding channel. The considered pulses, as a rule, do not have any abrupt transitions (this is the result of play and features of pulse formation in the feed mechanism and lagging in the guiding channel, features of pulse formation with the reversing motion of electrode wire). Proceeding from analysis of real oscillograms of feed rate [5], the formalized shape of the pulse can be presented in the form shown in Figure 1, b. For this case, presentation of the image of the initial value (rate of pulsed feed of electrode wire) in the following form will be valid:

$$v_f(p) = \frac{(A + B)\omega}{p^2 + \omega^2}, \quad (4)$$

where A and B are denoted in Figure 1.

Proceeding from equations (2) and (4) let us present the image of welding current I_w in the following form:

$$I_w(p) = \frac{(A + B)D\omega}{(p^2 + \omega^2)(T_1 p^2 + p + k)} = \frac{(A + B)D\omega}{T_1 p(p^2 + \omega^2) [p^2 + (p/T_1) + (k/T_1)]}, \quad (5)$$

where $D = E_c / (R_{eq} + 0.5s)$.

Equation (5) can be solved moving from the image of the output value $I_w(p)$ to its original $I_w(t)$, i.e. $I_w(p) = I_w(t)$, here the most rational way to find the above transition is to use the tables of operator images [6]. The following formula is the closest to the tabulated one:

$$F(p) = \frac{1}{(p^2 + c^2) [(p + a)^2 + b^2]},$$

$$f(t) = \frac{1}{\sqrt{(\delta^2 - c^2)^2 + 4a^2 c^2}} \times \left[\frac{1}{c} - \sin(ct - \lambda) + \frac{1}{b} e^{-at} \sin(bt - \mu) \right], \quad (6)$$

where

$$\lambda = \arctg \frac{2\alpha c}{\delta^2 - c^2}; \quad \mu = \arctg \frac{-2ab}{a^2 - b^2 + c^2}; \quad \delta^2 = a^2 + b^2.$$

Equating the respective coefficients of the denominators of equations (5) and (6), we will obtain the following expressions for definition of a , b and c :

$$a = 1/2T_1; \quad a^2 + b^2 = k/\hat{O}_1; \quad (7)$$

$$b = (\sqrt{4kT_1 - 1})/2T_1; \quad c = \omega.$$

In expressions (7) value b determines the frequency of forced oscillations of the welding current source-arc process system.

It should be noted that at pulsed feed the integral rate of electrode wire feed is connected with the feed rate in the pulse by the following dependence:

$$v_f = f(t) = \xi h, \quad (8)$$

where ξ , h is the pulse feed frequency and pitch, respectively.

Considering that the pitch recommended in [7] is related to electrode wire diameter d_{el} by dependence $h = 1.2d_{el}$, we will write equation (8) in the following form:

$$v_f = (1.2-1.4) d_{el} \xi, \quad (9)$$

It is known that the integral feed rate v_f at a harmonic law of its variation (see equation (3)) is related to amplitude value by the following dependence:

$$v_f = \frac{1}{\pi} \int_0^{T/2} V_f \sin \omega t = \frac{2}{\pi} V_f, \quad (10)$$

where T is the feed pulse repetition rate.

Amplitude value of feed rate v_f , allowing for (9) and (10), can be presented in the following form:

$$V_f = \pi(1.2-1.4) d_{el} \xi / 2 \approx 2 d_{el} \xi. \quad (11)$$

Allowing for the constant co-multipliers of equation (5), B , D and T_1 , as well as the fact that variations of electrode wire feed rate are shifted relative to abscissa axis by value

$$B = k_{sh} V_f, \quad (12)$$

where k_{sh} is the value characterizing the feed pulse shape, in the final variant we will obtain the sought dependence $I_w(t)$ for the case of pulsed feed of electrode wire:

$$I_w(t) = \frac{BD}{T_1 \sqrt{(\delta^2 - c^2)^2 + 4a^2 c^2}} + \frac{(A + B)D}{T_1 \sqrt{(\delta^2 - c^2)^2 + 4a^2 c^2}} \times \left[\sin(ct - \lambda) + \frac{c}{b} e^{-at} \sin(bt - \mu) \right]. \quad (13)$$

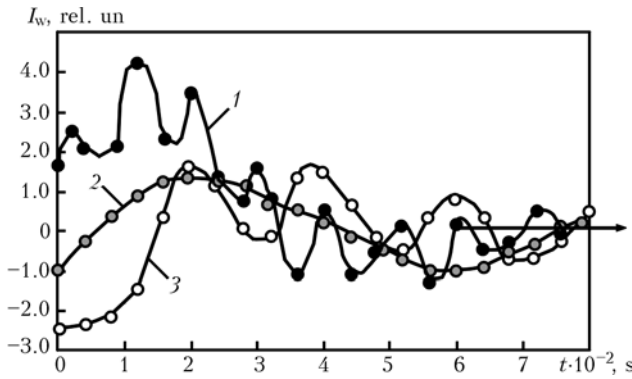


Figure 2. Relative variations of welding current at pulsed feed of electrode wire with a sinusoidal nature of motion ($b = 14 \text{ s}^{-1}$): 1 — $c = 100$; 2 — 14; 3 — 50 s^{-1}

Equation (13) is the mathematical model, which analytically describes the dependence between the wire feed rate varying by a harmonic law and welding current. This model is valid for investigation of an isolated feed pulse, but as the process with short-circuits is periodic and with correctly selected pulsed feed parameters [8] its frequency corresponds to the pulse repetition rate, the proposed approach to description of the above dependence should be regarded as acceptable.

Preliminary analysis of equation (13) shows that at pulsed feed of electrode wire the current in the welding circuit is of an oscillatory nature, but the frequency and amplitude of these oscillations is simultaneously determined by two components: as a consequence of variation of wire feed rate and as a result of asymptotically attenuating oscillatory transient processes in electrode wire melting.

Parameters of welding current fluctuations when using the pulsed feed of electrode wire were calculated on the basis of equation (13). These calculations are shown in the graphic form in Figure 2.

As was to be anticipated, at different frequencies of pulsed feed and transient process, their resultant value depends on a quite large number of parameters, as well as the features of electrode wire melting in the arc process using the consumable electrode, welding current source characteristics and welding circuit parameters.

An important feature is that variations (fluctuations) of welding current due to a pulsed nature of wire motion and oscillatory transient process, run not synchronously with the variation of the electrode wire feed rate, but with certain (calculated) shift from them for a time dependent on the characteristics of the above system, as well as the considerable excess of welding current at the initial moment of the action of the feed pulse over its fluctuations in the steady-state mode. The latter was assumed to be hypothetical in welding with short-circuiting of the arc gap for evaluation of the levels of current variation, depending on the feed rate.

Considering that the rate of electrode wire melting v_m follows the welding current variations in an inertialess manner and is proportional to it, as well as

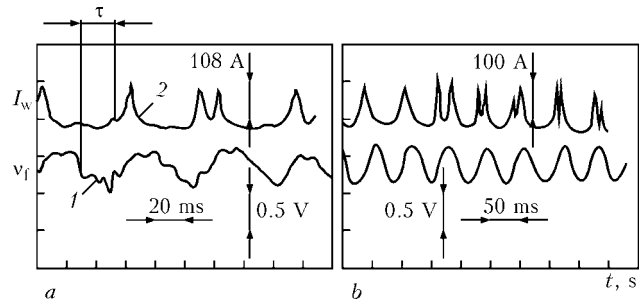


Figure 3. Oscillograms of synchronous recording of the rate of electrode wire pulsed motion (1) and arc process current (2): a — $c = 20 \text{ s}^{-1}$; b — 30 s^{-1} ; b — $c = 20 \text{ s}^{-1}$; b — 20 s^{-1}

allowing for equations (8), (12) and (13), the final equation relating the electrode wire feed rate and its melting rate can be presented in the following general form:

$$v_m(t) = \frac{k_I f \pi D / 2}{T_1 \sqrt{(\delta^2 - c^2)^2 + 4a^2 c^2}} \times \left\{ \frac{1}{2} + \left[\sin(ct - \lambda) + \frac{c}{b} e^{-at} \sin(bt - \mu) \right] \right\}, \quad (14)$$

where k_I is the coefficient of proportionality characterizing the degree of dependence $v_m = f(I_w)$, which, as a rule, is assumed to be directly proportional.

The most convincing example, confirming the results of the conducted investigation, is existence of forced short-circuits of the arc gap with pulsed feed frequency as a consequence of wire melting by the law assigned by the pulsed feed with its inherent accelerations in electrode wire melting in each pulse and arc gap closing by the drop at the moment of the pulse action. Figure 3 gives the experimentally derived characteristic oscillograms of synchronous recording of the rate of the wire pulsed motion, reproduced by the feed mechanism with the sinusoidal law of formation and arc process current. Lagging of the pulse in the guiding channel, corresponding to the conclusions of study [9], in this experiment is excluded, because of the maximum closeness of the device for recording the feed rate to the area of arc process running. A certain phase shift τ between the electrode wire feed rate and arc current is visible, and a difference in the shape of welding current curve is noticeable at different values of c and b parameters.

CONCLUSIONS

1. Pulsed nature of electrode wire feed has an essential influence on the arc process current, and, consequently, on electrode wire melting rate causing their oscillations.
2. Parameters of welding current oscillation and electrode wire melting rate at its pulsed motion are due both to the characteristics of pulsed feed with their periodical action, and characteristics of the welding current-arc process system, which are an aperiodic transient process.
3. Obtained mathematical model describing in the analytical form the dependence between the electrode wire feed rate and its melting rate, can be used for



calculation of the conditions of electrode metal transfer at purposefully assigned pulses, as well as for evaluation of the influence of deviations in the feed rate, arising for different reasons, on welded joint formation.

1. Voropaj, N.M. (1996) Parameters and technological capabilities of arc welding with pulse feed of electrode and filler wire. *Avtomatich. Svarka*, **10**, 3–9.
2. Lebedev, V.A., Moshkin, V.F., Pichak, V.G. (1996) New mechanisms for pulsed feed of electrode wire. *Ibid.*, **5**, 39–44.
3. Popkov, A.M. (1980) About stability of the power supply–arc system in welding with systematic short-circuiting of the arc gap. *Svarochn. Proizvodstvo*, **3**, 11–13.
4. Besekersky, V.A., Popov, E.P. (1972) *Theory of automatic regulation*. Moscow: Nauka.
5. Paton, B.E., Lebedev, V.A., Pichak, V.G. et al. (2002) Analysis of technical and technological capabilities of electrode wire pulsed feed in arc welding and surfacing processes. *Svarochn. Proizvodstvo*, **2**, 24–31.
6. Ditkin, V.A., Kuznetsov, P.I. (1951) *Refer. book on operational calculus*. Leningrad: Gostekhteorizdat.
7. Potapievsky, A.G. (1974) *Consumable-electrode gas-shielded arc welding*. Moscow: Mashinostroenie.
8. Lebedev, V.A., Pichak, V.G. (1998) Mechanized CO₂ arc welding with controlled pulsed feed of electrode wire. *Svarochn. Proizvodstvo*, **5**, 30–33.
9. Lebedev, V.A. (1999) Influence of guiding channel of semi-automatic welding machine on parameters of electrode wire pulsed feed. *Avtomatich. Svarka*, **2**, 45–48.

PECULIARITIES OF STRUCTURE AND PROPERTIES FORMATION IN 10Kh13G18D STEEL FUSION ZONE

A.I. GEDROVICH¹, A.N. TKACHENKO², S.A. TKACHENKO², A.T. ZELNICHENKO³,
I.I. ALEKSEENKO³ and V.L. BONDARENKO⁴

¹V. Dal East Ukrainian State University, Lugansk, Ukraine

²«HC Luganskteplovoz», Lugansk, Ukraine

³E.O. Paton Electric Welding Institute, NASU, Kiev, Ukraine

⁴«Fronius Ukraine» Company, Knyazhichi, Kiev region, Ukraine

Peculiarities of the reaction of austenitic steel 10Kh13G18D in the form of cold-rolled stock to the thermodeformational cycle of arc welding are considered. The nature of phase transformations in the fusion zone of steel 10Kh13G18D in similar and dissimilar joints with steel 09G2S is shown. Reduction of welding heat input prevents to a considerable degree the metal softening in the fusion zone of welded joints and reduces the probability of precipitation of δ -ferrite in this zone.

Keywords: arc welding, chromium-manganese steel, welded joints, fusion zone, phase transformations, δ -ferrite, softening, welding heat input

Austenitic chromium-manganese 10Kh13G18D steel (DI61) was designed [1] for application as corrosion-resistant material when manufacturing consumer goods, medical equipment, food machine-building products, heat-exchange equipment and other products that are in contact with mildly aggressive media. Ukraine has the experience of its application in the form of thin cold-rolled stock for the sheathing of diesel and electric trains in «HC Luganskteplovoz» [2]. In the process of carriage road tests, as well as their operation in the railways under alternating and dynamic loads, cases of cracks initiation and propagation in the fusion zone (FZ) of welded joints were found both in 10Kh13G18D steel and in its joints with 09G2S steel (from the side of 10Kh13G18D steel). As a result, atmospheric moisture penetrates into the fracture sections, development of local corrosion and deterioration of the metal product aesthetics is observed.

As earlier noted [3], formation of α -martensite in the amount of 1–2 vol.% was observed in FZ of welded joints of cold-deformed sheets of 10Kh13G18D steel produced by mechanized CO₂ welding with Sv-08Kh20N9G7 austenitic wire. Considerable residual tensile stresses developing in the welding zone under

the influence of welding thermal deformation cycle promote its appearance [3]. Reduction of α -martensite content was noted in HAZ metal of the joints with welded billets ageing, as a result of stress relaxation in them and loss of stability of geometrical dimensions. Simultaneous lowering of the strength and ductile properties of the metal in FZ is the result of structural transformations in welding. So, the bending angle of welded joints does not exceed 90–100°, and tensile specimens fail in FZ. The above properties can only be increased under the conditions of forced cooling of the joints during welding, achieved through application of special cooling reagents and devices [3]. In this case, decrease of α -martensite fraction in FZ metal to 0.5 % and the increase of joint ductility is achieved. Unfortunately, it is not clear from the above-mentioned, what leads to a simultaneous decrease of strength and ductility properties of the metal in the joint FZ under the impact of the thermal cycle of welding (α -martensite formation in FZ should be accompanied by increase of strength properties of the metal in this section).

The purpose of this work is getting a deeper insight into the reasons for embrittlement of 10Kh13G18D steel welded joints and suggesting the ways of welding technology optimization on this basis.

At the beginning the properties and peculiarities of austenitic 10Kh13G18D steel application were ana-



lyzed. After optimal heat treatment (quenching at heating temperature of 1000–1050 °C and cooling in water) it is not inferior to chromium-nickel steels of 18-10 type as to adaptability-to-fabrication [1]. Lowering of quenching temperature (to 860 °C, for example) increases σ_t from 670 up to 780 MPa, $\sigma_{0.2}$ from 300 up to 360 MPa, reduces the indices of ductility and toughness. The degree of quenched steel plastic deformation in cold rolling of thin sheets has the same influence. For example, at 20 % reduction, σ_t reaches 910, $\sigma_{0.2}$ --- 790 MPa at $\delta = 30$ %. The increase of the degree of plastic deformation can be the reason of martensite transformation in steel and abrupt lowering of ductility properties.

Thus, the use of high strength properties of cold deformed sheets from 10Kh13G18D steel a priori is attractive for designers and developers from the point of view of realization of reduction of welded structure weight. At the same time, one can anticipate a violation of austenite solid solution stability with such an initial state of the metal at further technological processing that in its turn can influence the physico-chemical properties of steel welded joints, their adaptability-to-fabrication and operation properties.

In view of the above prerequisites, single-pass butt welded joints of work-hardened 10Kh13G18D steel 1.5 mm thick of the following chemical composition, wt. %: 0.11 C; 0.45 Si; 17.01 Mn; 13.22 Cr; 1.39 Ni; 0.022 S; 0.03 P; 0.80 Cu, were studied in the work. Single-pass overlap joints of this steel 1.5 mm thick with 09G2S steel 2.5 mm thick, were also made. The variants of the used technologies of welding are given in Table 1. The value of welding heat input was calculated [4], residual stresses in the welded joints were determined by electron speckle-interferometry [5].

The samples of the joint cross-sections were first cut by the center of the weld to separate the joint section from 09G2S steel side. Prepared microsections were subjected to electrolytic etching in solution of 5 % H₂SO₄. Metallographic examinations were conducted using light microscope «Neophot-32» and microhardness meter PMT-3. Structural heterogeneity and phase composition of the joints were assessed using the JEOL scanning electron microscope JSM-840 fitted with MicroCapture image grabber with the following image recording on the computer screen, and ferrometer «Ferritgehaltmesser 1.53» (scale range of 0–1, 0–3 and 0–12 vol.%).

Experimental results. The results of tensile testing of samples are given in Table 1. Similar (10Kh13G18D + 10Kh13G18D) and dissimilar (10Kh13G18D + 09G2S) joints made by semi-automatic CO₂ welding demonstrate the lowest fracture resistance. In both the cases, fracture is located in FZ, and in the second case --- from the side of 10Kh13G18D steel. A noticeable increase of strength properties is observed at deposition of the technological bead along the FZ of the metal of the weld with 10Kh13G18D steel, as well as when using welding technologies with a low heat input (pulsed welding and cold metal transfer process --- CMT). Definite correlation is noted between the content of magnetic component in FZ joints, sample rupture force and welding heat input. A higher content of the magnetic phase in FZ (4.5 and 2.5 vol.%) and larger heat input value (3350 J/cm) correspond to the minimum force of fracture of joints 1 and 2 of Table 1. The content of magnetic phase in FZ is equal to 0.1–0.2 and 0.5–0.8 vol.%, respectively, under the conditions of pulsed

Table 1. Technologies and welding modes when making experimental single-pass joints

Joint number	Steels to be welded	Joint type, welding technology (welding modes) and heat input	Average rupture strength of the joints, MPa	Fracture site
1	10Kh13G18D + 10Kh13G18D	Butt; semi-automatic in CO ₂ with Sv-08Kh20N9G7 wire Ø1.2 mm ($I_w = 110-120$ A; $U_a = 20-21$ V; $v_w = 16-18$ m/h); $q_w = 3350$ J/cm	15293	FZ
2	10Kh13G18D + 09G2S	Overlap; semi-automatic in CO ₂ with Sv-08Kh20N9G7 wire Ø1.2 mm ($I_w = 110-120$ A; $U_a = 20-21$ V; $v_w = 16-18$ m/h); $q_w = 3350$ J/cm	17262	FZ from the 10Kh13G18D side
3	10Kh13G18D + 09G2S	Overlap; the same + technological bead with nonconsumable electrode in argon on the fusion line of the weld metal with steel 10Kh13G18D from the joint face ($I_w = 60-65$ A; $U_a = 10-12$ V; $v_w = 17-18$ m/h)	18023	09G2S base metal
4	10Kh13G18D + 09G2S	Overlap; automatic pulsed argon-arc welding in the «Fronius» robotic complex TRS 5000 CMT ($I_w = 178$ A; $U_a = 19.8$ V; $v_w = 90$ m/h; $v_f = 4$ m/min); $q_w = 1190$ J/cm	18000	HAZ from the 09G2S side
5	10Kh13G18D + 09G2S	Overlap; automatic «cold» welding (CMT-process [6]) in CO ₂ on robotic complex TRS 5000 CMT ($I_w = 99$ A; $U_a = 24.6$ V; $v_w = 46.8$ m/h; $v_f = 4$ m/min); $q_w = 1320$ J/cm	1826	Weld metal
6	10Kh13G18D + 09G2S	Overlap; semi-automatic «cold» welding (CMT-process [7]) in argon on the «Fronius» semi-automatic machine TRS 2700 CMT ($I_w = 106$ A; $U_a = 15.9$ V; $v_w = 38.2$ m/h; $v_f = 3.2$ m/min); $q_w = 1105$ J/cm	1863	10Kh13G18D base metal far from the HAZ

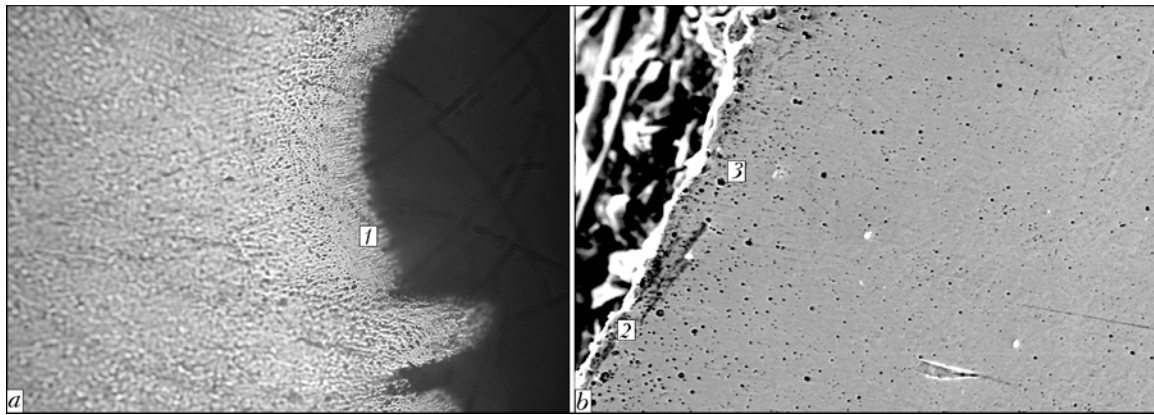


Figure 1. Microstructure of 10Kh13G18D steel butt joint metal after tensile tests from the side of weld metal (*a* — $\times 400$) and from the side of steel (*b* — $\times 1500$): 1–3 — phase analysis sections

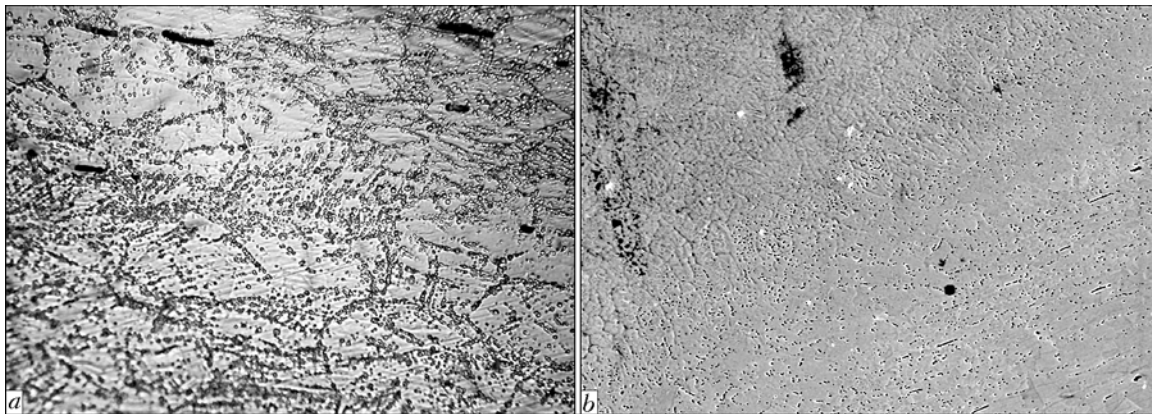


Figure 2. Microstructure in FZ of 10Kh13G18D steel in 10Kh13G18D + 09G2S joints with different intensity of δ -ferrite precipitation: *a* — mechanized CO₂ welding ($\times 1000$); *b* — CMT-process ($\times 500$)

Table 2. Content of alloying elements, wt.%, in structural components of FZ metal in 10Kh13G18D + 09G2S joints from the side of austenitic steel

Object of analysis	Cr	Ni	Mn	Cu
Solid solution of austenitic matrix:				
section 1, Figure 1, <i>a</i>	12.26	5.92	4.26	0.323
section 2, Figure 1, <i>b</i>	13.35	1.16	16.19	0.755
Phase precipitation (section 3, Figure 1, <i>b</i>)	23.08	1.06	13.10	0.580

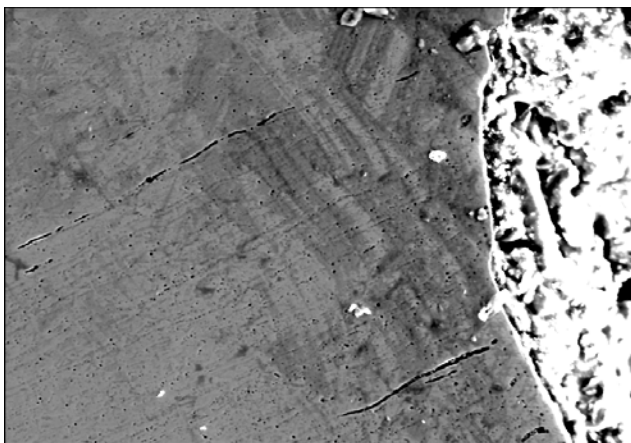


Figure 3. Microstructure of tensile specimen of 10Kh13G18D + 09G2S joint with line δ -ferrite precipitates ($\times 300$)

welding and CMT-process. In 10Kh13G18D steel proper, the magnetic phase is absent at a distance from the welding zone, and only in the local sections its content is up to 0.01 vol.%.

When Sv-08Kh20N9G7 wire is used, the weld metal contains the magnetic component in the form of δ -ferrite in the amount from 0.7–1.2 (joint 1) up to 0.7–10.0 vol.% (joint 3 of Table 1) in all the technology variants.

Microsections were cut out of the samples failing along FZ (joint 2 of Table 1) for assessment of both the composition of solid solution of the metal at the fracture boundary and its separate structural phases with 1 μ m locality (Figure 1). The results of evaluation of alloying elements distribution in the joint, summed up in Table 2, indicate that the sample fails along the FZ of the metal of the weld with the adjacent high-temperature section of the HAZ of 10Kh13G18D

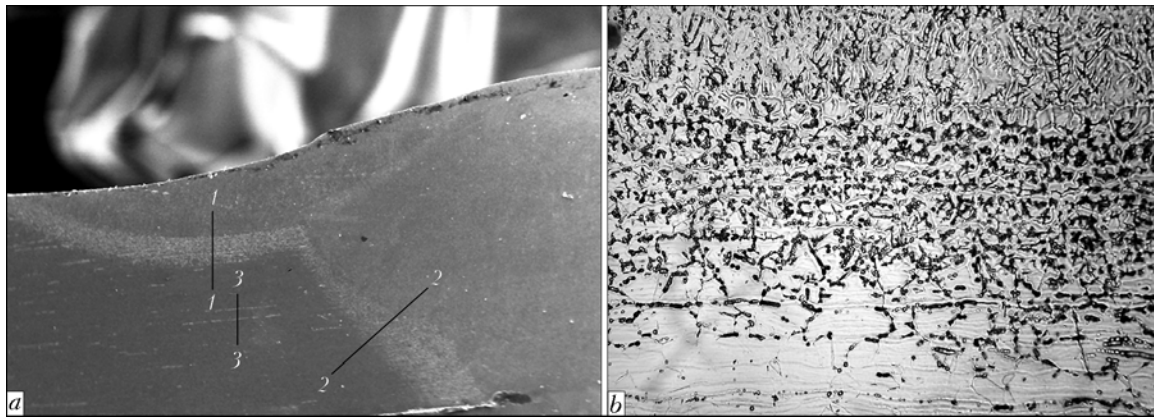


Figure 4. Macrostructure of a fragment of 10Kh13G18D + 09G2S welded joint with the main weld and technological bead (*a* — $\times 60$), and microstructure of FZ of the technological bead with 10Kh13G18D steel (*b* — $\times 500$): 1-1, 2-2, 3-3 — sections of microhardness measurement

Table 3. Microhardness (*HV* 0.2) distribution across the sections of phase instability

Section of microhardness measurement (Figure 4)	Weld		FZ	Base metal	Line precipitation
	Main	Technological			
1-1	--	232-260	216-241	232-241	--
2-2	229-280	--	232-274	221-244	--
3-3	--	--	--	232-234	171-183

steel. Precipitation of the second phase enriched in chromium is found in the latter under the influence of the thermal cycle of welding that allows identifying it as high-temperature δ -ferrite. As noted above, the intensity of the second phase precipitation in FZ correlates with the welding heat input (Figure 2). Precipitations (Figure 3) observed in the local sections of 10Kh13G18D steel (usually along the rolled metal lines) also are δ -ferrite, and are indicative of a certain metallurgical prehistory of the metal.

Deposition of the technological bead (joint 3, Table 1) by a nonconsumable electrode in argon along the line of fusion of the weld metal with 10Kh13G18D steel introduces certain corrections into formation of structural inhomogeneity (Figure 4). Judging by FZ metal etchability in the microsection, high-temperature δ -ferrite appears in FZ of both the main and technological weld. The width of precipitation zone is equal to 0.10-0.25 mm.

Appearance of δ -ferrite is determined by structural instability of the austenitic solid solution in 10Kh13G18D steel at heating (even for a short time) above 1200-1250 °C. On the other hand, it is obvious from Figure 4 that no FZ is found in the points where the technological weld (the composition of which corresponds to 10Kh13G18D steel, cast state) crosses the main weld (made with Sv-08Kh20N9G7 wire). The found peculiarities testify that when making the technological bead on cast chromium-nickel-manganese austenitic weld under the influence of thermodeformational welding cycle, no changes in phase composition are observed, unlike $\gamma \rightarrow \gamma + \delta$ transformations in the metal of FZ with 10Kh13G18D steel. Micro-

hardness distribution in the metal across the sections of phase instability (sections 1-1, 2-2 and 3-3 in Figure 4) is given in Table 3. At load lowering to 25 g, *HV* 0.2 in the section of δ -ferrite precipitate accumulation is equal to 203-258, and in the matrix (austenite solid solution) it is 172-190.

It is characteristic that when the technological bead is deposited, lowering of the residual stresses is achieved in the welded joints of 10Kh13G18D + 09G2S near the welding zone (Figure 5).

Discussion of the experimental data. From our viewpoint, the cause and effect relationship can be established between the embrittlement of welded joints of 10Kh13G18D steel in service and loss of the joint strength properties under the unfavourable weld-

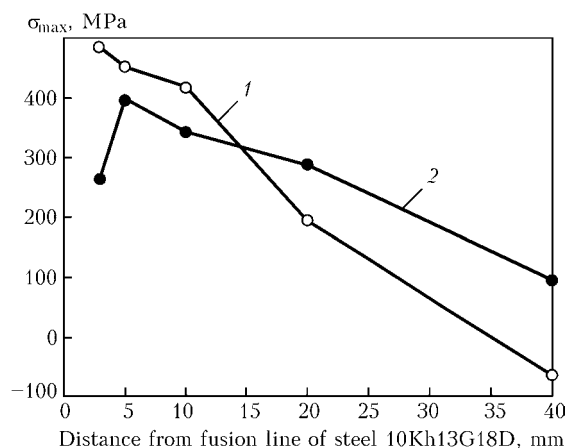


Figure 5. Longitudinal stresses in the transverse direction of overlap 10Kh13G18D + 09G2S welded joints after welding (1) and after technological bead deposition (2)



ing conditions. Metal of the cold rolled stock of 10Kh13G18D steel, depending on the initial chemical composition, austenitization mode, stage of deformation in rolling, i.e. its metallurgical prehistory, acquires different degrees of stability. It is manifested both in formation of line δ -ferrite precipitations in the austenitic matrix of the base metal, and in variation of the strength and ductile properties of the rolled metal delivered to «HC Luganskteplovoy». So, in accordance with certificates on the delivered sheet, their σ_t varies in the range of 670–850, $\sigma_{0.2}$ — 390–430 MPa, and relative elongation δ_5 — 54–64 %, respectively. Phase transformation $\gamma \rightarrow \gamma + \delta$ runs actively under the conditions of arc welding even at a short-time heating of steel above the temperature of 1200–1250 °C due to the diffusion nature of redistribution of chemical elements and, primarily, chromium. As a result, stable existence of the second phase (δ -ferrite) is observed. Appearance of δ -ferrite in the austenitic base, particularly in the amount of 2–8 vol.%, usually has no influence on the physico-mechanical properties of the metal. Furthermore, δ -ferrite presence in austenitic structure of weld metal abruptly suppresses the possibility of its hot cracking [8], which is actually achieved by application of Sv-08Kh20N9G7 wire for welding of 10Kh13G18D steel and its joints with 09G2S steel. However, δ -ferrite appearance in FZ of 10Kh13G18D steel joints has certain peculiarities. As the 10Kh13G18D steel strength properties in the cast state (technological weld metal) and weld metal produced using Sv-08Kh20N9G7 wire, are lower than those of the deformed 10Kh13G18D rolled stock, appearance of δ -ferrite in FZ metal is indicative of the process of rolled metal weakening and stress relaxation in it.

Lowering of specific heat input in welding or use of other (for example, technological) techniques for shortening the time of the metal staying in the overheated state, will promote preservation of phase stability of the base metal in FZ with the weld and preservation of higher strength properties, respectively. The same is also true for ductile properties of the joint FZ metal. On the contrary, appearance of δ -ferrite and the associated chromium redistribution

in FZ metal structure can be accompanied by development of microchemical heterogeneity (depletion in chromium of austenitic grain sections adjacent to δ -ferrite grains). The latter can provoke violation of austenite stability in these grain sections and lead to appearance of secondary martensite capable of lowering the ductile properties of the metal in this zone.

CONCLUSIONS

1. It was established that cold rolled stock in the form of 10Kh13G18D steel sheet is characterized by a metastable state.

2. Precipitation of δ -ferrite, accompanied by metal weakening in this zone, is observed under the influence of high temperature heating (above 1200–1250 °C) in FZ of 10Kh13G18D steel.

3. Limiting of the specific heat input in welding and shortening of the time of steel overheating improves the physical-mechanical properties of the welded joints.

4. Existence of cause-effect relationship between the joint FZ properties after welding and service properties of welded structures was suggested.

1. Ulianin, E.A. (1991) *Corrosion-resistant steels and alloys*. Moscow: Metallurgiya.
2. Tkachenko, A.N., Gedrovich, A.I., Galtsov, I.A. (2002) Application of metastable corrosion-resistant steel 10Kh13G18D as sheathing for cars of electric and diesel multiple-unit trains. In: *Proc. of Int. Conf. on Welding and Related Technologies* (Kiev, April 22–26, 2002). Kiev: PWI, 56–57.
3. Galtsov, I.A. (2005) *Improvement of the quality of metal structures from metastable steel 10Kh13G18D by welding with forced cooling*: Syn. of Thesis for Cand. of Techn. Sci. Degree. Mariupol.
4. Denisov, Yu.A., Kocheneva, G.I., Maslov, Yu.A. et al. (1982) *Reference book of the welder*. Ed. by V.V. Stepanov. Moscow: Mashinostroenie.
5. Lobanov, L.M., Pivtorak, V.A., Savitsky, V.V. et al. (2005) On-line determination of residual stresses using the electron speckle-interferometry. *V Mire Nerazrush. Kontrolya*, **1**, 10–13.
6. (2004) Arc welding with pulse feed of electrode wire — CMT process proposed by Fronius Society. *Avtomatich. Svarka*, **12**, 55–58.
7. (2006) Cost effectiveness comes first. *Weld + Vision*, 16–17.
8. Medovar, B.I. (1966) *Welding of austenitic steels and alloys*. Kiev: Tekhnika.



INFLUENCE OF THERMOPHYSICAL CONDITIONS OF WELDING ON FRACTURE RESISTANCE OF THE HAZ METAL IN THE JOINTS OF ALUMINIUM ALLOY V96tss

T.M. LABUR, A.Ya. ISHCHEKNO, T.G. TARANOVA, V.A. KOSTIN, G.M. GRIGORENKO and A.A. CHAJKA
E.O. Paton Electric Welding Institute, NASU, Kiev, Ukraine

Considered is the influence of volume fraction, morphology and composition of particles containing zirconium and scandium on fracture resistance characteristics of the HAZ metal of a high-strength complex-alloyed aluminium alloy V96tss in fusion arc and electron beam welding.

Keywords: arc and electron beam welding, aluminium alloy, welding heating, nonconsumable electrode, electron beam, heat-affected zone, structure, volume fraction of particles, fracture resistance

V96tss alloy of Al-Zn-Mg-Cu alloying system is a new modification of V96 alloy and is characterized by high values of mechanical properties [1-3]. High specific strength characteristic of alloys of this alloying system allows them to be used for the airframe skins and stiffeners (spar booms). These mainly are riveted joints of structural elements, as these are difficult-to-weld alloys.

Presence of zirconium and scandium in the alloys increases the temperature of aluminium recrystallization, accelerates the solid solution decomposition during subsequent thermal operations with formation of finely-dispersed particles of intermetallic phases [4-6]. They not only strengthened the alloy, but also prevent development of recrystallization during heating in welding. Such nonmetallic inclusions (NMI) are located along the boundaries and through the grain bulk. These phases coagulate during welding, this influencing the properties of welded joints [7].

It is known that presence of coarse phases, which are located along the grain boundaries, lowers the ductility, fracture toughness, and resistance to cracking in service [8-11]. They also are the cracking sites at failure of structural materials, irrespective of their shape (plate-like, acicular, etc.). All this makes it necessary to thoroughly take into account the dimensions and amount of the phases under the conditions of welding heating, as the amount of NMI is one of the most important indices of the quality of metals and their welded joints, on which the properties and service reliability depend.

Thermal conditions of two processes of joining aluminium alloys widely used in fabrication of light-weight structures --- nonconsumable electrode arc (TIG) and electron beam (EB) welding were selected, in order to study the structural processes running in the metal in welding. Air and water media were used to simulate the conditions of sample cooling in welding (10-20 and 30-50 °C/s), respectively [12].

Mechanical testing of the samples was conducted at off-center tension, when the metal is simultaneously exposed to uniaxial tension and bending. Testing simulated the work of typical structural elements and met the technical requirements of GOST 25.506. Experiments were conducted in all-purpose RU-5 machine, this allowing, in addition to studying the structure of welded joint HAZ metal, to also determine the characteristics of fracture resistance of its individual sections, and by the results establish the influence of the nature of distribution of particles, containing zirconium and scandium, their volume fraction on the conditions and parameters of crack initiation and propagation. Measurements of microhardness of the studied samples were performed from the notch tip along the line of the avalanche crack propagation (Table 1).

Quantitative estimate of the volume fraction of particles in the structure of the studied alloy V96tss was conducted using ImagePro 30 computer program, which allows separating the typical structural elements based on colour contrast. Subsequent mathematical processing was conducted using Statistica 5.0 program. The derived results were used to plot the graphic dependencies of the influence of volume fraction of NMI on the physico-mechanical properties of the structures characteristic of various sections of the HAZ metal. Scanning electron microscope JSM-840 was used for structural analysis of particles precipitating in welding heating and cooling, as well as the features of fracture relief.

Analysis of the data in Table 1 shows that distribution of NMI volume fraction in the studied alloy samples under the conditions of overheating simulating the metal condition in the fusion zone, nonuniformly depends on the distance to the notch tip. NMI volume fraction in the overheated condition (550 °C, 3 s) of V96tss alloy is equal to 1.94-2.42 %, i.e. their scatter is 20 %.

Alloy heating up to the quenching condition (460 °C, 1 h) with subsequent cooling in water, increases the scatter up to 30 %. NMI volume fraction somewhat decreases here, and is equal to 1.12-1.72 %. Sample cooling from the temperature of quenching in



Table 1. Change of NMI volume fraction, %, in V96tss alloy after heat treatment allowing for the distance from the notch tip

Distance from the notch tip, mm	Kind of heat treatment							
	Overheating	Quenching (water)	Quenching (air)	Annealing (water)	Annealing (air)	Tempering	Ageing	Initial condition
0	2.19	1.12	3.96	3.84	6.77	1.70	1.37	1.49
3	2.42	1.72	5.45	4.84	3.56	2.37	2.35	1.03
6	2.12	1.22	3.62	3.94	3.59	2.68	2.84	1.32
9	1.94	2.35	2.94	4.64	5.04	3.10	2.32	2.19
12	2.35	1.59	2.85	4.47	5.68	2.07	1.83	1.49

air leads to a 2 times increase of NMI volume fraction. Similar phenomena are also observed in the alloy at heating up to the annealing condition (360 °C, 20 min), however, NMI volume fraction is 2–2.5 times higher, compared to the metal in as-quenched condition. In the condition of tempering and ageing its value drops 1.5 to 3 times, reaching limit values of 1.7–3.1 and 1.37–2.84 %, respectively. Thus, the established regularities of variation of NMI volume fraction in V96tss alloy depending on welding heating temperature show that compared to the initial condition of the base metal the greatest amount of the phases precipitate in the HAZ section, where the conditions for annealing are in place.

Considering the nature of variation of NMI volume fraction, depending on the distance from the notch tip for the two studied welding processes (Figure 1), it may be noted that their precipitates in the metal are more non-uniform under the conditions of annealing, which occurs in the HAZ metal in TIG welding. Maximum values of NMI volume fraction (6.77 %) were observed in the structure of the studied alloy in the sample section near the notch. Their similar arrangement was found after quenching heating. Under the conditions simulating EBW, phase distribution in V96tss alloy is more uniform, and scatter is not higher than 15 %. In this case, a smaller volume fraction of NMI (4.1 %) is found in the sample near the notch. In other conditions of the metal (tempering, ageing) this index changes from 0.5 to 3.0 %. Sections with their maximum content can be the potential zones of lowering of the resistance to crack initiation and propagation under static loading. As the weld is usually located in parallel to the longitudinal direction of semi-finished product rolling, the above procedure was used in the first stage of investigation.

Redistribution of the dissolved atoms of alloying elements and impurities, which occurs in the metal under the thermal impact of welding, leads to precipitation of NMI particles both in the grain bulk and along their boundaries [7]. Nature of running of the process depends on heating temperature and cooling rate. Under the conditions of quenching, when particle dissolution runs in parallel to their precipitation, formation of a smaller NMI volume fraction (from 3 to 6 %) is noted, particularly in the case of the high cooling rate inherent to EBW. Under the conditions of annealing when NMI particles not only precipitate, but also coagulate, the metal cooling rate influences only the scatter of their volume fraction.

Comparing the obtained levels of NMI volume fraction precipitating at welding heating and cooling (Figure 2), its dependence on the cooling rate was established. High cooling rate (30–50 °C/s) of V96tss alloy accompanying EBW, leads to formation of a small volume fraction of the precipitating phases after quenching and annealing. At sample cooling in water to quenching temperature, NMI volume fraction is nonuniform and varies in the range of 1.12–2.20 % (see Table 1). Under the conditions of air cooling, its value rises 4 times (Figure 3). Here both the minimum

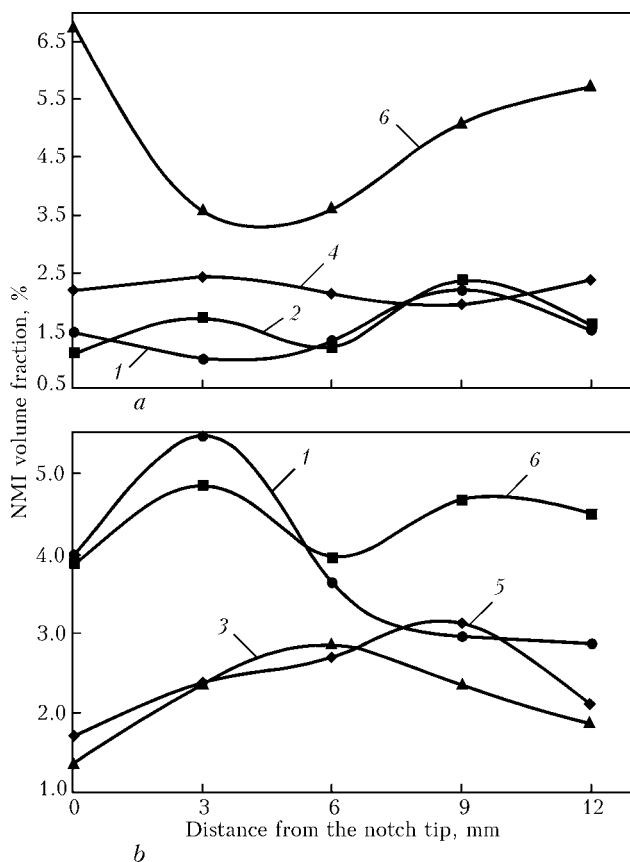


Figure 1. Change of NMI volume fraction in V96tss alloy in TIG welding (a) and EBW (b) allowing for the distance from the notch tip: 1 — overheating; 2, 3 — quenching with cooling in air and water, respectively; 4, 5 — annealing with cooling in air and water, respectively; 6 — tempering

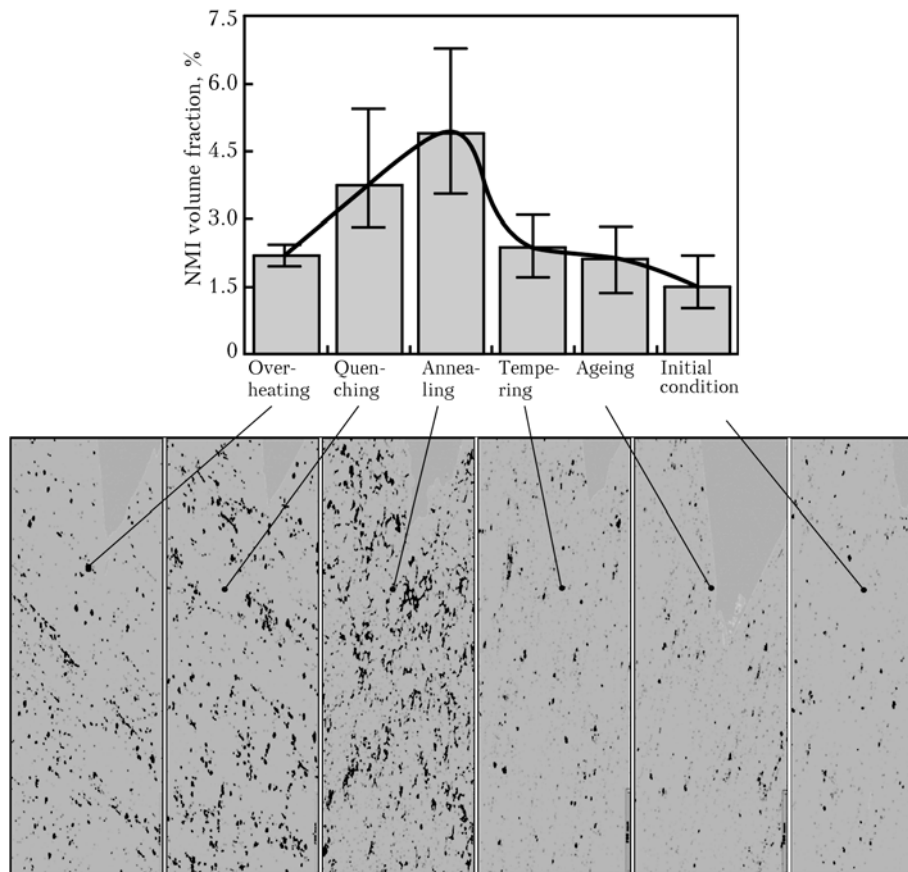


Figure 2. Influence of thermal conditions in TIG welding of alloy V96tss on NMI volume fraction and nature of their precipitation along the rolling direction

level of NMI volume fraction (2.85 %) and its maximum level (5.45 %) are increased. Heating of the samples of the studied V96tss alloy up to the annealing temperature leads to a change of the observed dependencies. Lower limits of NMI volume fraction coincide, and are equal to 4 %, and the maximum ones are determined by the cooling rate. At its increase the duration of the process of solid solution decomposition decreases, this promoting 1.5 times lowering of NMI volume fraction in the studied alloy.

As is seen from the data given in Figures 2 and 3, duration of the thermal cycle of welding affects not only the NMI volume fraction, but also the nature of particle distribution. A higher cooling rate in EBW ensures the dispersity and uniformity of particle precipitation. Nonetheless, a certain similarity in the nature of the change of the curves of NMI distribution in the HAZ metal structure should be also noted. In both the cases, the welded joint section heated up to the annealing condition, can be the potential site of lowering of the level of toughness and ductility, compared to other sections of the HAZ. The greatest volume fraction (6.77 %) of the precipitating particles is observed in the section of annealing ($T = 360\text{ }^{\circ}\text{C}$, 20 min) in TIG welding. Under the conditions simulating metal heating in EBW, the volume fraction of particles is 2 times smaller, and equal to approximately 5 %. Compared to the initial condition of the alloy (1.5 %) the obtained values of the amount of NMI are 4.5 and 2.5 times higher, respectively.

When studying the morphology of particle location, it was established that two types of precipitations are observed in the alloy as a result of welding heating. The computer procedure used in the study for determination of volume fraction of NMI contained in the samples, did not allow their identification, which is related to insufficient resolution of ImagePro program by colour contrast. Nonetheless, when studying the fractures of samples failing at off-center tension, also two types of NMI were found. NMI of a regular geometrical shape and complex structure can be regarded as the first type (Figure 4). They are non-uniformly located in the structure. Inclusion size is equal to 10–20 μm . At the first stage of plastic deformation under the conditions of off-center tension they delaminate, thus forming microcracks. Subsequent deformation of the metal leads to the crack growing and results in its coming to the boundary between the grains. Having studied the composition of individual delaminations of the particles, it was established that they contain 24–27 % Zr and 15–17 % Sc, respectively. Their microhardness is much higher than that of the matrix, where zirconium and scandium content is equal to just 0.2 and 0.5 %, respectively. Particles having a more round shape and an order of magnitude smaller dimensions, can be considered as the second type of phase inclusions (Figure 5). Content of the main alloying elements in them is as follows, %: 26–28 Cu, 38–40 Zn, 11–14 Mg. Average length of such particles is equal to 3–5 μm , their width being 2–

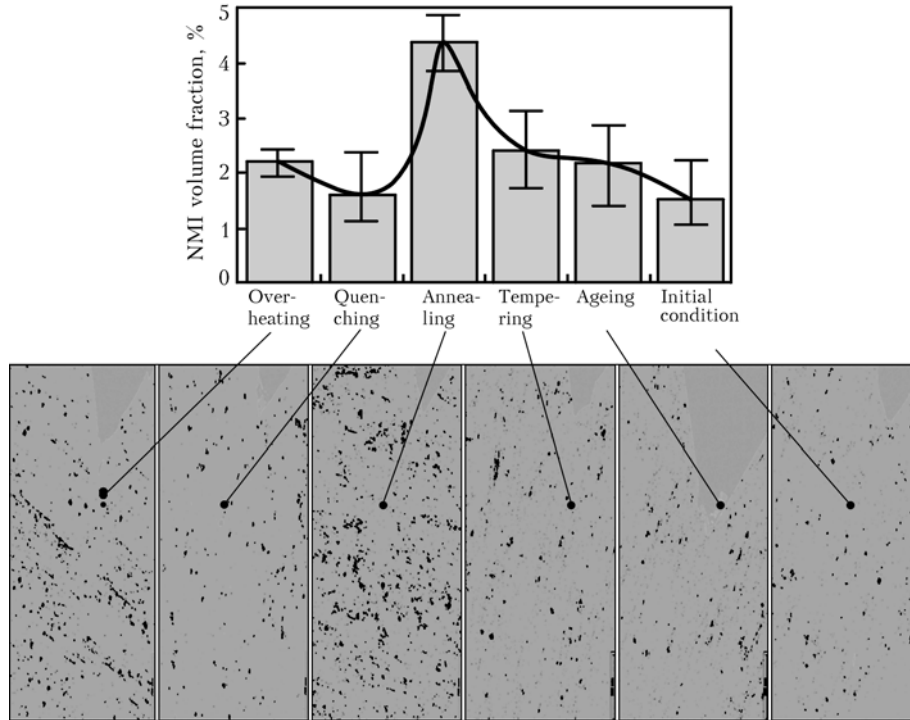


Figure 3. Influence of thermal conditions in EBW of V96tss alloy on NMI volume fraction and nature of their precipitation along the rolling direction

3 μ m. They are located in the form of clusters predominantly along the boundaries of grains oriented in the rolling direction.

In order to understand the features of particle precipitation in the HAZ metal under the impact of welding heating, samples cut out across the rolling direction were additionally studied at the second stage. According to the obtained results, the nature of distribution of the particles precipitating in the metal during heating, depends on sample orientation relative to the rolling direction (longitudinal or transverse direction). In EBW the greatest quantity of precipitates is observed in the sample, which in the overheated condition simulates the zone of weld fusion with the base metal (Figure 6). Then the curve of variation of NMI volume fraction abruptly decreases to 1.3 %, which is due to formation of complex compounds containing zirconium and scandium additives

at the temperature of heating below 500 °C. In the other studied sections of the HAZ, the NMI volume fraction decreases monotonically, which is related to the duration of the thermal cycle of welding (heating and cooling).

Under the conditions of TIG welding, two maximums of regularities variation are observed in the studied samples at particle precipitation. The first is the overheated condition, the second is that of annealing. Presence of the second maximum, which is by 2.17 % lower than the first one, is attributable to heterogeneous initiation and growth of excess phase particles under the annealing conditions. Considering the microstructure of precipitates at annealing, the result of their coagulation compared to the condition of overheating and quenching is clearly visible, which, possibly, promotes increase of the phase volume fraction. Compared to EBW conditions, in TIG welding

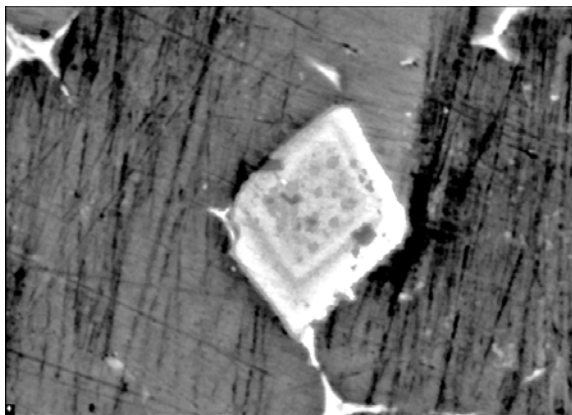


Figure 4. NMI in V96tss alloy enriched in zirconium and scandium ($\times 3000$)

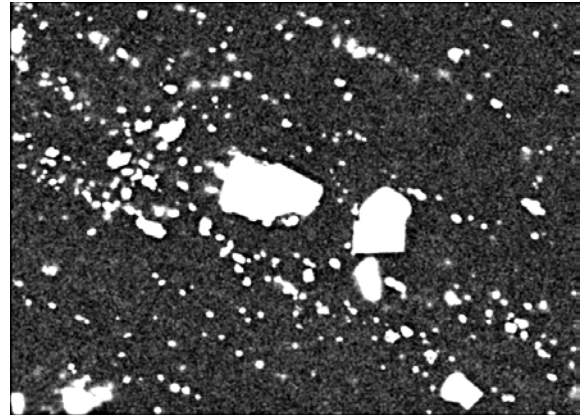


Figure 5. NMI in V96tss alloy enriched in copper, zinc and magnesium ($\times 1000$)



conditions for embrittlement of the intergranular gap are in place, this influencing crack initiation in this section of the welded joint.

Comparing the nature of distribution of particles precipitating in the near-weld zone at heating, differences in their shape and dimensions were found. In the longitudinal direction they are elongated along the rolling direction, in the cross-section they have a more round shape, are non-uniform and have a complex composition. According to the data, obtained by the colour contrast method, which reproduces the difference between the phases in terms of composition, five types of NMI can be singled out. Their size after heating in the TIG welding mode is between 2.5 and 7.8 μm , being 1.5–2 times larger than when EBW is used (1.7–4.9 μm). Five types of inclusions are observed in the base metal, as well as in the HAZ section, where ageing occurs. Three or four types of NMI are found in the other heat-affected sections. Such differences in the varieties of particles precipitating at heating are due to the temperature-time parameters of the thermophysical conditions of welding.

As is seen from Figure 7, microhardness of inclusions, containing zirconium and scandium, is 1.5 times higher than that of the matrix, which can be an indication of their higher brittleness. At testing under the conditions of tension, these particles are exactly the sites of microcrack initiation. The dependence is established between the level of microhardness of the matrix and the studied particles, depending on the structural condition, inherent to individual sections of the HAZ metal. The smallest values of microhardness of V96tss alloy matrix are observed in the overheated condition, which simulates the line of fusion of the weld with the base metal.

The second zone of microhardness lowering is the joint section, where the alloy was in the tempering condition during welding ($T = 360\text{ }^\circ\text{C}$, 3 min). This

Table 2. Fracture toughness characteristics of joints of V96tss alloy in different sections of the HAZ depending on the conditions of welding heating

Heating conditions	σ_{fr} , MPa	K_{IC} , MPa $\sqrt{\text{m}}$	J_C , J/cm 2	SWCP, J/cm 2
Overheating (FZ) 550 °N, 3 s	389	46.81	4.8	10.0
Quenching 460 °N, 1 h	456 / 397	32.02 / 24.19	3.5 / 1.9	4.8 / 6.6
Annealing 360 °N, 20 min	389 / 152	46.81 / 18.10	3.8 / 1.1	10.0 / 3.4
Tempering 360 °N, 3 min	371	32.02	3.24	6.6
Ageing 140 °N, 7 h	211	17.69	1.1	3.3
Base metal	245	17.23	1.1	3.2

Note. The numerator gives the results of testing after heating and cooling in water simulating EBW conditions, the denominator ---- TIG welding conditions.

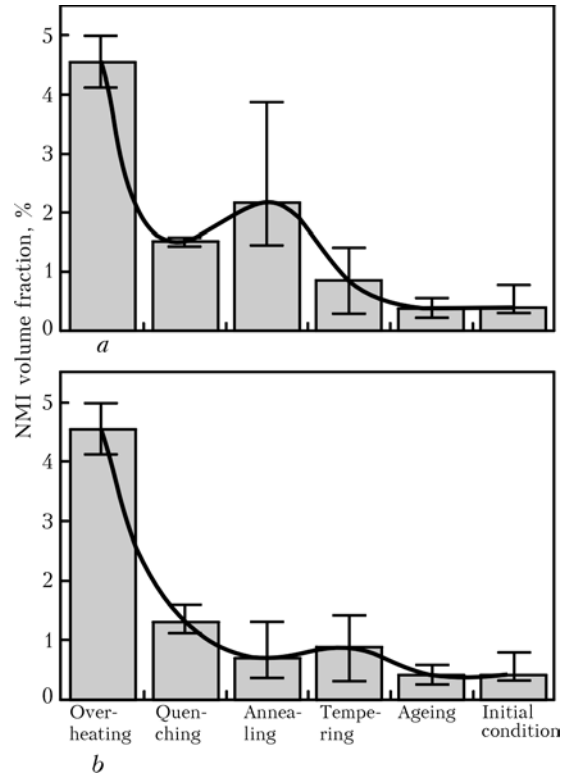


Figure 6. Influence of thermal conditions in TIG welding (a) and EBW (b) of V96tss alloy on volume fraction of phases and features of their precipitation across the rolling direction

is, obviously, promoted by the specific nature of phase transformations in view of the short duration of the action of welding cycle temperature on the metal. The found zones of abrupt lowering of the level of strength

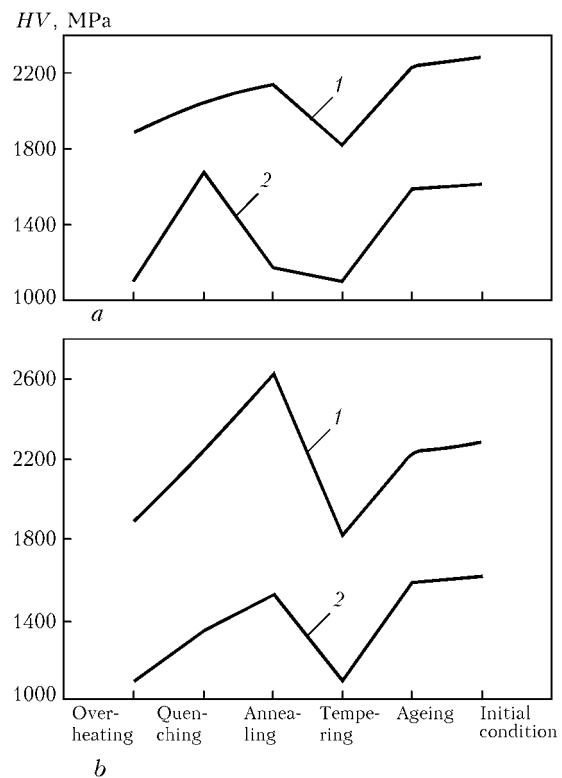


Figure 7. Nature of variation of microhardness of particles enriched in zirconium and scandium (1) and matrix (2) depending on temperature conditions of the HAZ in TIG welding (a) and EBW (b)



of V96tss alloy due to heating are the potential sections of limitation of the metal resistance to the action of external load, which may lead to crack initiation in service. According to the data on fracture toughness indices, given in Table 2, they decrease with increase of particle volume fraction at welding heating. Limiting the ability of V96tss alloy to deform plastically, the coarse inclusions located along the grain boundaries, facilitate crack initiation and propagation, which is indicated by an abrupt lowering of the level of fracture toughness indices.

As is seen from Table 2, practically all the fracture toughness indices depend on the thermophysical conditions of heating and cooling. The cooling rate in welding has the strongest influence on the energy of crack initiation J_C , which decreases by 15 % at cooling in water and by more than 2–3 times at cooling in air. The specific work of crack propagation (SWCP) also decreases.

Such regularity is observed also for the critical factor of stress intensity K_C , particularly after heating to the annealing temperature. K_C value in this case decreases more than 3 times. Structural changes occurring at artificial ageing of V96tss alloy, ensure an increase of σ_{fr} values by 20 %. However, other fracture toughness indices (K_C , J_C , SWCP) are characterized by lower values — 17.69 MPa \sqrt{m} , 1.1 and 3.1 J/cm², respectively.

Thus, change of the level of crack initiation and propagation indices at fracture of V96tss alloy in the near-weld zone depends on the thermophysical conditions accompanying the welding process. Increase of

the volume fraction of particles, structural and phase changes resulting from the thermal cycle of welding, cause a nonuniform stressed state in the alloy and the associated mechanism of joint fracture, which is indicative of the determinant role of the volume fraction of particles, also with modifiers (zirconium or scandium) on the nature of crack initiation at fracture of V96tss alloy and its welded joints.

1. Fridlyander, I.N. (2002) Aluminium alloys in aircraft during the periods of 1970–2000 and 2001–2015. *Tekhnologiya Lyog. Splavov*, **4**, 12–17.
2. Fridlyander, I.N., Beletsky, V.M., Krivov, G.A. (2000) Aluminium alloys in aircraft structures. *Tekhnolog. Systemy*, **1**, 5–17.
3. Mondolfo, L.F. (1979) *Structure and properties of aluminium alloys*. Moscow: Metallurgiya.
4. Ishchenko, A.Ya., Labur, T.M. (1999) *Weldable aluminium alloys containing scandium*. Kiev: MIIVTs.
5. Rabkin, D.M. (1986) *Metallurgy of fusion welding of aluminium and its alloys*. Kiev: Naukova Dumka.
6. Fujiwara, T. (2001) Technologies of joining of light metals in aircraft and space engineering. *Keikinzoiku Yosetsu*, **39**(3), 1–11.
7. Ishchenko, A.Ya., Sklabinskaya, I.E. (1979) Specifics of transformations in heat-affected zone during welding of some high-strength aluminium alloys. *Avtomatich. Svarka*, **5**, 26–29.
8. Broek, D. (1980) *Principles of fracture mechanics*. Moscow: Vysshaya Shkola.
9. Vladimirov, V.I. (1984) *Physical nature of fracture of metals*. Moscow: Metallurgiya.
10. Botvina, L.P. (1989) *Kinetics of fracture of structural materials*. Moscow: Nauka.
11. Kishkina, S.I. (1981) *Fracture resistance of aluminium alloys*. Moscow: Metallurgiya.
12. Labur, T.M., Taranova, T.G., Kostin, V.A. et al. (2006) Influence of structural transformations in welding of aluminium alloy V96 on fracture resistance parameters. *The Paton Welding J.*, **11**, 17–21.

EXPRESS-METHOD TO DETECT REGIONS OF PLASTICALLY DEFORMED METAL IN STRUCTURES

The method was developed at the E.O. Paton Electric Welding Institute together with SPC «Special R&D» (Kharkov, phone/fax: (0572) 64 36 13, 64 99 85) to widen the technical capabilities at expert evaluation of the condition of pressurized structures.

The method is based on the ability of the metal to change the magnetic parameters, depending on the indices of physico-mechanical condition (composition, mechanical properties, heat treatment, structure, stress-strain state, etc.). The method consists in measurement of the coercive force as a magnetic parameter, which is the most sensitive to changes occurring in the metal.

In order to detect plastically deformed metal in a pressurized structure, it is necessary to take two measurements of the coercive force, namely under load and after load relieving. It is preferable to conduct measurements at a trial pressure in keeping with DNAOP 0.00-1.07–94 Rules. The established higher value of the coercive force compared to its value under load indicates that the metal of the studied region was plastically deformed. The method was verified on cylinders and pipes of steels 10, 30KhGSA and 17G1S. Measurements were taken using KRM-TsK-2M instrument.

Purpose and application. The method is designed for diagnostics of the condition of ferromagnetic metal structures and should find application in technical inspection of cylinders, diagnostics of the condition of apparatuses of chemical and petrochemical productions, in pipeline transportation and on other facilities.

Contacts: Prof. Garf E.F.
E-mail: yupeter@ukr.net

INVESTIGATION OF PERFORMANCE OF WELDED JOINTS IN STEAM GENERATORS PGV-1000M BY LEAK TESTS

V.I. MAKHNENKO¹, O.V. MAKHNENKO¹ and O.Ya. ZINCHENKO²

¹E.O. Paton Electric Welding Institute, NASU, Kiev, Ukraine

²National Atomic Power Generation Company «Energoatom», Kiev, Ukraine

Increase in excessive pressure in the case of using the air-hydraulic aquarium method for testing leak-tightness of steam generators PGV-1000M leads to increase in gap between a heat exchanger pipe and collector wall. As a result, extra stresses are formed at the gap tip (weld root), which may lead to violation of integrity by the mechanism of initiation of a crack-like design defect. The risk of initiation of fracture with growth of excessive pressure is estimated.

Keywords: heat-exchanger pipes, welded joints, residual stresses, calculation, risk of fracture, performance of joints

Air-hydraulic aquarium test of leak-tightness of steam generators PGV-1000M is now the most effective method for detecting leaks in heat exchanger pipes (HEP) and welded joints between their ends and collector [1]. This method of testing leak-tightness in the second loop of PGV-1000M (Figure 1) leads to formation of excessive air pressure in the steam generator casing, provided that the collector is filled to a certain level with water (first loop).

If pipes or welded joints have defects in the form of leaks (Figure 2), air bubbles are evolved into water of the first loop in a region of corresponding pipes of a hot or cold collector, which is fixed by corresponding inspection devices. Leakage Q of a heat carrier (feed water) in the region of a pipe at excessive pressure $P = 10$ MPa between the first and second loops (Figure 3), the permissible value of which is $Q = 2$ l/h,

is determined by leak tests on the basis of the frequency of evolution of air bubbles in the region of this pipe, depending upon the excessive air pressure.

It can be seen from Figure 3 that increase in pressure substantially reduces the test time by reducing time τ between formation of adjacent bubbles. For example, at $Q = 2$ l/h, τ is reduced from 500 (at $P = 0.1$ MPa) to 7 s (at $P = 2.0$ MPa). Given that approximately 11,000 pipes in each loop of PGV-1000M are subject to tests, the above is of a high importance.

Increase in excessive pressure on the side of the second loop in the steam generator leads to increase in gap (see Figure 2) between HEP and collector wall. This induces extra stresses at the tip of this gap (weld root), which under certain conditions (residual stresses in the weld, embrittlement of the weld metal, insufficient penetration depth or bridge thickness) may lead to violation of integrity by the mechanism of initiation of a crack-like design defect.

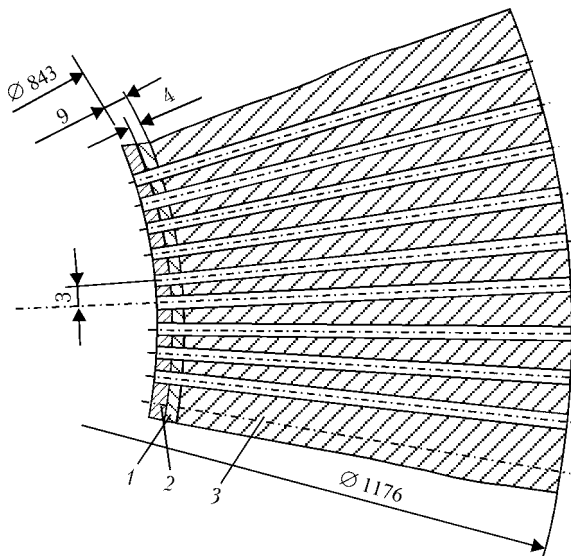


Figure 1. Schematic of assembly of HEPs in casing of collector of PGV-1000M: 1 — first deposited layer of steel 07Kh25N10; 2 — second deposited layer of steel 04Kh20N10; 3 — base metal — steel 10GN2MFA

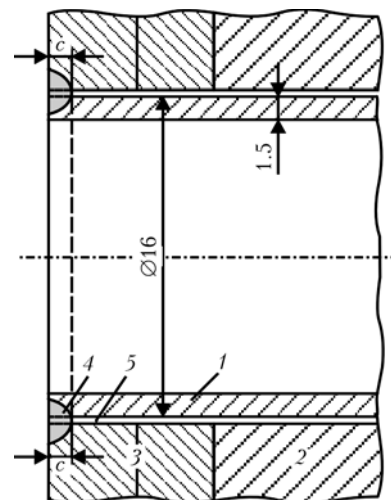


Figure 2. Schematic of welded joints between HEP and collector: 1 — HEP; 2 — collector wall; 3 — austenitic deposited metal; 4 — weld; 5 — gap between HEP and collector

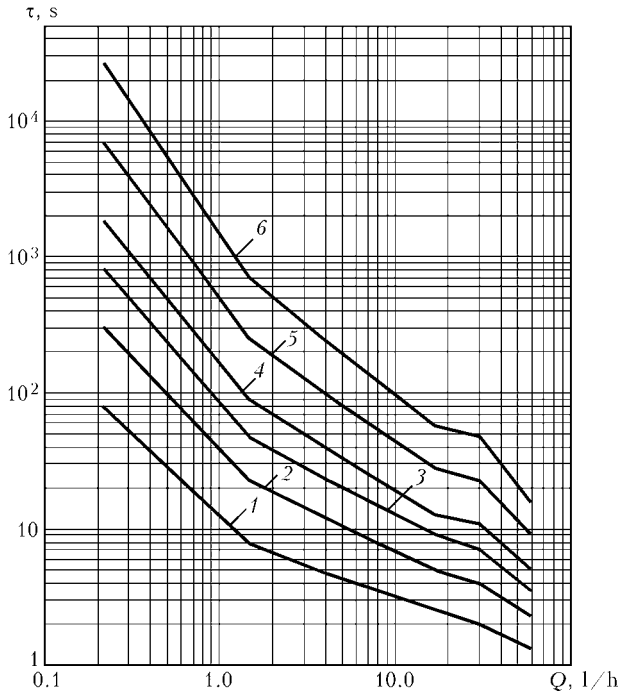


Figure 3. Time τ of holding of steam generator in tests under excessive air pressure P (0.1–2.0 MPa) against heat carrier leakage Q : 1 — 2.0; 2 — 1.0; 3 — 0.6; 4 — 0.4; 5 — 0.2; 6 — 0.1 MPa

This study is dedicated to estimation of the risk of such initiation with increase in excessive pressure P .

Problem statement. It can be assumed with certain conservatism from the schematic shown in Figure 2 that the gap is a circumferential crack with uniform excessive pressure P and a circular bridge with thickness c formed therein, where non-relaxed residual stresses σ_{rr}^{res} are effective, leading to violation of integrity at $\sigma_{rr}^{res} > 0$.

Criterion of brittle-tough fracture [2] (procedure R6) is used to quantitatively estimate the risk of violation of integrity depending upon P and non-relaxed residual welding stresses σ_{rr}^{res} . Applicability of this criterion to materials of welded joints in austenitic steels is shown in Figure 4 [2], where curve D corresponds to experimental data obtained for austenitic

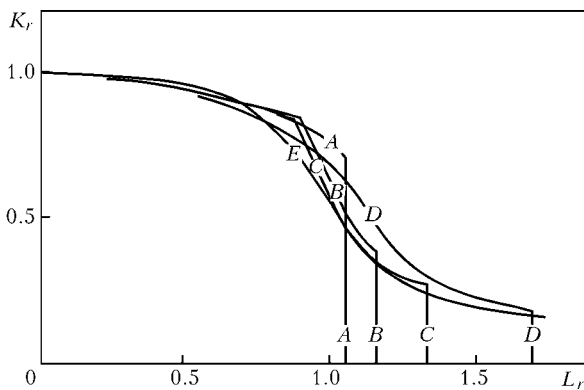


Figure 4. Limiting state diagrams $K_r = f(L_r)$ for different types of structural steels [2]: A — high-strength steel EN408; B — pressure vessel steel A533B; C — low-carbon manganese-containing steel; D — austenitic steel; E — generalised curve according to [2]

steels, and curve E presents generalised relationship $K_r = f(L_r)$:

$$K_r = (1 - 0.14L_r^2) [0.3 + 0.75 \exp(-0.65L_r^6)]$$

$$\text{at } L_r < L_r^{\max} = \frac{\sigma_y + \sigma_t}{2\sigma_y}; \quad (1)$$

$$K_r(L_r) = 0 \text{ at } L_r > L_r^{\max},$$

where $K_r = K_I / K_{Ic}$; $L_r = \sigma_{ref} / \sigma_y$; K_I is the stress intensity factor for the normal tear crack under consideration, which determines the risk of a purely brittle fracture, when compared with its critical value K_{Ic} for a given material; σ_{ref} is the stress caused by pressure P in the gap and capable of causing plastic instability in a bridge with thickness c , which determines its purely tough fracture depending upon P ; σ_y is the yield stress of the bridge material; and σ_t is its tensile strength.

To determine K_I in the bridge (weld) with thickness c , we will use the model of a semi-bound crack in an elastic sub-space [3], where the bridge is affected by bending moment M and force F :

$$K_I = 3.975 \frac{M}{c\sqrt{c}} + 7.044 \left(\frac{z_F}{c} - 0.368 \right) \frac{F}{\sqrt{\pi c}}, \quad (2)$$

where z_F is the distance from the bridge end to the line of action of force F . The values of M and F can be described as follows:

$$M = M_P + M_{res}; \quad F = F_P + F_{res}. \quad (3)$$

Here subscript P designates the load due to excessive pressure in a cavity between the pipe wall and collector wall, and subscript «res» — that due to non-relaxed residual stresses.

The values of M_P and F_P can be defined as reactions at the fixed end of a long cylindrical shell with diameter $2R$ and wall thickness h , caused by external excessive pressure P [4].

In this case, according to [4], it holds at $z/c = 1$:

$$F_P = \frac{(1 - \nu)P}{2\sqrt{3(1 - \nu^2)}} \sqrt{Rh}; \quad M_P = \frac{(2 - \nu)P}{4\sqrt{3(1 - \nu^2)}} Rh \quad (4)$$

or at Poisson's ratio $\nu = 0.3$:

$$F_P = 0.52P \sqrt{Rh}; \quad M_P = 0.26PRh. \quad (5)$$

The following relationship can be used for σ_{ref} :

$$\sigma_{ref} = \frac{F_P}{c} + \frac{4 \left(M_P + F_P \frac{c}{2} \right)}{c^2} = \frac{0.52P}{c} \left(3\sqrt{Rh} + \frac{2Rh}{c} \right) \quad (6)$$

Residual stresses are not taken into account in determination of the values of σ_{ref} , as in tough fracture they have enough time for full relaxation.

Bridge thickness c should be 1.5–1.0 mm according to specifications for welding of HEP for the case under consideration. However, after a certain period in service, it may decrease due to corrosion of the material.



There are at least two types of the mechanisms of corrosion decrease in bridge thickness c (Figure 5).

The first type of damages occurs due to corrosion-erosion fracture on the side of the first loop, or due to the mechanism of propagation of transcrystalline (intercrystalline) corrosion cracks on the side of the second loop. Objective conditions for initiation of the first type of damages are created over the entire length of the pipes, including at their ends, especially in horizontal steam generators [5].

The second type of damages takes place if the values of K_I according to (2) are much higher than zero, allowing for the fact that under service conditions the pressure gradient between the second and first loops is $\Delta P < 0$ (approximately -10 MPa), while this is possible only at a certain value of non-relaxed residual stresses.

Therefore, allowance for the values of residual stresses within the welded joint zone in welding of pipes is very important for solving this problem.

Evaluation of residual stresses. Small size of the zone of welding HEP to the collector wall (see Figure 2) makes it difficult to estimate the values of residual stresses by experimental methods. Publications on this issue are very scanty [6, etc.]. Worthy of notice among the official industry documents is the report [7] on experimental estimation of residual stresses in the HEP wall, induced by welding and expanding of the HEP ends. Figure 6 shows the corresponding results from study [7], the reliability of which for the above reason is rather low.

The E.O. Paton Electric Welding Institute developed in 2000 by a request of Infacor GmbH the calculation procedure for evaluation of the stressed state of welded joints formed in welding of HEP to pipe plates. The procedure is based on mathematical modelling of the kinetics of thermomechanical processes occurring in the zone of pipe to pipe plate welding, and is adapted to different materials of HEPs and pipe plates, shape of welded joints, etc. [6]. This procedure was used in the present study to estimate residual stresses in the case considered in Figure 2.

Figure 7 shows the distribution of residual stresses σ_{rr}^{res} in the welded joint zone at different values of welding heat input q_w providing penetration depth c ranging from 0.45 to 1.50 mm. The distribution of residual stresses after welding under the above conditions is of a very complex nature, as the presence of free surfaces (internal surfaces of pipes, gap between a pipe and collector, end surfaces) exerts a marked effect on the distribution of residual stresses. In section $z = \text{const}$ (i.e. in planes located at different distances from the end), the distribution of σ_{rr}^{res} along coordinate r has two extreme zones --- one zone at $r = 8$ mm (pipe surface), and second zone at $r = 12$ – 13 mm (approximately at the centre of the distance between the neighbouring pipes).

The stressed state dramatically decreases with increase in z , and at $z = 4$ – 5 mm the level of residual stresses in the collector wall is insignificant.

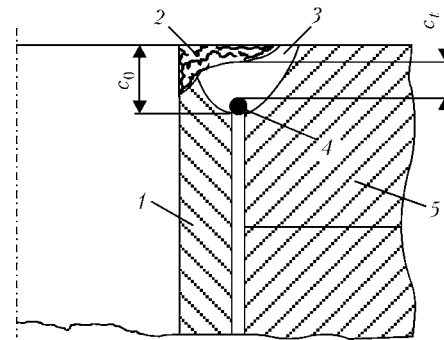


Figure 5. Schematic of decrease in bridge thickness during operation from c_0 to c_t : 1 --- HEP; 2 --- zone of corrosion-erosion fracture; 3 --- weld; 4 --- zone of intercrystalline stress cracking; 5 --- collector wall

Figure 8 shows the distribution of residual stresses σ_{rr}^{res} in section $z = \text{const}$ in the walls of a pipe and collector (pipe plate) depending upon coordinate r (calculation data) at $c = 1.05$ mm. The Figure also shows the data of study [7]. The comparison shows that the experimental data are close to the calculation ones for the middle part of the pipe wall at $z/c \approx 0.5$

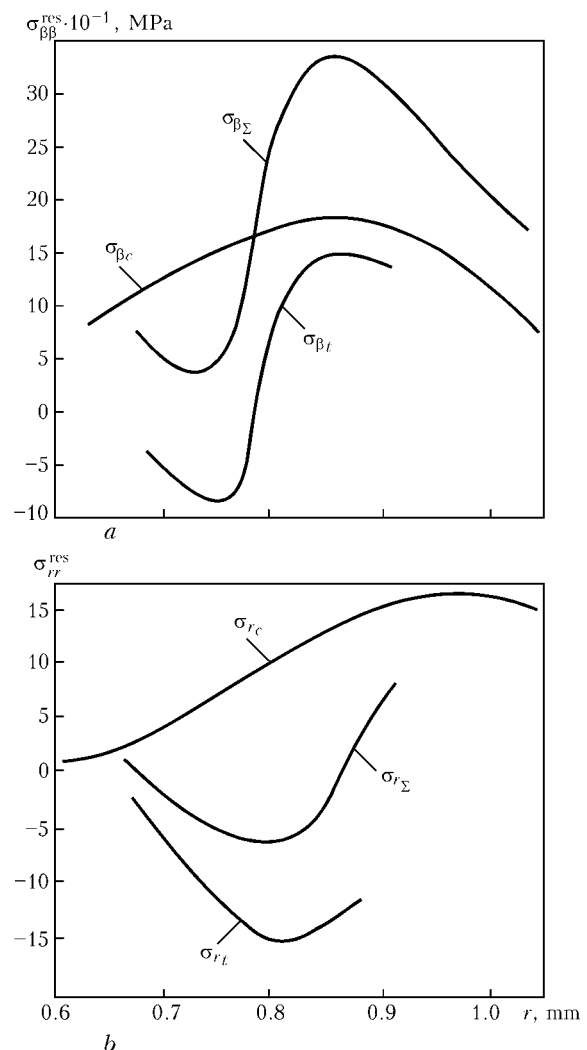


Figure 6. Experimental data [7] on measuring residual tangential (circumferential) $\sigma_{\beta\beta}^{\text{res}}$ (a) and radial σ_{rr}^{res} (b) stresses in HEP wall formed in welding and expansion of pipe ends: subscript c means after welding, b --- after expansion, Σ --- total; r --- coordinate r

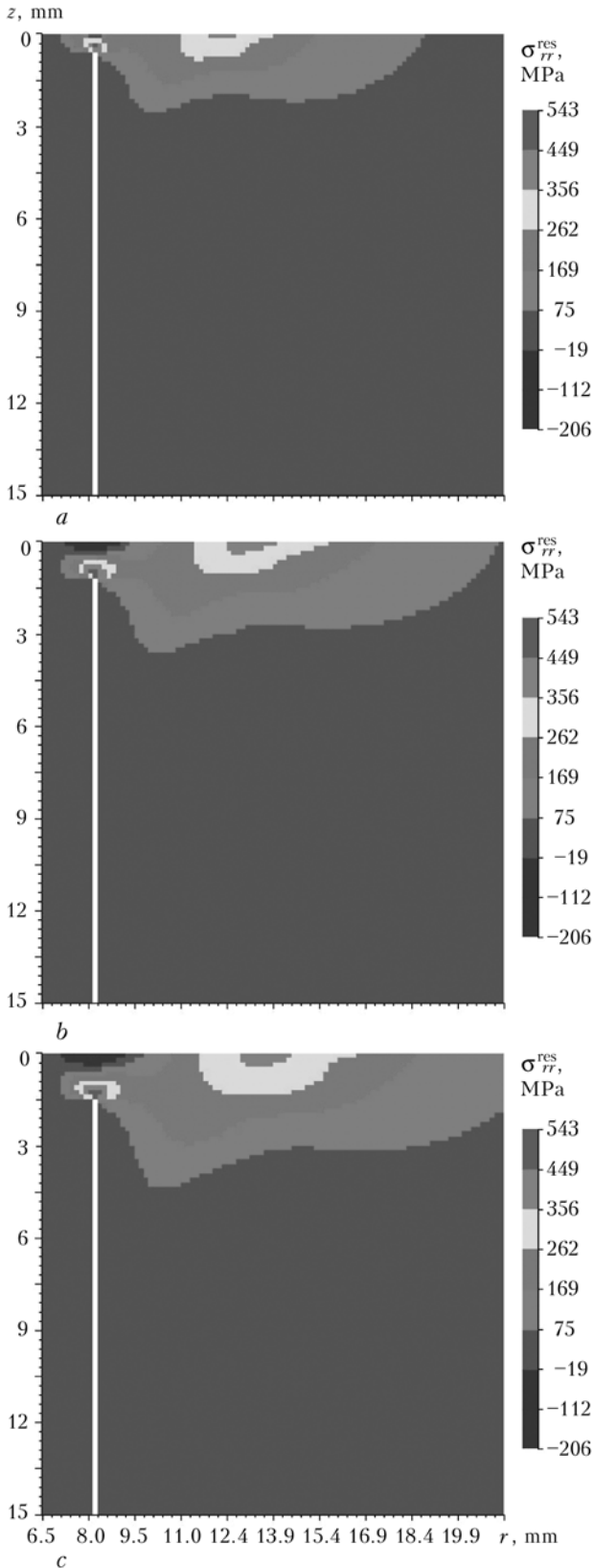


Figure 7. Calculated distribution of residual radial stresses σ_{rr}^{res} in welded joint at different heat input, providing penetration depth $c = 0.45$ (a), 1.05 (b) and 1.50 (c) mm

and $7 < r < 8$ mm. As follows from Figure 7, welding conditions do affect residual stresses in the weld.

Compared with Figure 7, Figure 9 shows in more detail the data obtained at $r = 8$ mm (HEP diameter 16 mm) and under different welding conditions. These

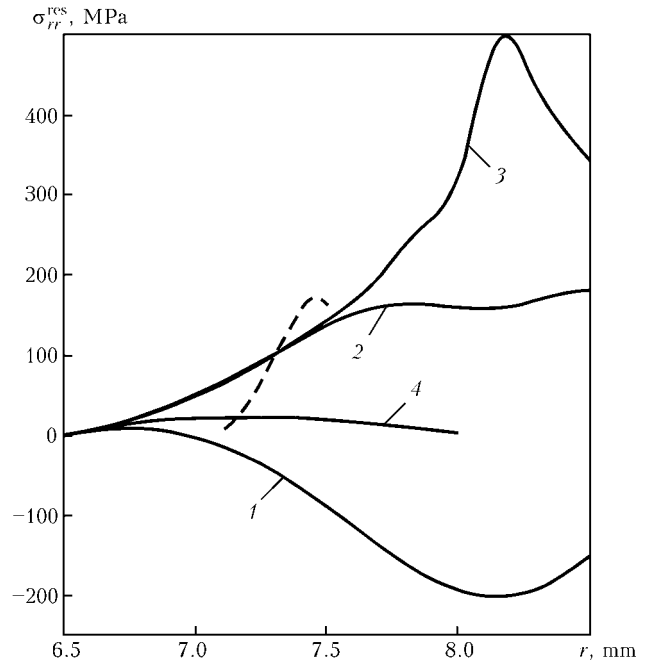


Figure 8. Distribution of residual stresses σ_{rr}^{res} through thickness of the pipe wall ($6.5 \leq r \leq 8.0$ mm) and pipe plate ($r > 8$ mm) under welding conditions providing bridge thickness $c = 1.05$ mm: solid curves — calculation results for section $z = \text{const}$ (i.e. in planes at different distances from the pipe end); dashed curve — experimental data [7]: 1 — $z/c = 0$; 2 — 0.5; 3 — 1.0; 4 — 1.5

data were approximated through linear distribution within $0 < z < c$ (dashed curve in Figure 8), M_{res} and F_{res} being calculated for $z_F/c = 0.5$ (Table 1). It can be seen from Table 1 that growth of c from 0.45 to 1.50 mm leads to growth of K_I^{res} according to (2) from 224 to 409 $\text{MPa}\cdot\text{mm}^{1/2}$.

Table 2 gives loading characteristics calculated from (2) and (6) at different excessive pressure P . The data obtained are indicative of the fact that the contribution of residual welding stresses grows in a sum of $K_I^P + K_I^{res}$ with growth of c and decrease of P . At $P < 4$ MPa, the contribution of residual stresses in the above sum is more than 66 % at $c = 0.45$ mm, 85 % at $c = 1.05$ mm, and 91 % at $c = 1.5$ mm.

Properties of material determining integrity of a welded joint. To generate data on maintenance of integrity of a welded joint from relationship (1), it is necessary to have information on calculated resistance of the weld metal to brittle fracture, K_{Ic} , and its plastic instability (σ_y, σ_v). As welding is performed using a non-consumable electrode, the weld metal acquires properties that are in-between the pipe material and material of the upper deposited layer in the collector at a test temperature of 15–30 °C.

Table 1. Results of processing the data shown in Figure 8

Welding mode	q_w , J/mm	\bar{n} , mm	F_{res} , MPa·mm	\dot{I}_{res} , MPa·mm ²	K_I^{res} , MPa·mm ^{1/2}	z_F/c
1	65	0.45	129	9.4	224	0.5
2	100	1.05	191	65.1	338	0.5
3	130	1.50	268	144.7	409	0.5



Table 2. Characteristics of loading of welded joints due to excessive pressure P and residual stresses σ_{rr}^{res}

c , mm	\bar{D} , MPa	σ_{ref} , MPa	K_I^P , MPa·mm ^{1/2}	$K_I = K_I^P + K_I^{res}$, MPa·mm ^{1/2}	L_r	K_r
0.45	0.2	15.20	9.60	233.6	0.087	0.228
	1.0	75.60	47.83	271.8	0.430	0.265
	2.0	151.20	95.70	319.7	0.860	0.312
	3.0	226.80	143.50	367.5	1.296	0.358
	4.0	302.40	191.40	415.4	1.730	0.405
1.05	0.2	3.30	3.20	337.2	0.029	0.341
	1.0	16.50	15.94	349.9	0.094	0.341
	2.0	33.00	31.90	365.9	0.188	0.357
	4.0	66.00	63.80	397.8	0.377	0.388
	10.0	165.00	159.40	493.4	0.940	0.481
	15.0	247.50	239.10	573.1	1.410	0.559
1.50	0.2	1.83	2.10	411.1	0.010	0.401
	1.0	9.15	10.44	419.4	0.052	0.409
	2.0	18.30	20.90	429.9	0.104	0.419
	4.0	36.60	41.80	450.8	0.203	0.440
	10.0	91.50	104.40	513.4	0.523	0.500
	15.0	137.20	156.60	565.6	0.784	0.552
	20.0	183.00	208.80	617.8	1.045	0.603
	25.0	228.70	261.00	670.0	1.300	0.653

The values of σ_t for the HEP and deposited layer materials are 640–700 MPa [5], and the values of σ_y depend upon the strain hardening (cold working) and, according to the calculation data for the weld metal, are close to $\sigma_y = 350$ –380 MPa. Assume $\sigma_t^r = 640$ MPa and $\sigma_y^r = 350$ MPa to be the rated values. Accordingly, the calculated values of σ_y and σ_t should decrease n times (here n is the safety factor). For the hydraulic

tests according to [8], it is assumed that $n = 2$, i.e. the calculated values are $\sigma_t = 320$ MPa and $\sigma_y = 175$ MPa.

Critical values of the J -integral for steel of the 08Kh18N10T type can be used for K_{Ic} . Corresponding tests were conducted more than once. In particular, study [9] gives an experimental value of $K_c = 65 \text{ MPa}\cdot\text{m}^{1/2} = 2050 \text{ MPa}\cdot\text{mm}^{1/2}$, which is a rather conservative estimate. If we take this value as a rated one, the calculated value will be $K_c = 2050/n = 1025 \text{ MPa}\cdot\text{mm}^{1/2}$.

Permissible values of excessive air test pressure. Allowing for the above-said, i.e. at $n = 2$, the following calculated data were obtained:

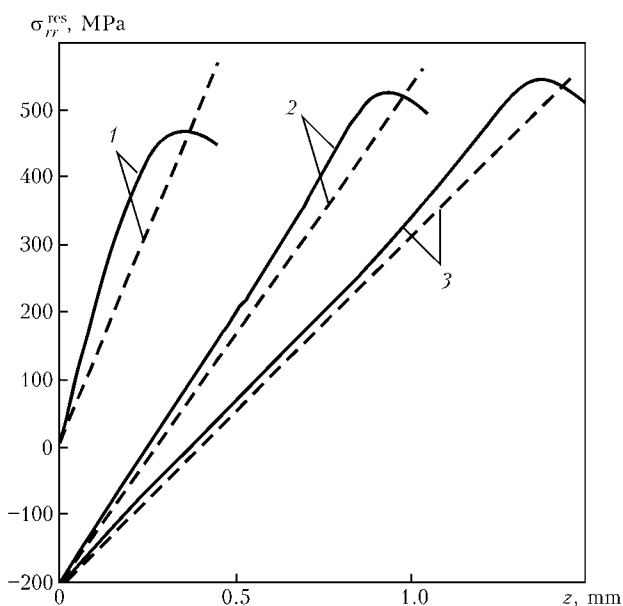


Figure 9. Distribution of residual stresses σ_{rr}^{res} through thickness of the bridge across its section ($r = 8$ mm) under welding conditions providing $c = 0.45$ (a), 1.05 (2) and 1.50 (3) mm: solid curves — results of elasto-plastic analysis; dashed curves — approximations

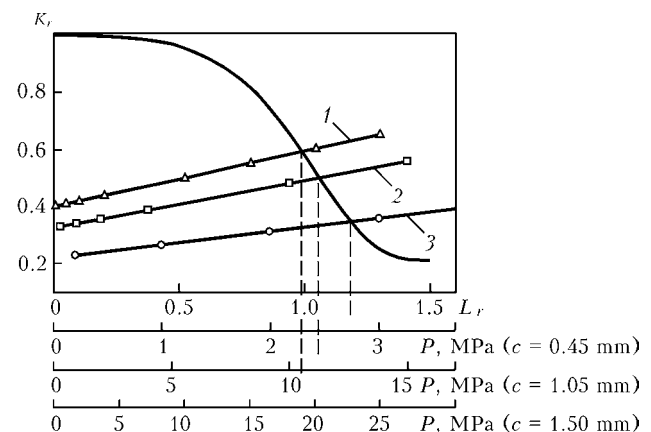


Figure 10. Diagram plotted by superposition of the curve of limiting state $K_r = f(L_r)$, according to (1), on calculated points $K_r(P)$ and $L_r(P)$: 1 — $c = 0.45$ mm, $P_{cr} = 2.7$ MPa; 2 — $c = 1.05$ mm, $P_{cr} = 11.2$ MPa; 3 — $c = 1.50$ mm, $P_{cr} = 19.0$ MPa



$dl/dt, \text{ mm/h}$

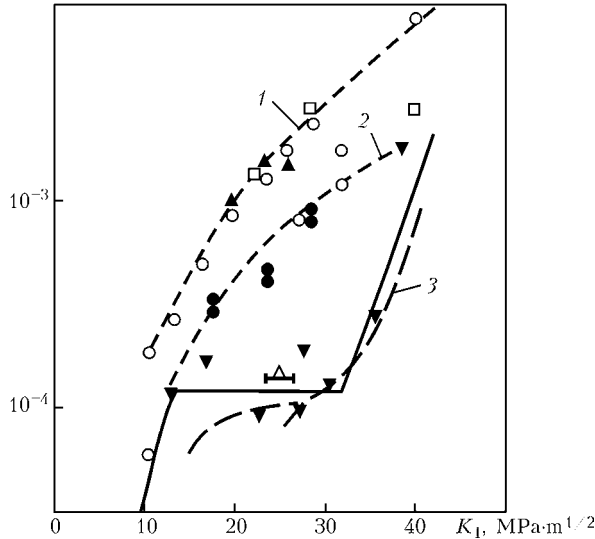


Figure 11. Kinetics of growth of stress intercrystalline corrosion crack under long-time static loading in chrome-nickel steels with upper (1), medium (2) and insignificant (3) sensitisation: \blacktriangledown — sensitisation at 650 °C for 2 h, $O_2 \approx 0.2 \text{ mg/l}$; \blacktriangle — same, different melt; \bullet — different sensitisation at $O_2 \approx 0.2 \text{ mg/l}$; \circ — sensitisation at 650 °C for 24 h, $O_2 \approx 8 \text{ mg/l}$; \square — same, but at $O_2 \approx 0.2 \text{ mg/l}$

$$\sigma_y = \sigma_y^r/n = 175 \text{ MPa}; \quad \sigma_t = \sigma_t^r/n = 320 \text{ MPa};$$

$$K_c = K_c^r/n = 1025 \text{ MPa}\cdot\text{mm}^{1/2}; \quad L_r^{\text{max}} = \frac{\sigma_y + \sigma_t}{2\sigma_y} = 1.41;$$

by using relationships (1) and data of Table 2, we determine coordinates K_r and L_r (Figure 10) for different values of excessive pressure P . The values of these coordinates for a fixed value of c are proportional to P , i.e. these points are connected by straight line. Intersection of these curves with a curve plotted according to (1) determines critical excessive test pressure P_{cr} . As a result, we obtain:

$c, \text{ mm}$	0.45	1.05	1.50
$P_{cr}, \text{ MPa}$	2.70	11.2	19.0

As follows from the above data, at $c > 0.5 \text{ mm}$ the excessive test pressure (up to 2.7 MPa) provides maintenance of integrity of welded joints between the pipes and collector.

Unfortunately, the values of c are difficult to control by non-destructive test methods. In welding, the initial value of c is usually not lower than 1.0 mm. However, it may decrease in long-time operation due to corrosion. This occurs most intensively at very high values of $K_I = K_I^P + K_I^{\text{res}}$, where K_I^{res} is K_I at a working pressure of about -10 MPa. For the initial values of

c and K_I^{res} (see Table 1) at $P = -10 \text{ MPa}$, we have the following:

$c, \text{ mm}$	0.45	1.05	1.50
$K_I = K_I^P + K_I^{\text{res}}, \text{ MPa}\cdot\text{mm}^{1/2}$	-254	+179	+305
$K_I = K_I^P + K_I^{\text{res}}, \text{ MPa}\cdot\text{m}^{1/2}$	-8.03	+5.66	+9.6

If we use the data of Figure 11 from study [10], at the above values of K_I the rate of growth of a stress corrosion crack is not in excess of $5 \cdot 10^{-5} \text{ mm/h}$ at $c = 1.5 \text{ mm}$, $1 \cdot 10^{-5} \text{ mm/h}$ at $c = 1.0 \text{ mm}$, and much lower — $1 \cdot 10^{-6} \text{ mm/h} = 0.00876 \text{ mm/yr}$ at $c = 0.45 \text{ mm}$. It can be assumed with certain conservatism that this law of decrease in the rate of growth of a corrosion crack will persist with decrease in the values of c from 1.50 to 0.45 mm due to corrosion. At $c \approx 0.5\text{--}0.6 \text{ mm}$, the crack is closed because of a negative value of $P = -10 \text{ MPa}$, and corrosion fracture is negligible.

Therefore, based on 15–20 years of service life of the steam generator, there is no reason to think that the calculated values of c of the welded joints in pipes will be lower than 0.45 mm. Therefore, in terms of maintaining integrity of the welded joints under consideration, it is permitted that the excessive pressure in tests be up to 2.7 MPa.

- (1992) *Inspection procedure 320.585.00.00.000*: Steam generator PGV-1000M. Air-hydraulic aquarium method for testing of leak-tightness. PM2/GKAE OKB «Gidropress». Podolsk.
- Harrison, R.P., Loosemore, K., Milne, J. et al. (1980) *Assessment of the integrity of structures containing defects*. Rep. R/H/RG, Rev. 2. Berkley.
- (1988) *Fracture mechanics and strength of materials*: Refer. book. Ed. by V.V. Panasyuk. Vol. 2: Savruk, M.P. Stress intensity factors in bodies with cracks. Kiev: Naukova Dumka.
- (1968) *Strength, stability, oscillations*. Ed. by I.A. Birger et al. Vol. 1. Moscow: Mashinostroenie.
- Melekhov, R.K., Pokhmursky, V.I. (2003) *Structural materials for power generation equipment*. Kiev: Naukova Dumka.
- Makhnenko, V.I., Velikoivanenko, E.A., Makhnenko, O.V. et al. (2002) Computer program «Welding of tubes to tube sheets of heat exchangers». *The Paton Welding J.*, **8**, 2–9.
- (1994) *Inspection of metal state*: Report on investigation of causes of sticking of heat-exchanging pipes to first loop collector, adjoining zones of pipes and deposited beads in PGV-1000M of KhNPP unit No.1. 320-EKO-320. GKAE OKB «Gidropress». Podolsk.
- (1989) *PNAE G-7-002-86*: Standards for strength design of equipment and pipings at nuclear power plants. Moscow: Energoatomizdat.
- Krasovsky, A.Ya., Orynyak, I.V. (2000) Assessment of residual life of welds in pipings of the first loop of nuclear power stations damaged by intercrystalline corrosion. *The Paton Welding J.*, **9/10**, 54–62.
- Horn, R.M., Kass, J.N., Rangantath, K. (1984) Evaluation of growth and stability of stress corrosion cracking in sensitized austenitic pipes. *J. Pressure Vessel Technol.*, **106**(2), 201–208.



IMPROVEMENT OF QUALITY OF PERMANENT JOINTS --- WAY TO PROLONGATION OF SERVICE LIFE OF HEAT-GENERATING ASSEMBLIES*

I.M. NEKLYUDOV, B.V. BORTS, A.F. VANZHA, A.T. LOPATA, N.D. RYBALCHENKO,
V.I. SYTIN and S.V. SHEVCHENKO

NSC «Kharkov Physical-Technical Institute», NASU, Kharkov, Ukraine

Possibilities of producing stable permanent joints of zirconium-base alloys and stainless steel, used in fuel rods of a number of nuclear reactors, and in sensors and probes of the reactor control instruments are investigated. By the method of solid phase welding joints of zirconium and stainless steel with interlayers from niobium and copper are investigated, which allow the items working in corrosive environment under conditions of thermocycling and alternating loading. Connection between structural changes of the composite and its weakening in the process of action on it of variable thermal fields is studied.

Keywords: zirconium, stainless steel, welding, solid phase, composite material, damping and barrier interlayers, structure, thermocycling, strength

Fuel rods of a number of reactors, and sensors and probes of the reactor control instruments contain permanent joints of zirconium with steels. That's why problem of producing reliable and long-lasting joints of elements of the structures, fabricated from materials, having different properties and suitable for operation under rigid (variable thermal and radiation fields) conditions, is rather actual.

Existing technical solution of manufacturing permanent joints of zirconium-base alloys and stainless steel does not ensure complete correspondence to more stringent safety requirements, established for nuclear reactors.

Permanent adhesion joints of dissimilar metals and alloys on their basis, in particular, of zirconium and steel, may be at present produced by different methods, for example, explosion welding, joint pressing, diffusion bonding, brazing, etc. [1, 2]. Such methods of formation of adhesion welds between dissimilar metals and alloys on their basis, in particular, between zirconium and steel, may ensure for the adhesion weld in initial state rather high strength properties, while action on structural materials of this type (which have in their composition adhesion welds, formed directly between zirconium and stainless steel) of high heat fluxes at increased temperatures inevitably causes occurrence near the adhesion weld of the brittle intermetallic phases, which can invoke occurrence of brittleness and loss of integrity of the structure.

One of essential factors, determining reliability and durability of the items from composite materials working under rigid conditions (high heat fluxes at increased temperatures), is introduction into composition of the composite of the barrier and intermediate

interlayers. Rational selection of intermediate (damping and barrier) interlayers can ensure within a long time of operation at increased temperatures high structural strength of the composite, high values of impact toughness, vacuum and corrosion resistance, and other operation properties.

The work is directed at substantiation of selection of the barrier and damping interlayers and investigation of the possibility of producing stable permanent joints of zirconium-base alloys and stainless steel.

Materials and methods of investigations. Zirconium alloys and steel 12Kh18N10T in austenized state were used for producing the composites. Heating and deformation of the packages were performed on the DUO-170 vacuum rolling mill, designed in NSC «KPTI» [3].

Melting of experimental ingots of the materials, used as the barrier and damping interlayers, was performed on the electron beam installation in vacuum not less than $1 \cdot 10^{-3}$ Pa. Solidification of the materials, except copper-base ones, was performed in copper water-cooled mould. Copper materials were solidified in a water-cooled mould with graphite insert in stepwise drawing of the ingots. Metallographic investigations of the material structure were performed on longitudinal and transverse microsections using the MIM-8M microscope.

Mechanical properties of the composites were determined using cylindrical specimens, cut out from the composites over their thickness perpendicular to the boundary of linking of the layers. Thermocyclic tests were performed on annular specimens within temperature range 200–800 °C at the temperature increase rate 50 deg/min; the tests were continued till loss of continuity of the joints.

Results of the investigations and discussion thereof. *Structure of the zirconium–niobium–copper–*

*The article is based on the results of accomplishment of NASU target integrated program «Problems of life and safety of structures, constructions and machines» (2004–2006).

© I.M. NEKLYUDOV, B.V. BORTS, A.F. VANZHA, A.T. LOPATA, N.D. RYBALCHENKO, V.I. SYTIN and S.V. SHEVCHENKO, 2007

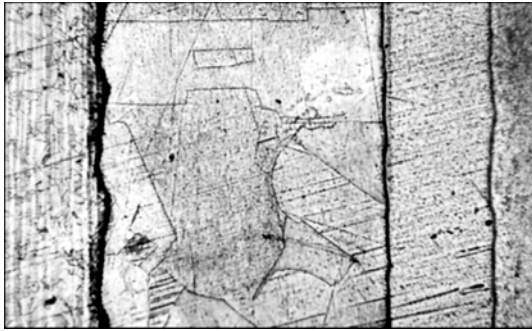


Figure 1. Microstructure of zirconium-niobium-copper-steel composite in initial state ($\times 70$)

steel composite. One can see from Figure 1 that boundaries of linking of the dissimilar material layers are clean. Transitional zones were not detected after etching. X-ray microspectral analysis showed presence of solid soluble zones on the boundaries of linkages niobium-copper (Figure 2, a) and niobium-zirconium (Figure 2, b).

Kinetics of thermal fatigue of laminated structural materials. In case of action on the composite

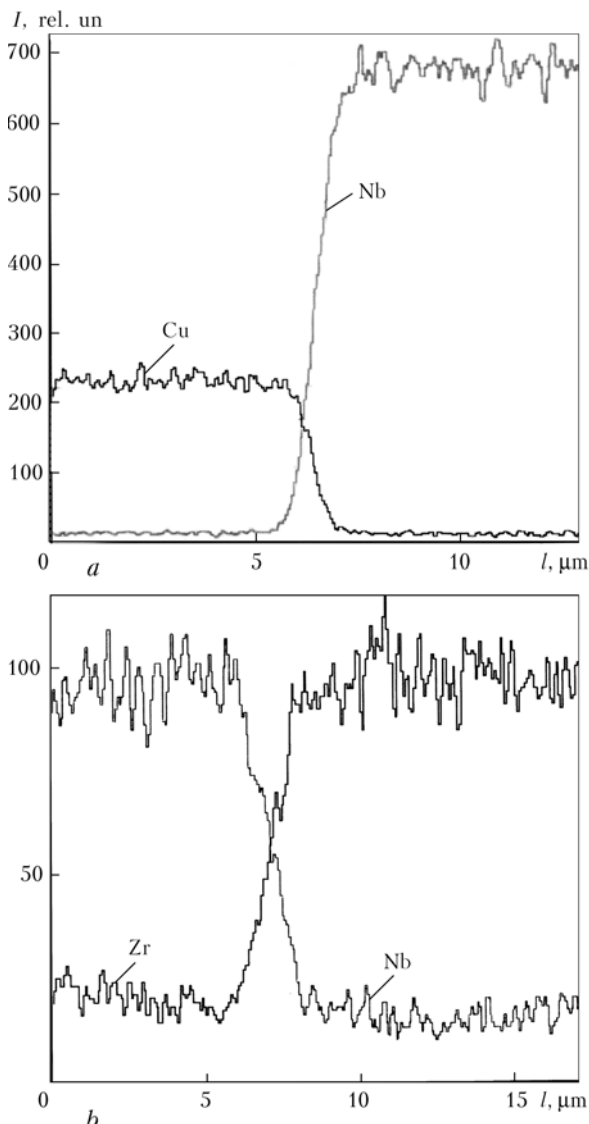


Figure 2. Spectra of X-ray microspectral analysis near linkage boundaries: a — niobium-copper; b — niobium-zirconium

material of the variable thermal field, mechanical stresses caused by the gradient of temperatures in the material, are manifested in it, substantiated by different coefficients of thermal expansions of the metals constituting the composite. Relaxation of the mechanical stresses, occurring under action of the variable thermal fields, is accompanied by generation and migration of dislocations and accumulation of extra-equilibrium concentrations of vacancies. Accumulated excessive number of the crystalline lattice faults stimulates, in its turn, processes controlled by diffusions: formation of the phases, re-crystallization, polygonization, etc. Under action of cyclic stresses increases thermodynamic potential of the system, changes, in comparison with static conditions, activation energy of the relaxation processes, originate new directions of diffusion flows, impurities and alloying additives, which are present in the materials that constitute the composite, are redistributed, structural defects are originated, pores are developed, and cracks are formed.

Investigations of the kinetics of formation and development of structural defects show that structural changes in the process of action on the laminated structural material of the thermal field variables are manifested in the softest component of the composite, whereby structure of the main more rigid components practically does not change. Structural changes in soft component of the composite are the result of the deformation processes, implemented by sliding, twinning, and intergrain slippage; processes of accumulation of point defects, propagation and annihilation of dislocations, formation and disintegration of dislocation accumulations, and formation and recovery of pores, microcracks, and cracks. Process of thermal-cycle fatigue of the soft layer is characterized by high intensity of accumulation of structural defects. After first thermal cycle (Figure 3, a) in the soft copper layer intragrain slip bands are manifested, one part of which is stopped on the grain boundaries, and the other — at significant distance from the boundaries. So, after several thermal cycles of the niobium-copper-steel composite within temperature range 300–800 °C in the copper layer a significant deformation relief is manifested. By means of increase of the heat condition changes, the number of slip bands, their length and intensity increase, and after 15–20 changes of heat conditions (Figure 3, b, c) process of formation of new slip bands practically stops: confluence of adjacent bands into wide slip bands, which are arranged parallel or at a small angle to the boundaries of linkages of the composite components, is manifested.

Formation of wide slip bands proves intensification of the diffusion processes, which facilitate creeping of the dislocations. Slip bands are arranged non-uniformly over the soft layer thickness. So, as the number of thermal cycles increases, deformation bands localized in the process of first thermal cycles near boundaries of linkage of copper with niobium and steel (in case of the niobium-copper-steel composite), propa-

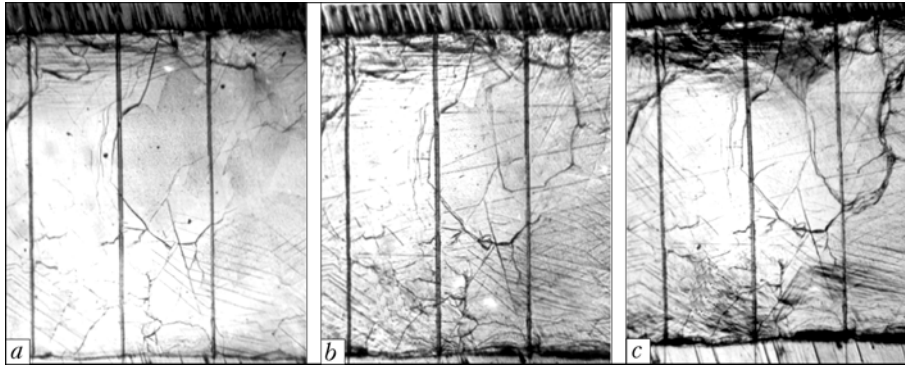


Figure 3. Microstructure of niobium–copper–steel composite within thermocycling temperature range 300–800 °C after one (a), 15 (b) and 20 (c) thermocycles ($\times 70$)

gate over the whole thickness of copper layer, whereby non-uniformity of distribution preserves: their density is maximal near boundary of linkage of copper with niobium, somewhat lower near boundary of linkage of copper with steel, and minimal in middle part of the layer.

In the process of thermocyclic action on the composite, composition of which includes a damping copper layer, in the latter signs of grain-boundary slippage and migration of grain boundaries is manifested (Figure 4). Initially after several changes of heat conditions migration of grain boundaries in the copper interlayer is observed practically over the whole thickness of the interlayer. Exception constitutes a zone of 3–5 μm width near boundary of linkage of copper with steel (for the niobium–copper–steel composite). As number of heat condition changes increases, width of the zone, in which migration of the grain boundaries is blocked, grows: in the copper layer of 0.8 mm thickness of the laminated composite with the main constituting component metals of niobium and stainless steel 12Kh18N10T, width of the zone, adjacent to stainless steel, in which boundaries of the grains are blocked, is about 30 μm , after 50 thermocycles — 45 μm . It should be noted that in this zone of the copper layer more fine-grained structure is formed; its width, as show the estimations, corresponds to diffusion penetration into copper of nickel from stainless steel.

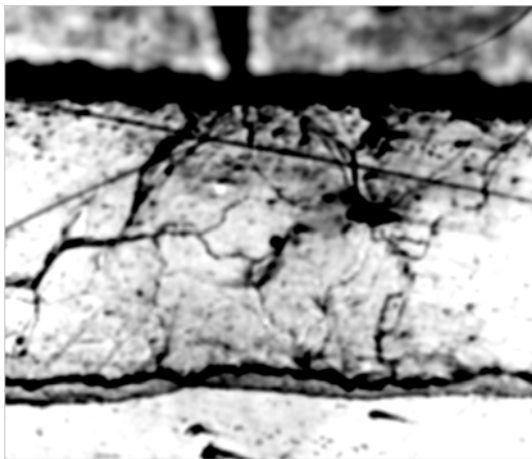


Figure 4. Grain-boundary slippage and migration of grain boundaries in niobium–copper–steel composite within thermocycling temperature range 300–800 °C after 25 thermocycles ($\times 70$)

After 25–30 thermocycles in copper layer of the niobium–copper–steel composite appear resolvable in optical microscope micropores, origination and growth of which are observed near boundaries of linkage of copper with steel within thickness range 25–50 μm , mainly on boundaries of the grains located parallel to boundary of linkage of the components.

First pores appear near free surface of the composite. As number of heat condition changes increases, pores appear at ever increasing distance from the surface, being located mainly in the near-boundary area of the copper layer — near boundaries of copper linkage with niobium. Further increase of heat condition changes causes increase of number and size of the pores, confluence of the latter, and formation of microcracks (Figure 5) all over perimeter of the specimen. In case of the zirconium–steel composite material with barrier interlayers from niobium and damping interlayer of copper a microcrack is formed at the distance of 20–50 μm from boundary of linkage of copper with steel.

Heat stability of the bimetal zirconium–steel transition elements. Results of investigation of heat influence on properties of zirconium- and stainless steel-base laminated composite materials are presented in Tables 1 and 2.

The investigations showed that application of the system of interlayers allowed developing zirconium- and steel-base laminated composites suitable for long operation under conditions of increased non-stationary temperature and force fields. The best complex of

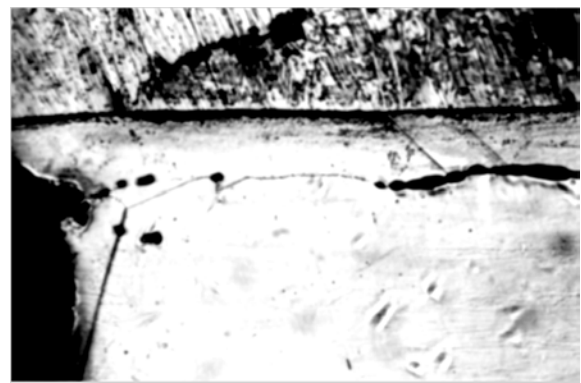


Figure 5. Microstructure of niobium–copper–steel composite within thermocycling temperature range 300–800 °C after 35 thermocycles ($\times 300$)

Table 1. Influence of thermal actions on properties of laminated composite materials on basis of zirconium alloys and stainless steel

Composite	Intermetallic zone width, μm , after annealing, $^{\circ}\text{C}$, for time, h			Number of thermocycles before loss of continuity in thermocycling at $200\text{--}800\text{ }^{\circ}\text{N}$
	Initial	$700\text{ }^{\circ}\text{N}$, 100 h	$1000\text{ }^{\circ}\text{N}$, 10 h	
Zirconium--steel	1--3	10--15	--	5--10
Zirconium--niobium--copper--steel	N/D	N/D	N/D	80--90
Zirconium--chromium--steel	Same	Same	Same	35--45
Zirconium--vanadium--nickel--steel	1--3	5--10	--	10--15

Table 2. Strength of zirconium composite specimens in layer tear tests

Composite	Heat treatment, $^{\circ}\text{N}$					
	20		300		700	
	Tensile strength, MPa	Place of failure	Tensile strength, MPa	Place of failure	Tensile strength, MPa	Place of failure
Zirconium--steel	450	Boundary	350	Boundary	250	Boundary
Zirconium--niobium--copper--steel	400	Copper	270	Copper	120	Copper
Zirconium--chromium--steel	430	Chromium	370	Chromium	280	Chromium
Zirconium--vanadium--nickel--steel	460	Boundary	320	Boundary	230	Boundary

properties was manifested by composites with interlayers of copper or a system of copper--niobium interlayers.

In the course of the investigations connection between structural changes of the composite and its weakening in the process of action on it of variable thermal fields was detected. Reduction of the composite material strength by means of increase of thermocycles is stipulated by accumulation of defects in the soft damping layer. Micropores and microcracks over grain boundaries and microcracks near boundaries of linkage of the components form in it.

Thermocyclic endurance of laminated composite materials may be enhanced by increase of structural-phase stability of materials of the barrier and damping interlayers, in particular, due to introduction into them of microadditions of chemically active elements [4].

So, technological scheme of joints (zirconium--stainless steel) in solid phase on the basis of formation of interatomic bonds between dissimilar materials for

application in the WWER-1000 reactor is developed and investigated. New technological process is designed to replace mechanical attachments used in limit switches of fuel rods. Zirconium--steel joints with niobium--copper interlayers, which allow the items operating under conditions of thermocycling and alternative loads at high temperatures, are investigated.

1. Icefelier, H. Frank, K., Vojzinger, H. (1969) Zirconium--steel joints for evaporated-overheated solid-oxide fuel cells. *Atom. Tekhnika za Rubezhom*, **2**, 37--41.
2. Frolov, N.G., Shilkov, Yu.B. (1974) Joint pressing welding of stainless steel with zirconium alloys. *Svarochn. Proizvodstvo*, **5**.
3. Borts, B.V., Neklyudov, I.M., Lopata, A.T. et al. (2005) Study of welding processes of multilayer structures from crystallites of various chemical compositions promising for nuclear power applications. *Voprosy Atom. Nauki i Tekhniki. Series Physics of Radiation Damages and Radiation Materials Science*, **5**, 156--158.
4. Lopata, A.T., Neklyudov, I.M., Shevchenko, S.V. et al. (2001) Role of microalloyed damping and barrier interlayers in increase of thermocyclic life of composite material on the base of titanium and stainless steel. *Nauchn. Vedomosti*, **14(1)**, 168--171.



TIG WELDING OF TITANIUM AND ITS ALLOYS (REVIEW)

V.E. BLASHCHUK

E.O. Paton Electric Welding Institute, NASU, Kiev, Ukraine

Peculiarities of utilisation of TIG welding methods for joining titanium and its alloys are considered. Recommendations are given for application of different welding methods, and their advantages and drawbacks are noted.

Keywords: arc welding, tungsten electrode, titanium alloys, shielding gas, immersed-arc welding, narrow-gap welding, through-penetration welding, plasma welding, microplasma welding, technology, metal thickness, defects, quality inspection

Titanium and its alloys are widely applied as structural materials in modern engineering owing to their high specific strength and corrosion resistance, as well as heat resistance in certain temperature ranges. Arc welding is a leading technological process for production of permanent joints. Main difficulties arising in welding of titanium are associated with its high-temperature reactivity (particularly in molten state) with respect to air components. In this case, a mandatory requirement for production of a quality joint is to ensure reliable shielding of not only the zone of a joint, but also its cooling regions (to a temperature of 300–400 °C) from contact with atmospheric gases. In fusion welding, it is also necessary to ensure a quality shielding of the weld root, even if metal is heated above the said temperature, but is not melted yet [1–4].

Substantial amounts of different-application wrought titanium alloys were developed and are commercially applied all over the world. Depending upon the character of impact on titanium by different alloying elements, and proceeding from the type of structure, its commercial alloys can be subdivided into the following groups [2, 3, 5, 6]:

- α - and pseudo α -alloys (based on the α -phase with 2–7 % of the β -phase in equilibrium state). They have good workability (all types of semi-finished products can be made from them), satisfactory ductility, weldability and high corrosion resistance in aggressive environments. Alloys of this grade can be fusion welded in a wide range of process parameters. Welded structures of these alloys are subjected to incomplete annealing at a temperature below 700 °C;

- two-phase $\alpha + \beta$ - and pseudo β -alloys (structure is based on the β -phase with a small amount of the α -phase). These alloys acquire satisfactory properties after annealing. However, wide application of such high-strength alloys in welded structures is hampered by insufficient ductility of the joints in a heat-hardened state. One-pass welding without groove preparation is indicated to produce welded joints of alloys of this grade. Depending upon the service conditions,

welded joints are subjected to annealing or strengthening heat treatment, i.e. quenching and ageing;

- β -alloys are high alloys with stable structure of the β -phase, having high corrosion resistance. The most promising welding methods to produce joints in these alloys are argon-arc and electron beam welding.

Almost all welding methods used for joining steels and non-ferrous metals can be applied to fabricate welded structures of titanium and its alloys [3–11]. However, the manual covered-electrode welding method has not yet been developed for titanium. The quality of welded joints in titanium is determined in many respects by a specific thermal-deformation cycle of arc welding, which differs from that in the case of welding steels. In titanium welding, the losses of energy are lower, whereas the time of dwelling of the HAZ metal in a range of high temperatures is 2–3 times longer. Sensitivity to the thermal cycle of welding shows up in $\alpha \rightarrow \beta$ transformation, rapid growth of grain of the high-temperature β -phase in heating above the range of structural transformations, overheating and formation of brittle phases in cooling and ageing.

High reactivity of titanium with respect to air components ([O], [N], [H]) leads to saturation of the welded joint metal with these components, while this, in turn, leads to its embrittlement, decrease in mechanical properties (ductility, long-time strength) and corrosion resistance. Substantial saturation of metal during welding occurs as low as at $T \geq 350$ °C. In this connection, it is necessary to ensure reliable shielding of the welding zone having a temperature of 350 °C from the contact with air. This is achieved by using argon of the first and highest grades (GOST 10157 and EN 439), high-purity helium (TU 51-940-8 and EN 439), their mixtures (EN 439) and special oxygen-free fluxes. Welding in vacuum also excludes the probability of interaction of titanium with gases.

The necessary condition for production of quality joints in titanium and its alloys is regulation of mechanical properties and structure of the weld and HAZ metals through selecting optimal technologies and welding consumables, as well as welding parameters that provide a minimal heat input during welding. The quality of the resulting welded joints is determined in many respects by the technology used for



preparation of edges for welding and composition (grade) of titanium filler wire.

Edges in billets are prepared by using gas, plasma and laser-gas cutting (cutting gas --- argon) [12]. Gas cutting of titanium is performed at a higher speed and lower power of the flame, compared with cutting of steel. This is associated with a more intensive evolution of heat within the cut zone. After gas and plasma cutting, machining of the edges should be performed to a depth of 3–5 mm. No such need exists after laser-gas cutting. In machining, roughness of the edge surfaces should be not worse than $Rz = 40$ (GOST 2789). Surfaces of billets adjoining the edges on both sides to a distance of not less than 20 mm can be cleaned with a scraper, electrocorundum disk, rotating metal brush, fine emery cloth, disks with abrasive material knurling or vulcanite disk. In cleaning with abrasive disks, no overheating of metal causing formation of temper colours on the surface of a welded joint is permitted. Prepared surfaces of the welded joint and welding wire should be degreased immediately before tack welding and welding. Moisture from them should be removed using calico cloths wetted with acetone and commercial ethyl alcohol.

The choice of a method for welding titanium alloys should be based on the requirement to ensure reliable shielding of the welding zone and cooling regions of the joint from contact with air, as well as peculiarities of joining metal of small, medium and large thickness.

Arc welding methods are widely used for titanium, the most common of them being TIG welding (automatic, mechanised or manual). These methods will be considered in this study.

TIG welding is versatile, as it allows joints to be made in different spatial positions, including under

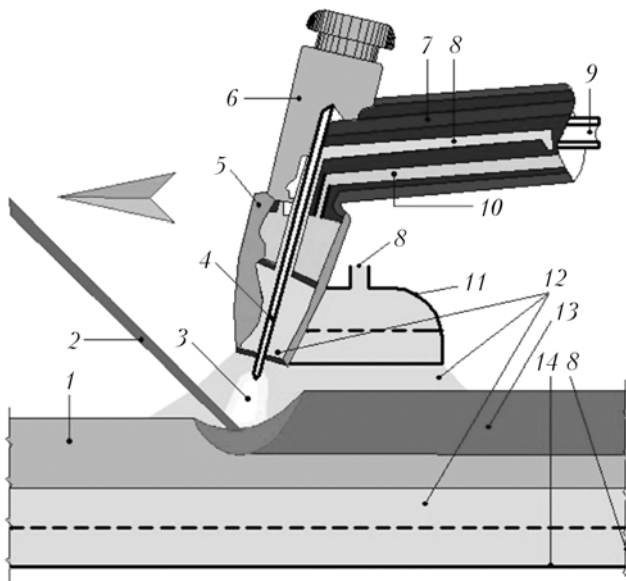


Figure 1. Flow diagram of manual TIG welding of titanium: 1 --- base metal; 2 --- filler wire; 3 --- arc; 4 --- tungsten electrode; 5 --- nozzle; 6 --- torch body; 7 --- feeding of cooling water; 8 --- feeding of shielding gas; 9 --- current conductor; 10 --- removal of water; 11 --- shroud for protection of cooling weld regions; 12 --- shielding atmosphere; 13 --- weld metal; 14 --- device for protection of the back side of the weld

restrained conditions, and requires no re-adjustment of equipment in changes of metal thickness or type of a joint.

TIG welding of titanium is performed at a direct current of straight polarity. Tungsten electrode serves as a cathode, and the welding process stability, quality of the weld formation and penetration depth depend in many respects upon its fracture resistance, shape of the sharpened tip and stability of emission ability. Electrodes of pure (non-alloyed) tungsten are unsuitable for welding of titanium because of their low fracture resistance. Alloyed tungsten electrodes of the EVL (WL10), EVI-2 and EVT-12 (WT20) grades, according to GOST 23949–80 (EN 26848 NF), are used for this welding method. Diameter of the tungsten electrode is selected depending upon the amperage, allowing for the permissible current load. Sharpening angle is 30–45°. Prior to welding, the sharpened tungsten electrode is subjected to treatment by the five-fold arc ignition at a working current. In long-time operation, the electrode is gradually destroyed, and it is necessary to periodically re-sharpen it [5, 6, 9].

The following types of inert gas shielding of the welding zone are used depending upon the size and configuration of titanium pieces being welded [5, 6, 9]:

- general shielding of a workpiece in a chamber with the controlled inert gas atmosphere, providing the most reliable and stable protection of the welding zone and cooling regions of a welded joint from the top and bottom of the weld root. It is applied in mass production and in manufacture of complex configuration parts;

- local shielding of a welded joint using small-size chambers, providing consistent quality of position and roll butt joints in welding of tubular structures. The back side of the weld in this case is protected by filling the cavity of a billet or its part with inert gas;

- spray shielding of the welding zone and cooling regions of the joint, which is provided by their continuous blowing using a nozzle with increased opening and extended shroud, compared with welding of other metals. Blowing of the weld root is performed by feeding inert gas from the bottom. In this case, the shielding gas is fed via three channels, i.e. to nozzle 5, extended shroud 11 and protecting forming backing 14 (Figure 1). Despite the fact that in this case it is difficult to ensure a reliable shielding, this welding method has received wide acceptance in welding industry. Consistent and high quality of the welded joints made in air is assured by using automatic welding.

In manual TIG welding, shroud 11 (see Figure 1) fixed on the torch is used to protect the cooling regions of the welded joints. Width of the shroud is selected depending upon the width of HAZ of a welded joint, and length in welding of a thin plate is found from the following expression:

$$I = (0.006 I_w^2 U_a^2) / (T^2 v_w b)^{-d_n/2},$$

where I_w is the welding current, A; U_a is the arc voltage, V; T is the temperature below which the metal requires no protection ($T < 400$ °C); v_w is the welding speed, cm/s; b is the metal thickness, cm; and d_n is the inner diameter of the nozzle, cm.

Shielding of the weld root and adjoining heated regions of a welded joint is provided by tightly pressing edges to copper or steel backings with forming grooves and a system of holes to feed the shielding gas (Figure 2) [5, 6, 9].

Maximal welding current is limited to avoid overheating of metal of the weld edges in arc welding of titanium. For example, the current in TIG welding with the surface arc should not exceed 300 A. This allows welding of titanium plates with $b \leq 3$ mm in one pass without groove preparation. Butt joints in thicker titanium plates are made by multi-layer welding with groove preparation using filler wire. The following groove preparation is used for welding titanium: V-groove with opening angle of 70–90° for plates 4–10 mm thick; X-groove with opening angle of 50–70° for plates with $b = 10$ –15 mm; wineglass shaped groove with opening angle of 30° for plates with $b > 15$ mm. Root face in all the cases is 1.5–2.0 mm, and gap is no more than 10 % of thickness of a titanium plate.

To remove air from the gas system, the shielding gas and protective devices are fed to the torch 1–2 min before the beginning of welding. The arc is ignited by touching a workpiece with tungsten electrode (Figure 3, a) or by means of an oscillator (Figure 3, b). Prior to welding, it is recommended to check the quality of shielding on a titanium specimen under common welding conditions by igniting the arc on the «spot», which should have a bright silvery colour. Manual welding is performed without weaving of the torch at a short arc by the forward angle method. The angle between the electrode and filler wire is maintained within a range of 90°, and wire is fed in a continuous mode. In this case it is necessary to make sure that the heated tip of the filler wire is permanently shielded with the inert gas. If for some reasons whatsoever it has been affected by air, the oxidised tip should be removed by a mechanical method. Upon completion of welding or after an accidental extinguishing of the arc, the shielding gas should be fed until the metal cools down to $T < 400$ °C.

The efficiency of gas shielding in welding and subsequent cooling of the welded joint can be evaluated from appearance of the weld: its bright silvery surface is indicative of a good shielding and high properties of the joint. Shielding is considered satisfactory if the surface of the weld has straw-yellow colour. Such a weld can be left without repair. If the weld surface has a light-blue colour, it should be cleaned with a metal brush. Welds with a blue or grey surface are inadmissible and should be removed.

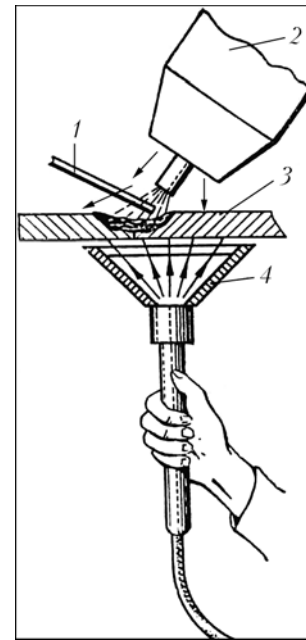


Figure 2. Schematic of protection of the weld root in repair welding: 1 — filler; 2 — torch; 3 — workpiece; 4 — local blowing

It is necessary to take into account that a good shielding in welding affects not only the weld quality but also the tungsten electrode life.

Titanium welding wires of different compositions, which, according to GOST 27265–87 and AWS A5.16/A5.16M:2004 [3, 4, 9, 13], are supplied in the etched and degassed condition, were developed and are commercially manufactured for welding titanium alloys of different grades. Rods of the base metal, which should be subjected to preliminary vacuum annealing, can also be utilised as fillers. In welding corrosion-resistant titanium alloys containing small additions, for example, of palladium or ruthenium, the filler wire should also be alloyed with these elements to ensure required corrosion resistance of the weld metal.

Approximate conditions of manual TIG welding of titanium are as follows: $b = 3$ (10) mm, tungsten electrode diameter $d_w = 2.5$ –3.0 (3.0–4.0) mm, filler

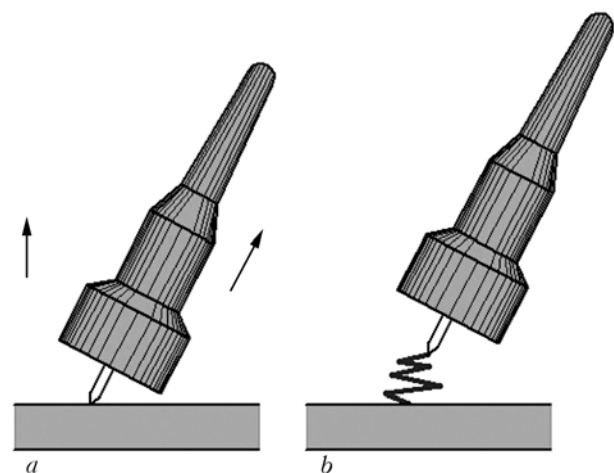


Figure 3. Schematic of arc ignition in manual TIG welding of titanium using a torch with «gas lens» provided by touching (a) and by means of an oscillator, i.e. arc stabilisation device (b)

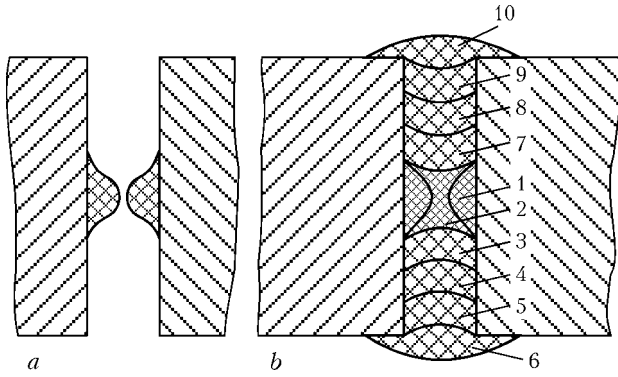


Figure 4. Schematic of sequence of welding over a slot gap: *a* — joint with deposited beads assembled for welding; *b* — sequence of making passes (designated by numerals)

wire diameter $d_f = 2.0\text{--}3.0$ (2.0–3.0) mm, $I_w = 120\text{--}150$ (160–200) A, $U_a = 10\text{--}14$ (12–16) V.

The technology for slot-gap welding of low titanium alloys without groove preparation was developed to raise the productivity of manual TIG welding of thick plate titanium structures ($b \geq 15$ mm). Compared to welding with X-groove, this technology has the following advantages: 2–3 times decrease in volume and weight of the deposited metal, which allows amounts of expensive welding consumables used for welding to be reduced, and the productivity of the welding process to be increased 2–3 times; possibility of regulating mechanical properties of the welded joints both through changing chemical composition of welding wires and through using the effect of contact strengthening of the weld metal operating under conditions characteristic of the so-called soft interlayers; presence of the slot gap that improves gas shielding, stabilising the welding process and increasing the efficiency of a heat source; reduction of overheads owing to decrease in machining of edges for welding, as well as consumption of electric power [1, 5].

Prior to assembly for welding, run-out tabs of titanium plates with $b = 3\text{--}4$ mm are welded to the preliminarily machined ends of the edges, and a three-layer beads are deposited in central part of an edge (Figure 4, *a*). Smoothing beads are often deposited using no filler to ensure smooth transition from the deposited bead to the base metal edges. The pieces thus prepared are assembled for welding and tack welded with a gap of 2–3 mm between the deposited layers.

Slot-gap welding of the joints is performed in a certain sequence (Figure 4, *b*). First the connecting welds ($I_w = 160\text{--}180$ A) are made, then the first pass using filler wire ($d_f = 3\text{--}4$ mm) and second pass on the back side using no filler are made. The main layers are deposited at $I_w = 380\text{--}400$ A and $d_f = 5$ mm.

Quality joints can be produced providing that the surface of each layer has a concave meniscus shape with smooth transition to edges of the pieces welded, which eliminates the probability of lacks of fusion between the beads.

Slot-gap welding has a number of peculiarities. For example, extension of tungsten electrode at $d_f = 4$ mm is set so that the torch nozzle is at a distance of 2 mm from the surface of the plates welded. The electrode axis should be normal to the surface of the plates, and the back side of the weld should be protected from oxidation with an argon flow fed via a tube with radial openings (Figure 5).

The flow rate of argon should be 12–14 l/min for deposition of inner layers. A narrow and deep slot provides quality protection of the deposited metal using no shrouds. The use in this case is made of the reflecting shield, which is put on the torch nozzle. A shroud is used for deposition of outer layers to additionally feed 6–8 l/min of argon. The technology for narrow-gap magnetically-impelled arc TIG welding was offered for joining titanium plates with $b = 110$ mm [11]. The welds made by these technologies are characterised by a high quality. They are free from pores and other defects.

The method for TIG welding using fluoride fluxes in the form of pastes (TIG-F) was developed and first applied to raise the efficiency of TIG welding of titanium alloys [5–7]. TIG-F welding widens technological capabilities of the arc, allows the penetration depth to be increased, heat input of the welding process to be reduced, and formation of pores in the weld metal to be prevented. This welding method makes it possible to weld titanium plates with $b \leq 6$ mm in one pass without groove preparation, make welds of any type both with and without filler wire, in flat position and on a vertical plane. Consumption of the flux does not depend upon the thickness of the metal welded, and is about 10 g per running meter of the weld.

Further development of the TIG-F welding method is welding using filler wire, which provides welds in

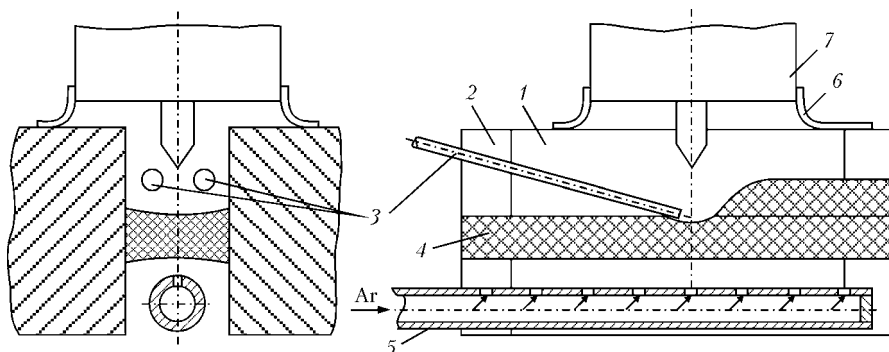


Figure 5. Flow diagram of slot-gap welding: 1 — piece being welded; 2 — run-out tabs; 3 — twin filler; 4 — deposited metal; 5 — back flow device; 6 — reflecting shield; 7 — torch nozzle



one pass without groove preparation on titanium plates with $b = 5\text{--}16$ mm. Consumption of filler wire is about 1.5 m per running meter of the weld. The resulting weld metal is pore-free. However, TIG-F welding requires a high accuracy of assembly of pieces for welding [5–7, 14].

Mechanised and automatic TIG welding has also found wide acceptance. These welding methods allow the size and shape of welded joints to be varied over wide ranges, and provide welds with satisfactory quality of the surface. Welding of titanium plates with $b \geq 6$ mm is performed by the two-sided technique. Drawbacks of these welding methods include sensitivity of the weld metal to formation of porosity, and a high level of distortions in the welded joints. Application of pulsed-arc welding (Figure 6) allows elimination or decrease of these drawbacks. Sizes of the welds can be varied over wide ranges by regulating the current, speed, as well as duration of the pulse and pause. Pulsed-arc TIG welding provides good formation of the weld with smooth transition to the base metal, and decreases non-uniformity of the field of residual stresses and level of their concentration within the welding zone in operation of parts under loading [5, 6].

Modifications of this process were developed to increase the penetrating power of the arc in TIG welding: immersed-arc welding with and without electromagnetic stirring of the weld pool metal, through-penetration welding, twin-arc welding, etc. [1, 3–7, 9–12, 15–17].

In immersed-arc welding, the tungsten electrode tip is lowered below the surface of the base metal using a special forced automatic (sometimes manual) system for regulation of the arc voltage. Increase in the efficiency of thermal power of the arc makes it possible to weld titanium plates with $b \leq 15$ mm in one pass without groove preparation, and with $b \leq 36$ mm by two-sided welding. In this case, welds on each side of a plate are made in two passes using no filler wire: the first pass is made with the immersed arc to provide the required penetration depth, and the second pass is made with the surface arc to smooth the weld and impart it the required geometric sizes. Drawbacks of this welding method include a wide width of the welds, coarse-crystalline metal structure, impossibility of regulation of its chemical composition, and high sensitivity to porosity. Welding with electromagnetic stirring allows structure of the weld metal to be improved and its porosity to be substantially decreased [1, 15, 17].

The technology and equipment for welding using two tungsten electrodes located in a plane normal to the weld axis were developed to raise the deposition efficiency in multi-layer one-sided groove TIG welding of titanium plates ($b \leq 50$ mm). With this method, welding of titanium plate with $b = 50$ mm is performed in 6–8 passes using filler wire ($d_f = 5\text{--}7$ mm). This welding method is also applied for cladding [5, 16].

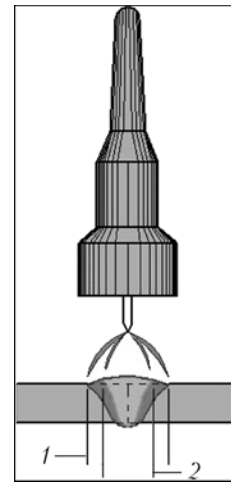


Figure 6. Schematic of geometry of cross section of the weld metal in continuous- (1) and pulsed-arc (2) TIG welding

Through-penetration TIG welding allows joining of titanium plates with $b \leq 12$ mm in one pass. To provide a keyhole penetration, the set length of the arc should be 0.5–1.0 mm, and welding parameters should be set so that a hole filled with liquid metal is formed under the moving arc. The second pass using filler wire is required to form the weld reinforcement.

Surface-arc TIG welding is used to make roll and position butt joints in pipelines, as well as to weld tubes into tube plates. In this case it is necessary to employ specialised equipment, which is inapplicable to other welding methods [1, 5, 6, 18].

Plasma welding (PW), along with TIG welding, is used to make permanent joints in titanium without groove preparation on parts with $b \leq 10$ mm. This welding method requires the same protection means as TIG welding. Filler wire can be introduced into the leading portion of the weld pool. Less stringent requirements are imposed on the filler wire feed speed and diameter in PW, compared with TIG welding. PW is performed with one- or two-sided V-groove [1, 5, 6, 19].

Titanium sheets with $b \leq 1.5$ mm are joined by microplasma welding (MPW), which is performed at a direct current of straight polarity using the arc burning in the continuous or pulsed mode. Argon is used as a plasma gas, and helium or a mixture of Ar + 50–75 % He is used as a shielding gas. Titanium parts with $b \leq 0.3$ mm are welded by flanging the edges. Mean working length of the arc in MPW is almost an order of magnitude larger than in TIG welding. Therefore, with this welding method larger deviations of the arc length from the set one are permitted, which has no significant effect on the weld parameters. The shape and size of the joint are of special importance in terms of ensuring the stable weld formation [5, 6, 20].

Chemical apparatuses of titanium, e.g. hydrolysis one of 47 m³ (Figure 7), are fabricated by using several welding methods. It should be noted that manual TIG welding is unavoidable in this case. All welds on the casing of the apparatus were made by automatic immersed-arc TIG welding using no filler, welds in the

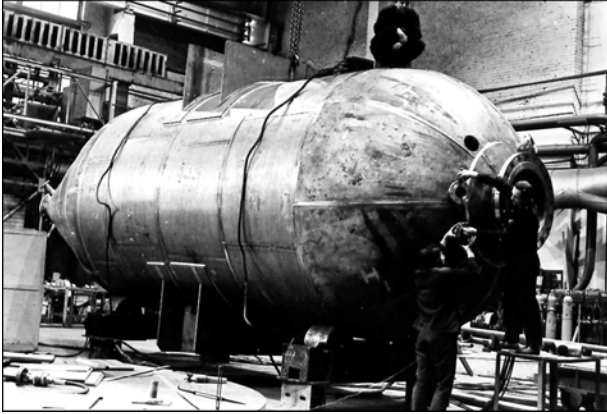


Figure 7. Fabrication of hydrolysis apparatus of alloy AT3 with 24 mm thick casing

bottom were made by manual TIG welding with groove preparation and using the 2V alloy filler wire with $d_f = 3\text{--}6$ mm. Automatic welding devices were equipped with aprons of the caterpillar type, which copied the shape of the mating surfaces and provided a reliable protection of cooling regions of a welded joint. Back side of the weld was shielded using a special device providing the uniform argon flow over the entire length of the welded joint. Welding was performed in two passes on each side. Large-diameter flanges were made by slot-gap TIG welding followed by straightening and machining. Sleeves and hatches were assembled to the casing using tack welding, and then were joined by manual TIG welding with groove preparation [1, 5, 6].

Main defects in TIG welding of titanium are pores, cold cracks and elongated gas cavities. Titanium and its alloys are insensitive to solidification (hot) cracking. Porosity is the main cause of reduction of service life of the welded joints. Elongated cavities are formed in root of the welds made by automatic immersed-arc TIG welding in argon atmosphere [1, 5, 6, 21, 22]. Defects of the welds in the form of cracks, lacks of fusion, burns-through in the crater and undercuts, as well as the welds with surfaces of a blue or grey colour, are inadmissible. Defects (except for temper colours) can be repaired by welding. Locations of defects should be thoroughly cleaned, and crack ends should be drilled prior to welding repair. It is recommended that one and the same location of a defect should be repaired by welding not more than two times using the same TIG welding as for welding of new parts.

Quality inspection and detection of defects in titanium welded joints are performed by the same methods as those used for steel welded joints. Quality and

state of billets being welded, welding consumables, and correspondence of edge preparation and assembly for welding to requirements of specifications, standards and drawings are checked in manufacture of parts. The specified welding and heat treatment processes should be kept to. The choice of inspection methods and scopes should be based on their economic expediency [22].

1. Shelenkov, G.M., Blashchuk, V.E., Melekhov, R.K. et al. (1984) *Manufacture and service of titanium equipment*. Kiev: Tekhnika.
2. (2001) *Machine-building*: Encyclopedia. Vol. 2: Non-ferrous metals and alloys. Ed. by I.N. Fridlyander. Moscow: Mashinostroenie.
3. Melechow, R., Tubielewicz, K., Blaszk, W. (2004) *Titanium: jero stopy*. Czestochowa: WPC.
4. Blashchuk, V.E. (2004) Titanium: alloys, welding, application. *The Paton Welding J.*, **3**, 30–37.
5. Gurevich, S.M., Zamkov, V.N., Blashchuk, V.E. et al. (1986) *Metallurgy and technology of welding of titanium and its alloys*. Kiev: Naukova Dumka.
6. Gurevich, S.M. (1990) *Reference book on welding of non-ferrous metals*. Kiev: Naukova Dumka.
7. Zamkov, V.N., Prilutskii, V.P., Shevelev, A.D. (1992) Metallurgy and technology of welding titanium alloys. In: *Welding and Surfacing Rev.*, Vol. 2, 1–39.
8. (1997) *Forming, welding, brazing and heat treatment of titanium and its alloys in aircraft engineering*. Ed. by A.G. Bratukhin. Moscow: Mashinostroenie.
9. (1998) *AWS Welding Handbook*. Vol. 4. Miami: American Welding Society.
10. Blashchuk, V.E., Shelenkov, G.M. (2005) Fusion welding of titanium and its alloys (Review). *The Paton Welding J.*, **2**, 35–42.
11. Paton, B.E., Zamkov, V.N., Prilutsky, V.P. (1996) Narrow-groove welding proves its worth on thick titanium. *Welding J.*, **5**, 37–41.
12. Gavriluk, V.S., Izmajlova, G.M. (2005) Laser welding of titanium alloy OT4 along a laser cut. *Tekhnologiya Metallov*, **1**, 23–26.
13. McMasters, J.A., Sutherlin, R.C. (2004) Update: titanium specification revised. *Welding J.*, **5**, 43–47.
14. Zamkov, V.N., Prilutsky, V.P. (2005) Methods for welding titanium alloys. *The Paton Welding J.*, **8**, 41–44.
15. Chernysh, V.P., Kuznetsov, V.D., Briskman, A.N. et al. (1983) *Welding with electromagnetic stirring*. Kiev: Tekhnika.
16. Zamkov, V.N., Topolsky, V.F., Kushnirenko, N.A. (1978) Tungsten electrode twin-arc welding of titanium plate. *Avtomatich. Svarka*, **2**, 44–47.
17. Dolotov, B.I., Muraviov, V.I., Ivanov, Yu.L. et al. (1997) Immersed tungsten electrode welding of VT20 alloy along the non-machined edges. *Svaroch. Proizvodstvo*, **7**, 25–27.
18. Blashchuk, V.E., Shelenkov, G.M. (2005) Welding of tubes with tube plates of heat-exchange apparatuses of titanium alloys. *The Paton Welding J.*, **9**, 36–38.
19. Blashchuk, V.E., Onoprienko, L.M., Shelenkov, G.M. et al. (1993) Plasma welding of titanium alloys. *Avtomatich. Svarka*, **3**, 31–33.
20. (1979) *Microplasma welding*. Ed. by B.E. Paton. Kiev: Naukova Dumka.
21. Troitsky, V.A. (1977) *Concise manual on quality control of welded joints*. Kiev: PWI.
22. Royanov, V.A., Zusin, V.Ya., Samotugin, S.R. (2000) *Defects in welded joints and coatings*. Mariupol: PGTU.



METHODS FOR MANUFACTURE OF POWDERS WITH QUASI-CRYSTALLINE COMPONENT FOR THERMAL SPRAYING OF COATINGS (REVIEW)

Yu.S. BORISOV, M.T. PANKO and V.L. RUPCHEV
E.O. Paton Electric Welding Institute, NASU, Kiev, Ukraine

Analysis of the state-of-the-art in methods for manufacture of powders of quasi-crystalline alloys has been conducted. It is shown that the most suitable method to manufacture powders for thermal spraying, among those available now, is compressed air atomisation of the melt, which provides powders with a high content of the quasi-crystalline phase and high workability (flowability).

Keywords: thermal spraying, coating, powder, quasi-crystalline icosahedral ψ -phase, manufacturing methods, workability of powder

Quasi-crystals are solids with atom packing that is characterised by the presence of rotational symmetry with axes of the 5th, 8th, 10th or 12th orders [1]. Many scientists consider discovery of quasi-crystals the most important achievement in materials science of the 20th century. Starting from 1984, scientists specialising in different disciplines, from more than 30 countries of the world (e.g. USA, France, Germany and Japan), have conducted comprehensive investigations into properties of quasi-crystals and their application fields.

Quasi-crystalline materials have a number of specific properties. For example, quasi-crystals of the Al-Cu-Fe system are interesting as materials with low thermal conductivity (at a level of oxide ceramics), having values of the thermal expansion coefficient at a level of metals, as well as high hardness, corrosion resistance and wear resistance [2, 3]. However, operations with quasi-crystals and their practical application in industry are substantially hampered because they have no microductility at room temperature. Therefore, they are commercially applied mostly as coatings.

One of the most common methods for production of such coatings is thermal spraying of powders. Productivity of the thermal spraying methods and quality of the resulting coatings depend to a considerable degree upon the physical and technological properties of the powders used for spraying. In turn, properties of the powders depend upon the method used to manufacture them.

The purpose of this study was to analyse existing methods for manufacture of powders with the quasi-crystalline component.

Evaporation and condensation method. This method is based on evaporation of heated metal or alloy, followed by its rapid cooling in the gas envi-

ronment or on the substrate. The process of production of powder or compact layer with the required structure can be controlled by varying the pressure of gas, rate of evaporation of metal and temperature of the substrate.

Powders containing the quasi-crystalline phase are manufactured by evaporation of 50 μm thick strips of alloys of the Al-Cu-Fe and Al-Pd-Mn systems by the laser beam [4]. Strips of the $\text{Al}_{62}\text{Cu}_{25.5}\text{Fe}_{12.5}$ and $\text{Al}_{70}\text{Pd}_{21}\text{Mn}_9$ composition were produced by melt spinning in argon atmosphere. Laser with a wavelength of 248 nm was used as an energy source. The laser beam was focused into a spot 0.5–1.0 mm in size on the surface of a target, which was rotated in a vacuum chamber filled with argon. Pulses with duration of 20 ns were emitted at a frequency of 10 Hz, and their energy was maintained at a constant level (50 mJ/pulse) in all experiments. The resulting powders were collected on a nylon filter of the vacuum system.

Investigation of structure of the Al-Cu-Fe system powder showed that it contained mostly the quasi-crystalline ψ -phase, as well as impurities of the β -phase. Structure of the Al-Pd-Mn system powder included the ψ -phase. Particles of the powder produced by laser evaporation had the form of flakes 10–20 μm in size, with ultra-fine granular structure.

The above process of manufacture of powders has low productivity, and its commercial application involves problems.

The evaporation and condensation method was applied to produce coatings of the Al-Cu-Fe system with a quasi-crystalline structure [5]. Evaporation of ingot of the $\text{Al}_{65}\text{Cu}_{20}\text{Fe}_{15}$ composition was performed from copper water-cooled crucibles in the vacuum chamber using electron beam gun. Cooling occurred at a substrate temperature of 470–1070 K. It was established that size of grains of the quasi-crystalline phase depends upon the substrate temperature, it becomes less than 100 nm at its decrease (below 770 K).

Method for centrifugal dispersion of the melt. This method is based on refining of the melt jet under



the effect of centrifugal forces of the rotating disk and further solidification of droplets in their flight to the chamber walls. This method was used in study [6] to manufacture powder of the Al-Cu-Fe system containing the quasi-crystalline component. Ingot with a weight of several hundreds of grams was melted in the crucible of the atomisation chamber in a helium atmosphere. Upon reaching the temperature required for pouring, the bottom of the crucible was opened, and the melt was poured onto the disk rotating at a speed of $30,000 \text{ min}^{-1}$. The melt spreading over the disk was transformed at its end into droplets, which solidified in flight to the chamber walls. The resulting powders contained not more than 30 vol.% of the ψ -phase, which, in the opinion of the authors of that study, was related to a low rate of cooling of the droplets.

The described method for manufacture of powders has low productivity. The content of the quasi-crystalline ψ -phase in the powders is insignificant.

Mechanical alloying method. This method consists in mixing of individual components or master alloys in the form of powders with certain particle size in high-power mixing units (attritors, planetary-type mills, etc.) to produce compositions of homogeneous mixtures or alloys.

In study [7], alloys $\text{Al}_{63}\text{Cu}_{25}\text{Fe}_{12}$, $\text{Al}_{65}\text{Cu}_{20}\text{Fe}_{15}$ and $\text{Al}_{70}\text{Cu}_{20}\text{Fe}_{10}$ were produced from powders of aluminium, copper and iron of the 99.9 % purity by mechanical alloying in a high-power planetary-type ball mill (Fritsch Pulverisette P-5). Treatment of the mechanical mixture corresponding to the $\text{Al}_{63}\text{Cu}_{25}\text{Fe}_{12}$ composition for 10–30 h led to formation of the stable quasi-crystalline β -phase. At the same time, in the other two alloys, $\text{Al}_{65}\text{Cu}_{20}\text{Fe}_{15}$ and $\text{Al}_{70}\text{Cu}_{20}\text{Fe}_{10}$, the icosahedral quasi-crystalline ψ -phase was synthesised, together with the β -phase. The ratio of atomic concentrations of aluminium and copper + iron by using this method was found to play an important role in formation of the quasi-crystalline phase.

In study [8], mechanical alloying was performed using the planetary-type ball mill AGO-2U, the speed of rotation of which was 685, 1015 and 1235 min^{-1} . Aluminium, copper and iron powders of the 99.9 % purity with a particle size of less than $150 \mu\text{m}$ in the bulk, corresponding to the $\text{Al}_{63}\text{Cu}_{25}\text{Fe}_{12}$ composition, were loaded together with the mill balls 3.5–8.0 mm in diameter and total weight of 200 g into a mixing tank. Powder weight was 10 g. Surface-active materials (benzene, kerosene) were added to prevent contamination of powder in milling. It was established that high-power milling promotes formation of an unstable nano-crystalline phase, where a number of transformations, including interaction with remainders of pure elements and secondary intermetallic products, occur, and the unstable cubic phase is transformed into the icosahedral quasi-crystal one as a result of annealing at a temperature of 773–873 K.

However, milling of the balls results in a high probability of contamination of the material with im-

purities. Additional annealing is required to produce a high content of the quasi-crystalline phase.

Ingot crushing method. The method for manufacture of powders containing the quasi-crystalline phase consists in melting of an alloy of the required chemical composition and structure, and subsequent crushing of ingots to produce particles of the required size.

Ingots of small weight (50–100 g) for laboratory studies were produced by melting in a water-cooled copper crucible of a high-frequency furnace in an atmosphere of argon [9, 10]. In studies [9, 11], specimens with a diameter of several millimetres and several centimetres high were formed by drawing of the melt into a quartz tube. The rate of solidification at a diameter of the tube equal to 10 mm was 250 K/s . Thus produced ingots of 47 alloys of the systems of Al-Cu-Fe, Al-Co-Fe, Al-Co-Ni, etc. [9] contained, as a rule, several phases. The content of the ψ -phase in them was increased by annealing for 24 h at a temperature of 1085 K, which allowed the weight content of the quasi-crystalline phase in an ingot to be increased to 95 % [10]. In study [12], ingots of 5 kg in weight and large diameter (50 mm) were used for milling, and properties of the coatings produced from the crushed powders were described. Crushing was performed in a mechanical agate mortar. Dubois [9] described the technology for manufacturing from the melt the Al-Cu-Fe-Cr ingots 2 kg in weight with 96 vol.% of the quasi-crystalline phase. The results reported are indicative of the possibility of applying this method for commercial manufacture of powders. These ingots were crushed in a drum mill with steel balls. Company «Saint-Gobain» uses this method to manufacture such powders under the «Cristome» grade [3].

The method of crushing ingots to produce powders has commercial application. However, it has an important drawback consisting in the fact that particles of the powder have a fragmented shape. This determines its low flowability and decreases workability in utilisation.

Method for spontaneous disintegration of the melt jet with cooling in water and crushing of granules. The method includes the following stages: preparation of the melt of the required chemical composition, passing of the melt through a round hole, disintegration of the jet into separate fragments following the Rayleigh law, formation of droplets under the effect of surface tension forces and cooling of the droplets in water, and drying and crushing of the powder granules to the required size.

This method for manufacture of powders from alloy $\text{Al}_{63}\text{Cu}_{25}\text{Fe}_{12}$ was first used by the E. O. Paton Electric Welding Institute [13]. The work resulted in production of a powder with the quasi-crystalline component (from 22 to 43 wt.%), the particles of which had an irregular fragmented shape and contained the β -, ψ -, λ - and θ -phases. This was caused by a low rate of cooling of the droplets and chemical heterogeneity of the melt.



Method of compressed air atomisation (dispersion) of the melt. This method described in detail in study [14] is currently the main commercial method for manufacture of powders of aluminium and aluminium alloys.

In studies by Sordelet and other researchers [12, 15], the preference in production of both coatings and sintered alloys of the Al-Cu-Fe system with the quasi-crystalline phase is given to powders atomised from the melt by an argon jet. The rate of cooling of the melt in gas atomisation amounts to $1 \cdot 10^5$ K/s, which is almost two orders of magnitude higher than the rate of cooling of an ingot in a water-cooled copper crucible. Structure of the powder at a high cooling rate is finer, and its composition is more homogeneous. Unlike the crushed powder, the particles of which are characterised by an irregular fragmented shape, the particles of the argon atomised powder have a spherical (or near-spherical) shape, which provides its good flowability in deposition of coatings. Atomisation with inert gas prevents the powder particle surfaces from substantial oxidation. Thus, the content of oxygen in the $Al_{63}Cu_{25}Fe_{12}$ powder produced by argon atomisation of the melt was 0.205–0.065 wt.% for particle sizes of 0–25 and 75–106 μm , respectively [16]. The content of oxygen decreased with increase in size of the particles because of decrease in their specific surface, and volume content of the ψ -phase varied from 69 to 55 % because the rate of cooling of fine particles is higher than that of coarse particles. Particle size composition is regulated by gas pressure. The method for manufacture of powders from quasi-crystalline alloys Al-Cu-Fe by high-pressure inert gas atomisation of the melt is described in study [17].

The E.O. Paton Electric Welding Institute tested the method for manufacture of the $Al_{63}Cu_{25}Fe_{12}$ powder by compressed air atomisation of the melt [13]. Aluminium of the 99.95 % purity, copper of the 99.9 % purity and iron of the 99.7 % purity were used as source materials. The melt was produced by induction melting of the charge in a graphite crucible in air by using a homogenising holding for 15 min at a temperature of (1100 ± 30) °C. A sprayer with a circular gas nozzle was used for atomisation of the melt, and the melt was fed through the centre of the gas flow.

The content of oxygen in the air atomised $Al_{63}Cu_{25}Fe_{12}$ powder varied from 1.50 to 0.63 wt.% for particle sizes of 0–50 and 100–160 μm . The content of oxygen decreased with increase in size of the particles because of decrease in their specific surface. The content of the quasi-crystalline ψ -phase was 54 to 50 vol.% for particle sizes of 0–50 and 80–100 μm , respectively, as the rate of cooling of fine particles is higher than that of coarse particles. Particles of the powder produced by air atomisation of the melt had irregular shape.

In their physical and operational characteristics, powders produced by argon atomisation of the melt met all the requirements imposed on powders for thermal spraying of coatings.

When using powders atomised in air, productivity of the spraying process decreases because of their poor flowability, and coatings have a lower quality because of the presence of oxide films on the powder particle surfaces.

Method of high-pressure water atomisation of the melt [14]. This method is used in industry to produce powders from different metals and alloys, along with gas atomisation of the melt. For example, a well known method of dispersion of the melt with high-pressure water jets allows the rate of cooling of the melt to be increased by an order of magnitude, compared with the gas atomisation method. This method is extensively employed for production of powders of ferrous and non-ferrous metals (e.g. copper and copper-base alloys). However, it failed to find a wide commercial application for manufacture of powders from aluminium and aluminium alloys because of a probability of explosion, which may be caused by evolution of hydrogen as a result of interaction of powders with water.

In testing this method for the manufacture of powders from the $Al_{63}Cu_{25}Fe_{12}$ alloy at the E.O. Paton Electric Welding Institute [13] by high-pressure water atomisation of the melt, refining of the melt flow prepared by the same technology as in air atomisation was performed by using separate water jets located on a ring about the melt jet at a pressure of 9 MPa. The powder thus produced was dried at a temperature of 200 °C for 4 h. Owing to a high solidification rate, it contained a substantial amount (69–74 vol.%) of the ψ -phase, compared with the powder atomised by compressed air (50–54 vol.%).

The content of oxygen in the powder was 1.95 to 1.60 wt.% for particle sizes of 0–50 and 100–125 μm , respectively. Like in the case of gas atomisation, the content of oxygen decreased with increase in size of the powder particles because of decrease in their specific surface. The content of the quasi-crystalline phase in the powder is also related to size of the particles: weight content of the ψ -phase in fine powder particles is higher than in coarse powder particles, which is attributable to a high rate of cooling of the former. Particles of the powder had irregular shape.

This manufacturing method requires further development, as the process is characterised by explosion hazard and high oxygen content of the powder, as well as by low flowability of the powder.

Therefore, powders produced by inert gas atomisation of the melt are most suitable for thermal spraying of coatings of the Al-Cu-Fe system.

Spherical shape of particles of the powder produced by argon atomisation of the melt provides its good flowability, which ensures a stable feed of the material under thermal spraying conditions. A low content of oxygen on the surface of the powder particles leads to formation of quality thermal spray coatings.

1. Dubois, J.-M. (1998) *Introduction to quasicrystals*. Berlin: Springer.

2. Dubois, J.-M. (2000) New prospects from potential applications of quasicrystalline materials. *Mater. Sci. and Eng.*, **294-296**, 4-9.
3. Sanchez, A., Garcia de Blas, F.J., Algaba, J.M. et al. (1999) Application of quasicrystalline materials as thermal barriers in aeronautics and future perspectives of use for these materials. In: *Proc. of MRS Symp. on Quasicrystals*. Vol. 553. Warrendale: MRS, 447-458.
4. Nicula, R., Jianu, A., Grigoriu, C. et al. (2000) Laser ablation synthesis of Al-based icosahedral powders. *Mater. Sci. and Eng.*, **294-296**, 86-89.
5. Ustinov, A.I., Movchan, B.A., Polishchuk, S.S. (2004) Structure and mechanical properties of Al-Cu-Fe coatings with quasi-crystalline nanostructure. *Transact. on Nanosystems, Nanomaterials, Nanotechnologies*, **2(1)**, 203-213.
6. Michot, G. (1996) Production of icosahedral Al-Cu-Fe powders by centrifugal atomization method. In: *Proc. of 5th Int. Conf. on Quasicrystals*. Singapore: World Scientific, 794-797.
7. Barua, P., Murty, B.S., Srinivas, V. (2001) Mechanical alloying of Al-Cu-Fe elemental powders. *Mater. Sci. and Eng. A*, **304-306**, 863-866.
8. Salimon, A.I., Korsunsky, A.M., Shelekhov, E.V. et al. (2001) Crystallochemical aspects of solid state reactions in mechanically alloyed Al-Cu-Fe quasicrystalline powders. *Acta Mater.*, **49**, 1821-1833.
9. Dubois, J.-M., Piranelli, A. *Aluminum alloys, substrates coated with these alloys and their applications*. Pat. 5652877 U.S. Publ. 1997.
10. Giacometti, E., Guyot, P., Baluc, N. et al. (2001) Plastic behavior of icosahedral Al-Cu-Fe quasicrystals: Experiment and modeling. *Mater. Sci. and Eng. A*, **319-321**, 429-433.
11. Kang, S.S., Dubois, J.M. (1992) Compression testing of quasicrystalline materials. *Phil. Mag. A*, **66(1)**, 151-163.
12. Sordelet, D.J., Kramer, M.J., Unal, O. (1995) Effect of starting powders on the control of microstructural development of Al-Cu-Fe quasicrystalline plasma-sprayed coatings. *J. Thermal Spray Technol.*, **4(3)**, 235-244.
13. Borisov, Yu.S., Panko, M.T., Adeeva, L.I. et al. (2001) Technologies for production and properties of powders of the Al-Cu-Fe system for thermal spraying of coatings with quasicrystalline structure. *The Paton Welding J.*, **1**, 45-50.
14. Nabojchenko, S.S., Nichiporenko, O.S., Murashova, I.B. et al. (1997) *Powders of non-ferrous metals*: Refer. Book. Moscow: Metallurgiya.
15. Sordelet, D.J., Kim, J.S., Besser, M.F. (1999) Dry sliding of polygrained quasicrystalline and crystalline Al-Cu-Fe alloys. In: *Proc. of MRS Symp. on Quasicrystals*. Vol. 533. Warrendale: MRS, 459-471.
16. Sordelet, D.J., Besser, M.F., Anderson, I.E. (1996) Particle size effects on chemistry and structure of Al-Cu-Fe quasicrystalline coatings. *J. Thermal Spray Technol.*, **5(2)**, 161-174.
17. Shield, E., Goldman, J. *Method of making quasicrystal alloy powder, protective coatings and articles*. Pat. 5433978 U.S. Int. Cl. B 22 F 009/08. Publ. 18.07.95.

ADAPTIVE WELDING TRACTOR FOR SINGLE-PASS ARC WELDING OF THICK-WALLED ITEMS



Welding tractors designed for mechanizing the welding process are used in welding butt joints on large-sized thick-walled structures. The welding tool manipulator of the tractor follows a rigid preset trajectory. The preset trajectory of welding tool motion and the established welding mode in practice often do not meet the optimum values, and the welding operator has to intervene during welding, performing corrective actions based on his own visual observations of the welding zone. Thus, the weld quality depends chiefly on the qualifications and practical skills of the welding operator.

To lower the influence of the human factor on welding quality the adaptive welding tractor has been fitted with a TV sensor, based on the laser triangulation method, and control units (industrial computer and/or programmable controller).

TV sensor is installed ahead of the welding zone, i.e. delayed control is implemented. Based on the data on the position and geometrical parameters of the butt joints received from the TV sensor, the control unit plots the optimum trajectory of the welding tool motion, selects optimum parameters of the welding mode for each specific section of the trajectory and forms the program for controlling the tractor drives and arc power source.

The control program is divided into a sequence of files of elementary control actions that are fed via a special interface to the actuator mechanisms of the welding tractor and the arc power source at the required moments of time. The errors of following the trajectory by the manipulation system of the tractor and deviation of the welding mode parameters from the specified modes are recorded during welding. Welding process specification is formed automatically for each weld.

The development allows improving the welded joint quality, reducing the scope of reworking of the welds and lowering the requirements to welder's qualifications.

Purpose. Adaptive welding tractor is designed for automatic arc welding of large-sized structures 7 to 50 mm thick in the positions from the downhand to the vertical one.

Application. Welding of large-sized sheet structures in heavy mechanical engineering, repair-welding operations on vertical surfaces in restoration of large-sized tanks and tank-cars.

Contacts: Dr. Shapovalov E.V.
Tel.: (38044) 287 67 11



EFFICIENCY ENHANCEMENT OF GAS GENERATORS OF HYDROGEN-OXYGEN MIXTURE

A.M. ZHERNOSEKOV and V.M. KISLITSYN
E.O. Paton Electric Welding Institute, NASU, Kiev, Ukraine

It is established that application of pulsed arc power sources with smooth adjustment of the pulse parameters and increased repetition rate allows increasing the electrolyzer efficiency.

Keywords: gas generators, hydrogen-oxygen mixture, electrolyzer, power sources, pulse repetition rate, gas-flame technology

For producing hydrogen of commercial purity electrolysis of water is most frequently used. However, in many cases commercial use of electrolytic hydrogen is more expensive than use of other combustible gases or hydrogen produced, for example, by the methods of catalytic conversion of water steam or reforming of methane. Attempts to reduce significant expenses, connected with transportation and storage of hydrogen stocks, by arrangement of the electrolyzer near the place of hydrogen consumption turned out to be vain because of high cost of the electrolyzer, need in a special premise for its location and high level of current expenses.

Wide use of hydrogen is restrained by the persistent opinion that it is especially explosion hazardous. This thesis was refuted early in 1970s, when it was experimentally proved in this country and abroad that under certain conditions it is possible to ensure sufficiently high degree of explosion and fire safety using electrolyzers of hydrogen-oxygen mixture (fulminic mixture) of a simpler design. First models of hydrogen-oxygen mixture generators had low productivity (up to $0.2 \text{ m}^3/\text{h}$) [1, 2], sufficient for application in the processes of brazing and microwelding of the items of electrotechnical and electronic industries.

Transition to development of the gas generator designs, having productivity above $1 \text{ m}^3/\text{h}$ [3], was performed on the basis of accumulated experience on their technological use. Main principles of development in PWI of hydrogen-oxygen mixture generators, having productivity above $1 \text{ m}^3/\text{h}$ [4], consisted in the double-unit design of the gas generator (the power source and the electrolyzer), application of the welding direct current source; separation of the produced mixture into two channels --- pure fulminic mixture and mixture enriched with hydrocarbon additives. This concept of the gas generator development, checked within dozen years at many enterprises of Ukraine, was later also used by leading foreign companies [5].

As showed practice of long-term operation of the A-1803 hydrogen-oxygen mixture generator of $1.8 \text{ m}^3/\text{h}$ productivity, developed on the basis of the

GVK-1.5 prototype, its design turned out to be the most successful from the viewpoint of the ratio of its market cost to the value of production cost and operation advantages in comparison with other designs. Reliability of the design and possibility of development on the basis of hydrogen-oxygen mixtures of environmentally clean technologies allows hoping on good prospects of the gas-flame technology development in this direction [6].

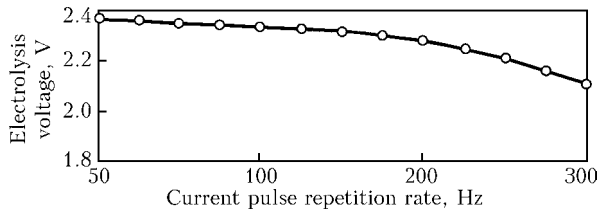
Taking into account that the A-1803 gas generator, developed more than 25 years ago, had efficiency of the electric power conversion into the chemical one not higher than 62 %, at present possibility appeared to enhance it by using nickel instead of low-carbon steel as a material for the electrodes, reduction of current density at the electrodes, and performance of the electrolysis process at the pressure below 0.3 MPa. In addition, possibility appeared to perform experimental check of the idea of electrolysis at increased frequencies, which was enabled by the developed in PWI [7] of power sources, which proved their efficiency in pulse-arc welding of special-purpose structures [8]. They allow smooth adjustment of the current pulse repetition rate from 30 to 300 Hz, duration of the pulses from 1.5 to 5.0 ms, amplitude of the current pulses up to 800 A, welding current from 50 to 315 A (at duty cycles of 100 %) and arc voltage from 16 to 40 V.

In the Figure experimental dependence of voltage in the electrolytic cell upon the current pulse repetition rate is presented. It turned out that this dependence is specific for the design of a particular electrolytic cell used in the A-1803 electrolyzer [3]. Phenomenon of the electrolysis voltage reduction may be explained in the following way. It follows from the literature [9] that in electrolysis of water solutions overvoltage of hydrogen mainly depends upon material of the cathode and density of the electrolysis current. However, as show results of this experiment, voltage of electrolysis depends to a great degree upon shape of the current pulses. As release of hydrogen in the process of electrolysis of water solutions exceeds two-fold release of oxygen, let us consider in greater detail peculiarities of hydrogen release.

As it is known, direct current sources, consisting of a three-phase rectifier, made according to the Larionov scheme, or a single-phase rectifier with a



BRIEF INFORMATION



Dependence of electrolysis voltage upon current pulse repetition rate

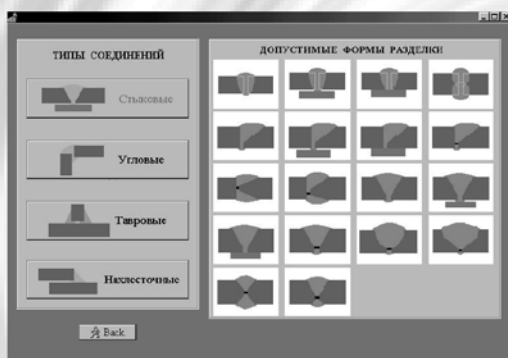
half-period rectifying, are used for electrolysis. In the process of electrolysis the cathode practically within several dozen seconds is covered by the layer of adsorbed hydrogen, which is accompanied by increase of the electrolysis voltage because of increase of the transitional electric resistance at the metal–electrolyte boundary. It is also known that if during growth of the hydrogen bubble on the cathode surface the electrolysis current is interrupted for a certain time, at the first instant stepwise increase of the cathode potential takes place, which inevitably causes formation of a new center of adsorption and redistribution of the adsorbed hydrogen bubbles. In the course of this process separation of the biggest hydrogen bubbles from the cathode surface and their natural or forced removal from the electrolyte occur. In a new cycle of the electrolysis current engagement release of hydrogen will occur most intensively exactly in new adsorption centers, formed at the instant of the electrolysis current engagement, voltage value of the power source being lower. Of primary importance in this case is full cessation of the electrolysis current, achieved when the voltage falls to zero level, but not its reduction, caused by pulsation characteristic of

conventional direct current sources. Presence of insignificant negative voltage peak will, evidently, also enable reduction of overvoltage caused by formation on the cathode surface of gas sublayer.

So, it is experimentally established that increase of current pulse repetition rate of the power source from 50 to 300 Hz will allow increasing the electrolyzer efficiency from 62 to 70 %. In case of additional replacement in the electrolyzer design of the electrode materials and increase of the electrolysis pressure one may expect increase of efficiency of this design of the electrolyzer up to 90 %.

- (1972) Wasser-Schweisser. *Produktion*, **8**, 104.
- Kislitsyn, V.M., Musin, A.G. (1974) Small-sized portable welders for soldering and oxyhydrogen welding. In: *Welding and soldering of elements of semiconductor devices and integrated circuits*. Kiev: Znanie.
- Lebedev, V.K., Rossoshinsky, A.A., Kislitsyn, V.M. et al. *Electrolyzer cell for production of oxyhydrogen gas from water and water solution*. USSR author's cert. 507668. Publ. 1976.
- Kislitsyn, V.M., Musin, A.G., Shevchenko, V.P. (1981) Generators GVK-1.5 and GVK-0.2 of hydrogen-oxygen mixture. In: *PWI Information letter*, 2(1246).
- (1988) Gas from electrolysis. *Newsweek*, March 21.
- Pismenny, A.S., Kislitsyn, V.M. (1995) Prospects of development of flame treatment of materials by oxyhydrogen mixtures. *Avtomatich. Svarka*, **2**, 39–42.
- Shejko, P.P., Pavshuk, V.M., Zhernosekov, A.M. et al. (2003) Power source for consumable electrode pulse-arc welding with automatic stabilization of welding parameters. *Svarshchik*, **4**, 4.
- Kudryashov, O.N., Novikov, O.M., Alekseev, I.V. et al. (2001) Welding of aircraft structures of thick aluminium alloys. *Svarochn. Proizvodstvo*, **12**, 31–33.
- Yakimenko, L.M. (1981) *Electrochemical processes in chemical industry. Production of hydrogen, oxygen, chlorine and alkali*. Moscow: Khimiya.

COMPUTER SYSTEM TO DESIGN TECHNOLOGIES FOR WELDING LIGHT ALLOYS



Selection of type of welded joint and shape of weld groove

Purpose. The computer system is intended for design of technologies for electric arc welding of light alloys with different alloying systems. It allows selection of shape of the weld groove, welding consumables, welding method and parameters depending upon the geometric features of a welded joint, base metal grade and other welding conditions. To make an optimal decision, a user is given an information support in the form of comparative characteristics of welding methods by 10 indicators, as well as information on welding-technological characteristics of non-consumable electrodes. Result of operation of the system has the form of a flow sheet.

Application. The system can be applied at machine building enterprises, technology and design bureaus, as well as at higher education institutions for training welding engineers.

Contacts: Prof. Makhnenko V.I.
E-mail: d34@paton.kiev.ua